Identified di-hadron angular correlations using the ALICE detector at the Large Hadron Collider

Erhardt, Filip

University of Zagreb

FACULTY OF SCIENCE
DEPARTMENT OF PHYSICS

Filip Erhardt

IDENTIFIED DI-HADRON ANGULAR CORRELATIONS USING THE ALICE DETECTOR AT THE LARGE HADRON COLLIDER

DOCTORAL THESIS

Zagreb, 2020

University of Zagreb

FACULTY OF SCIENCE
DEPARTMENT OF PHYSICS

Filip Erhardt

IDENTIFIED DI-HADRON ANGULAR CORRELATIONS USING THE ALICE DETECTOR AT THE LARGE HADRON COLLIDER

DOCTORAL THESIS

Supervisor:
Assoc. Prof. Nikola Poljak

Zagreb, 2020

Sveučilište u Zagrebu

PRIRODOSLOVNO - MATEMATIČKI FAKULTET
FIZIČKI ODSJEK

Filip Erhardt

KUTNE KORELACIJE IDENTIFICIRANIH PAROVA HADRONA POMOĆU ALICE DETEKTORA NA VELIKOM HADRONSKOM SUDARIVAČU

DOKTORSKI RAD

Mentor:
doc. dr. sc. Nikola Poljak

Zagreb, 2020.

Acknowledgements

Firstly, I would like to express my sincere gratitude to my mentor Assoc. Prof. Nikola Poljak for his support during my PhD study and related research. On more than one occasion I got stuck and his help enabled me to get through. I would also like to thank him for thoroughly reading my thesis and correcting the many errors that I missed, especially the gramatical ones. Secondly, I would like to thank my group leader Prof. Dr. Sc. Mirko Planinic who, together with my mentor, gave me many ideas regarding the direction in which to take my research. I am grateful to him for introducing me to various experts in the field from whom I learned a lot, as well as for sending me to various conferences where I greatly expanded my knowledge of the field. I would especially like to thank both Nikola and Mirko for their limitless patience and understanding, in particular when my progress was slow to the point of crossing the event horizon of a black hole.

Speaking of experts in the field, I would like to thank Alice Ohlson who was particularly helpful in getting me started, both with the codes and with my understanding of the subject matter and the state of the field. She spent an unreasonable amount of her precious time helping me and saved me at least a year of work if I had to figure it all out by myself.

I would like to thank my work colleagues Antonija Utrobičić and Marko Jerčić for many years of motivation, support and encouragement.

Last but not least, I would like to thank my family and my friends for putting up with me during the past few years and for motivating me to keep going. Many of you deserve more credit for helping me complete this thesis than you know. More importantly, I would like to thank you for all the laughs, good times and for reminding me that life always goes on.

This work has been fully supported by the Croatian Science Foundation project IP-2018-01-4108 “Demystifying Two Particle Correlations in pp collisions with the upgraded Time Projection Chamber”.

Abstract

Keywords: *two-particle angular correlations, Ridge, transverse sphericity, jet peak, quark-gluon plasma*

Two-particle angular correlations are a useful tool to study the mechanisms of particle production by observing the angular separation $(\Delta\eta, \Delta\varphi)$ between pairs of particles in an event. Different structures in the $\Delta\eta - \Delta\varphi$ space are caused by various modes of particle production and interactions between particles shortly after production. Examining these structures can give us insight into the nature of these interactions. One of these structures is called "the Ridge" and its significance is that the best current explanation for its origin comes from interactions within the quark-gluon plasma (QGP). Therefore, the presence of the ridge could be an indicator of the formation of QGP in a particular system. It is however often overshadowed by other structures in the correlation. In this thesis, two-particle angular correlations from proton-proton collisions at $\sqrt{s} = 7$ TeV are analysed using transverse sphericity and multiplicity to isolate and study different structures in the correlation function. Transverse sphericity (S_T) is a momentum space event shape variable giving a measure of how isotropically particles and their momenta are distributed within an event. This variable allows us to differentiate events containing jets produced in hard processes from events containing multiple soft, non-perturbative QCD processes. Differences in the shape of the correlation function as a function of transverse sphericity are presented. A drastic change in the shape of the correlation function is observed. There appears to be consistent shrinking of the jet peak together with an overall change in the size and shape of certain underlying long-range correlations. In order to quantify the data various projections are made which are subsequently fit. The width and yield of the jet peak are extracted from the fits for different S_T bins showing a quasi-exponential decrease

in the yield of the jet peak with increasing S_T, however the width remains constant. A couple of unexpected structures appear in the correlation function, including the presence of a long range correlation imitating the Ridge in a data sample where it shouldn't appear. This indicates that the Ridge may be obtained by introducing a mathematical bias into the data sample by means of S_T and possibly other variables.

Contents

Chapter 1

Introduction

The boundaries of what is known about the nature of the universe are constantly being pushed and expanded in different directions through the branches of modern physics. One of these branches is particle physics, which studies the nature of the particles that constitute matter and the interactions between them. The boundaries of particle physics are expanded experimentally through high energy collisions of particles. Ever increasing energies of collision enable the probing of ever smaller and more elusive structures of the universe. The Large Hadron Collider (LHC) at the European Organization for Nuclear Research (CERN) is a particle accelerator at the forefront of particle collision energies and thus at the forefront for new discoveries in particle physics. One of the main experiments at the LHC is ALICE (A Large Ion Collider Experiment), optimized for probing the aspect of particle physics relating to the strong interaction via the collision of heavy ions. One of the aims of ALICE is to study the characteristics of Quark-Gluon Plasma (QGP) which is a state of matter made up of asymptotically free quarks and gluons that exists at extremely high temperatures and/or densities. It is believed that the Universe was completely in a QGP state up until a few milliseconds after the Big Bang.

Any new phenomenon produced in heavy ion collisions, be it QGP or an undiscovered particle or interaction, is usually extremely short lived decaying into other particles before it has a chance to get anywhere near any detector. Therefore the particles into which the new phenomenon decayed must be studied in order to infer some of its characteristics. Two-particle angular correlations are a useful tool to study the mechanisms of particle production by observing the angular separation $(\Delta\eta, \Delta\varphi)$ between pairs of particles in an event. Different structures in the $\Delta\eta - \Delta\varphi$ space are caused by various modes of particle production and interactions between particles shortly after production. Examining these

structures can give us insight into the nature of these interactions. One of these structures is called “the Ridge” and its significance is that the best current explanation for its origin comes from interactions within the quark-gluon plasma. Therefore, the presence of the ridge could be an indicator of the formation of QGP in a particular system. It is however often overshadowed by other structures in the correlation.

In this thesis, two-particle angular correlations from proton-proton collisions at $\sqrt{s} = 7$ TeV are analysed using transverse sphericity and multiplicity to isolate and study different structures in the correlation function. Transverse sphericity is a momentum space event shape variable giving a measure of how isotropically particles and their momenta are distributed within an event. This variable allows us to differentiate events containing jets produced in hard processes from events containing multiple soft, non-perturbative QCD processes.

This thesis is organized as follows: Chapter 2 will describe the theoretical background of the physics that is important for this thesis including the Standard Model, Quark-Gluon Plasma and heavy-ion collisions; Chapter 3 will give a theoretical overview of the two-particle angular correlation function and its underlying physical structures; The experimental setup consisting of the LHC and ALICE detector is described in Chapter 4; In Chapter 5 the data sample selected for the thesis and the ways in which it is shaped for the analysis is discussed. This includes the introduction of Transverse Sphericity as an event shape variable to differentiate the data; Chapter 6 describes the formalism with which the correlation function is implemented into the data analysis procedure; The experimental results are presented in Chapter 7 and the associated errors are discussed in Chapter 8; Finally, the results are discussed and the thesis is summarized in Chapter 9.

Chapter 2

Quark-Gluon Plasma and Heavy-ion Collisions

Quark-Gluon Plasma (QGP) is a state of matter where the elementary particles that carry the strong nuclear force (quarks and gluons) and make up hadrons are seemingly freed of their strong attraction for one another. This exotic state of matter forms under extreme energies and densities. Such conditions were thought to permeate the early Universe up to a few milliseconds after the Big Bang and also to currently exist in the centres of neutron stars. These conditions can also be recreated in the lab using ultra-relativistic heavy-ion collisions as the primary tool for studying QGP as well as mechanisms of the strong nuclear force in general. This chapter will briefly discuss the Standard Model and quantum chromodynamics which is the theory that governs the strong interaction. The characteristics of QGP will be discussed including heavy-ion collisions as well as how heavy-ion collisions can be used to detect QGP. Finally, the possibility of the formation of QGP in lighter collision systems will be discussed.

2.1 The Standard Model and quantum chromodynamics

The Standard Model

The matter and energy content of the Universe, at this moment in time, are primarily best described by physicists in terms of the motion and interactions of elementary particles. One of the major unsolved problems in physics is finding a single theory that would successfully describe all particles in the Universe and unite all fundamental laws and

theories governing the interaction of those particles. Such an all encompassing theory would be called a Theory of Everything (ToE) and there are presently two theoretical frameworks which, while mutually incompatible, together appear to approximate a ToE. These two frameworks describe the workings of the Universe at vastly different scales, with General Relativity (GR) focusing on gravity and describing the Universe over large distances and masses, and Quantum Field Theory (QFT) focusing on the other fundamental forces and describing the Universe over small distances and masses. The QFT framework includes the standard model which is the most successful theory of particle physics to date and arguably one of the most successful theories of nature in general.

The Standard Model (SM) is a theory that classifies all known elementary particles and describes three of the four known fundamental interactions between the particles. The fundamental forces described are the electromagnetic force, the weak force and the strong force which, according to the standard model, are mediated by force carrying particles.

The elementary particles described by the standard model can be distinguished by various characteristics [1]. The primary attribute used to characterize the elementary particles is their spin. The particles that have a half-integer spin are called elementary fermions and obey Fermi-Dirac statistics whereas elementary bosons have an integer spin and obey Bose-Einstein statistics. While fermions in general are particles that have any odd half-integer spin ($\frac{1}{2}$, $\frac{3}{2}$, $\frac{5}{2}$, etc.) the fermions of the standard model all have a spin of exactly $\frac{1}{2}$. Twelve fermions exist in the standard model and are further separated into two groups of six depending on how they interact, or in other words which charge they have. Quarks are the fermions that have a colour charge and thus participate in strong interactions. The six quarks that exist are the down (d), up (u), strange (s), charm (c), bottom (b) and top (t) quarks. Each of the 6 quarks has one of 3 possible colour charges. The fermions that have no colour charge are called leptons and only participate in electroweak interactions. The six leptons that exist are the electron (e), electron neutrino (ν_e), muon (μ), muon neutrino (ν_μ), tau (τ) and the tau neutrino (ν_τ). The twelve fermions can be further grouped into three groups of four particles called generations. Each generation consists of a negatively charged lepton, a neutrino and two quarks with charges $+\frac{2}{3}$ and $-\frac{1}{3}$. The corresponding particles in each higher generation have identical properties to the particles in the previous generation other than the fact that they have a higher mass. Therefore the particles from higher generations spontaneously decay via the

weak force into the lighter particles of the first generation meaning that there are only four stable fermions according to the standard model; the electron, the electron neutrino, the up quark and the down quark. All observable stable matter in the Universe is composed of the first generation of fermions, with all observed quarks confined into hadrons (protons - uud and neutrons - udd) and leptons such as the electron being free. Each of the twelve fermions has a corresponding antiparticle that has the same mass as the particle but has opposite physical charges such as electric charge, chirality and weak isospin. A summary of the fermions of the SM along with some of their characteristics can be seen in table 2.1.

The elementary bosons of the standard model can also be divided into two groups. The first group is the gauge bosons, which are particles that have a spin of 1. These particles are also called force carriers since they are the ones that mediate the three fundamental forces of the standard model. The photon is the gauge boson that mediates the electromagnetic interaction. It is a massless stable particle that interacts with particles that posses an electric charge and is its own antiparticle. The weak interaction is mediated by the W^+, W^- and Z bosons. They are massive particles, amongst the most massive particles in the standard model, causing the weak interaction to have a very short range, less than the diameter of the proton. The W^+ and W^- are charged and are each others antiparticle, whereas the Z is neutral and is its own antiparticle. These particles interact with all of the fermions of the standard model and are responsible for their decay, or in other words, the transformation of one fermion into another. The strong interaction is mediated by gluons of which there are 8 types (a ninth, colourless, gluon singlet could theoretically exist but is not observed in nature). Finally, a single non-gauge boson exists in the standard model, the Higgs boson, which is a scalar boson with a spin of 0. It is a massive, electrically neutral particle which manifests as a quantum excitation of the Higgs field. The Higgs field permeates the Universe and is responsible for the mass of certain elementary particles [2–5].

Despite the fact that the Standard Model is thought to be theoretically self-consistent and is extremely successful at making predictions that have since been experimentally verified, some phenomena remain unexplained and the theory falls short of being a complete theory of fundamental interactions. It does not include the force of gravity at all, and is at odds with the current best theory of gravity (General relativity), it cannot explain

Table 2.1
The fermions of the standard model grouped by generation with their corresponding characteristics [6].

Generation 1		Generation 2		Generation 3		Properties	
Fermion	Mass (MeV/c^2)	Fermion	Mass (MeV/c^2)	Fermion	Mass (MeV/c^2)	Charge (e)	Weak isospin
e^-	0.511	μ^-	105.7	τ^-	1 776.86	-1	$-1/2$
ν_e	$< 2.2 \times 10^{-6}$	ν_μ	< 0.170	ν_τ	< 15.5	0	$+1/2$
u	2.2	c	1 280	t	173 100	$2/3$	$+1/2$
d	4.6	s	96	b	4 180	$-1/3$	$-1/2$

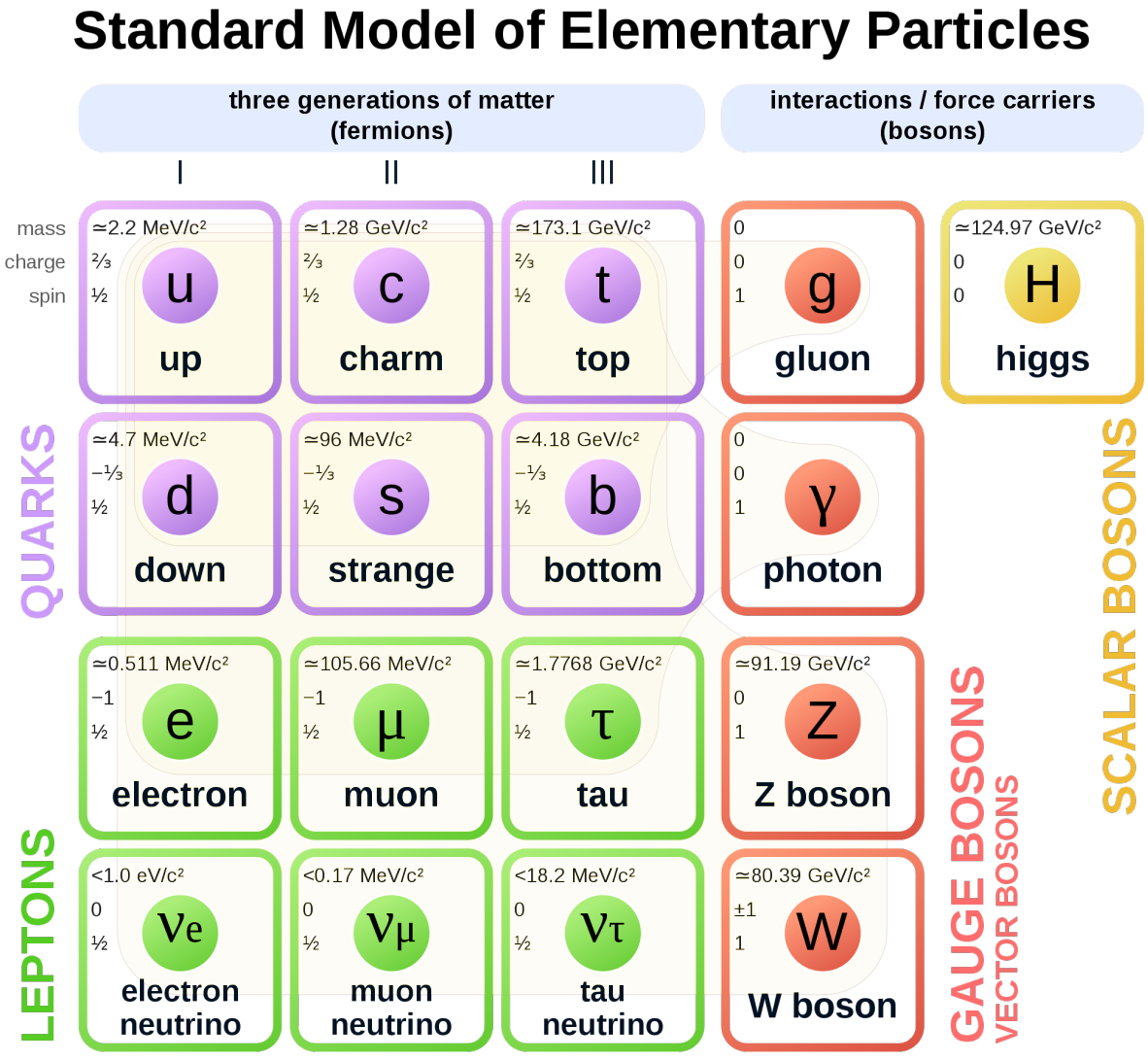

Figure 2.1: The elementary particles of the standard model grouped by their characteristics along with each particles mass, electric charge and spin [7].

baryon asymmetry, nor can it account for the accelerating expansion of the Universe. The SM does not contain any viable dark matter particle that possesses all of the required properties deduced from astrophysics. It also does not incorporate neutrino oscillations and their non-zero masses.

Quantum Chromodynamics

The part of the SM relating to the strong interaction is called quantum chromodynamics (QCD), whose name is analogous to quantum electrodynamics (QED), however, instead of the electric charge of QED, QCD has an equivalent charge called colour. QCD is a quantum field theory that describes the strong interaction between quarks and gluons explaining how they coalesce into hadrons, such as the proton, as well as how those hadrons are able to stick together forming the nucleus of atoms when electrostatic forces would like to push them apart. QCD is a non-abelian gauge theory with an SU(3) symmetry group. The discovery of the Delta baryon Δ^{++} with its unusual +2 charge was vital for the development of the quark model. Observations that particles like the Δ^{++} exist and the fact that they are composed of 3 quarks of the same flavour (uuu) indicated that a new quantum number was needed to avoid Pauli's exclusion principle leading to the introduction of colour. There are three types of colour charge; red, green and blue, each with its corresponding anticolour; antired, antigreen and antiblue. QCD states that any free particle that exists must be white (colour neutral). There are 2 main ways of obtaining a white particle; either having a colour anticolour pair of particles or a triplet of particles where all three colours (or anticolours) are present. Therefore mesons are always colour anticolour doublets and baryons are always red, green and blue triplets. Particles containing more than 3 quarks are also theoretically possible if they can be separated into some combination of white doublets and triplets. The strong force is mediated by the exchange of gluons, which also have a colour charge. Gluons carry a combination of one colour and one anticolour not necessarily the pair to the colour, so the gluon has some net colour charge. This differs from QED where the force mediating particle is the photon which is electrically neutral (the analogy of consisting of an electric charge and an anti-electric charge could still hold as QED only has 1 type of charge and they necessarily cancel each other out). This means that while photons don't interact with each other electromagnetically, gluons do in fact interact with each other via the strong force. It also

means that quarks can and do constantly change while interacting with other quarks. A green quark can interact with other quarks by emitting a green-antired gluon leaving it red. If a red quark were to absorb that gluon it would become green. This is the reason why we do not say that we have 3 different up quarks, one for each colour, but only 1 type whose colour can change.

The dynamics of quarks and gluons under the effects of the strong force can be determined by the QCD Lagrangian [8]:

$$\mathcal{L}_{QCD} = -\frac{1}{4}G^{\alpha}_{\mu\nu}G^{\mu\nu}_{\alpha} + \sum_{q}\left(\bar{\psi}_{qi}i\gamma^{\mu}\left[\delta_{ij}\partial_{\nu} + ig(G^{\alpha}_{\mu}t_{\alpha})_{ij}\right]\psi_{qj} - m\bar{\psi}_{qi}\psi_{qi}\right), \tag{2.1.1}$$

where $G^{\alpha}_{\mu\nu}$ is the field strength tensor which is found from the gluon field A^{α}_{μ},

$$G^{\alpha}_{\mu\nu} = \partial_{\mu}A^{\alpha}_{\nu} - \partial_{\nu}A^{\alpha}_{\mu} - gf^{\alpha\beta\gamma}A^{\beta}_{\mu}A^{\gamma}_{\nu}. \tag{2.1.2}$$

The index α runs over the colour degrees of freedom of the gluon field ($\alpha = 1, \ldots, 8$). The third term in equation (2.1.2) is a non-Abelian term which distinguishes QCD from QED where $f^{\alpha\beta\gamma}$ are the structure constants of the SU(3) colour group. This is the term which enables gluons to couple to themselves. ψ_i is the Dirac spinor of the quark field in triplet representation (i represents colour). The sum over q is a sum over the different flavours of quarks, u, d, s, ... The term g represents the coupling of the theory, or strong (colour) charge, and determines the strength of the interaction between coloured quarks and gluons. It is linked to the coupling constant α_s by $g = \sqrt{4\pi\alpha_s}$. One of the main differences between QED and QCD is in the nature of this coupling constant. In QED, this constant is called the fine structure constant and is equal to $\alpha = \frac{e^2}{\hbar c} \approx \frac{1}{137}$ which is small compared to the strong coupling constant which is of the order of 1. The main difference is that the QCD coupling constant, α_s, is not a constant at all but is a function of the momentum transferred in the interaction [9, 10]. The first-order perturbative QCD calculation (at large values of Q^2) gives:

$$\alpha_s(Q^2) = \frac{12\pi}{(33 - 2n_f)\cdot\ln(Q^2/\Lambda^2_{QCD})} \propto \frac{1}{\ln(Q^2/\Lambda^2_{QCD})}, \tag{2.1.3}$$

where Q^2 is the transferred four-momentum in the interaction and Λ_{QCD} is a scale constant parameter in QCD [11]. The spatial separation between quarks goes as $\lambda\!\!\!^{-} = \frac{\hbar}{\sqrt{Q^2}}$. Therefore, for very small separation and high value of Q^2, the coupling constant decreases and vanishes asymptotically. This dependence of the coupling constant manifests as two named properties of coloured objects (quarks and gluons):

- **Colour confinement** - is a property that states that a single colour charge cannot exist by itself [12–14]. Since the strong force between two colour charges doesn't decrease with distance as does the electric force, the energy needed to separate them grows boundlessly (as the distance increases, the momentum transfer Q^2 decreases and the coupling constant increases). Eventually, with a high enough separation, this energy becomes large enough that the energy in the system is minimized if a quark-antiquark pair is produced, which couple to the two colour charges being separated creating two new white objects from the original one. This is the reason that all free particles are colour neutral (white). While colour confinement might not be analytically proven, it has been confirmed countless times from lattice QCD calculations and through experiments.

- **Asymptotic freedom** - is a property of QCD that is observed as a steady reduction in the strength of the strong interaction (a decrease in the coupling constant) as the energy scale of those interactions increases. In such cases where the momentum transfer (Q^2) is high, such as at short distances or high temperatures, the partons are asymptotically free and act as if they are not confined into individual colourless particles [15–17].

There are two main regimes in which different approaches are used to attempt to theoretically solve the QCD equations. The first regime is called perturbative QCD and is used for large values of Q^2 which corresponds to very small distances or hard collisions. In this regime the equations are solved in a similar manner as they are in QED. The second regime is the non-perturbative QCD range which is the case for small values of Q^2, also called soft collisions. In this regime, a discreet numerical technique is used and is called Lattice QCD. In it, space and time are divided into a grid of lattice points.

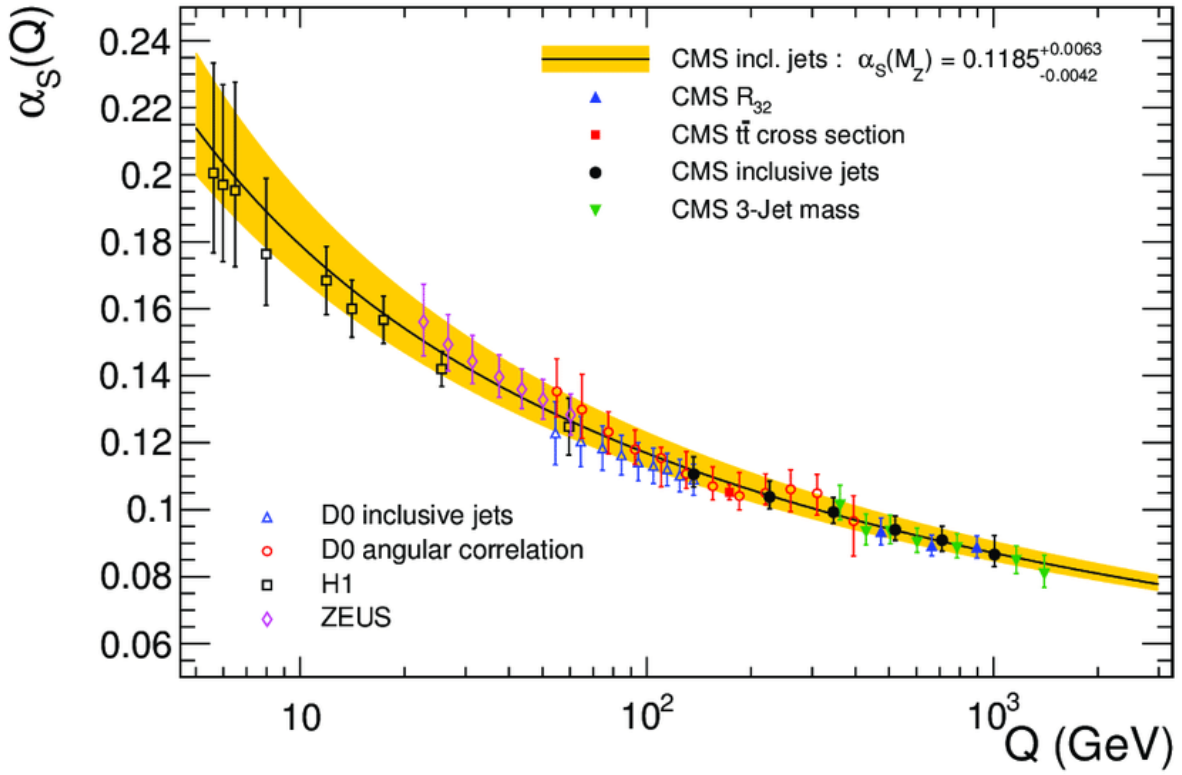

Figure 2.2: Measurements of α_s as a function of the energy scale Q [18]. Conventionally, the value of α_S is quoted at the mass of the Z^0 boson (about 91 GeV) as $\alpha_S(M_Z)$.

2.2 Quark-Gluon Plasma

The concept of asymptotic freedom lead to the hypothesis that a state of matter called Quark-Gluon Plasma (QGP) may exist under certain conditions. The hypothesis stated that at sufficiently small distances between partons or at sufficiently high energy densities, the strong force acting on them would become weak enough that the parton matter would behave as a weakly interacting parton gas instead of separate, confined hadrons. The name quark-gluon plasma was given as an analogy to conventional electromagnetic plasma where regular atoms are dissociated into free nuclei and electrons at sufficiently high temperatures acting as an electron-ion gas. It is believed that the conditions in the early Universe were such that the entire Universe was in a Quark-Gluon plasma state. This period in the evolution of the early Universe is known as the quark epoch and lasted only a few milliseconds starting approximately 10^{-12} seconds after the Big Bang and ending around $\sim 10^{-6} - 10^{-5}$ seconds after the Big Bang. Studying QGP would give valuable insight into the physics governing some of the earliest moments of the Universe. QGP is not

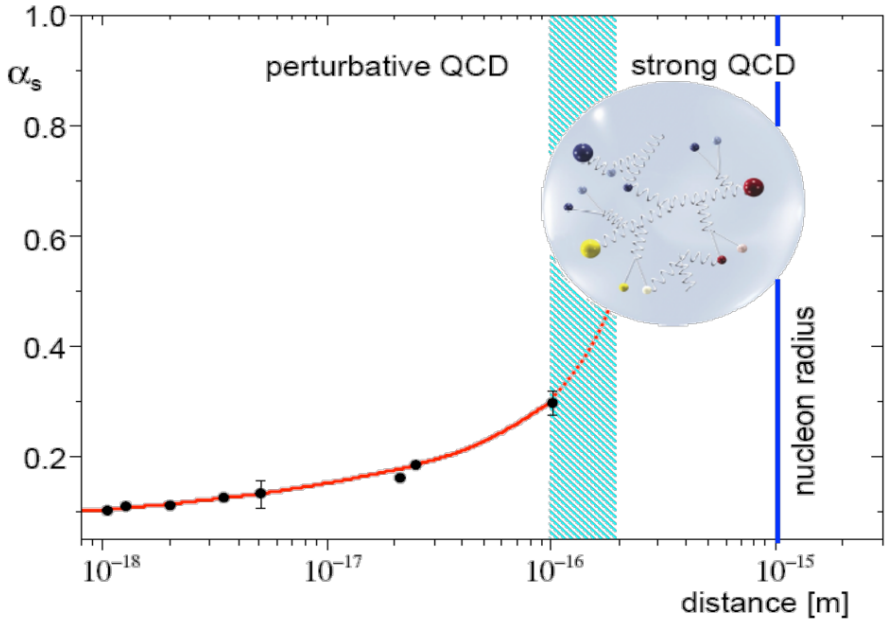

Figure 2.3: α_s as a function of distance [19]. The two regimes at small and large distances can be seen separated by a blue "intermediate" region.

experimentally available to us since the Universe only became transparent to EM radiation a few hundred-thousand years later when it was cold enough for protons and electrons to combine into neutral atoms. It is also theorised that QGP might exist today in the centre of certain massive neutron stars but with current technology this is not experimentally available to us either. Fortunately, QGP can be created in the lab by heavy-ion collisions. Temperatures around 2×10^{12} kelvin should be enough for deconfinement corresponding to about 175 MeV per particle or an energy density of about 1 GeV/fm in the QGP medium. Colliding two large ions at a sufficiently high energy could lead to a droplet of medium where this required energy per particle can be achieved. This collision would create a "fireball" of QGP which would expand under its own pressure and cool before recombining into regular hadronic matter.

Experiments at CERN and BNL tried to create QGP in the 1990s by colliding ions of heavy elements (lead or gold) with an announcement by CERN that they had indirect evidence for a "new state of matter" in 2000 [20] and an announcement from BNL that claimed that they had indeed created QGP a few years later [21, 22]. Modern experiments at RHIC and the LHC have continued studying the properties of QGP with a temperature

of 5.5×10^{12} kelvin reportedly achieved by the ALICE experiment in a lead-lead collision [23]. This temperature is almost triple the temperature required for deconfinement meaning that more of the properties of the QGP fireball can be studied. Many physicists were surprised to find out that the QGP did not act as a weakly interacting gas as had been suspected but behaved like a nearly perfect liquid with very small viscosity. Hydrodynamic models are some of the most successful models for describing the evolution of the QGP medium.

Questions remain about the nature of the phase transition between QGP and ordinary matter. Is it a smooth cross-over or some sort of first or second order canonical phase transition? Is it a combination of both with a critical point somewhere? At what temperatures and densities does the transition happen? Lattice QCD calculations suggest phase diagrams similar to the one shown in figure 2.4 with a smooth cross-over at low particle densities transitioning to a first order phase transition at higher densities. These calculations tend to give the critical temperature for the deconfinement of partons at around $T_c \approx 155 - 175$ MeV, which seems to roughly agree with experimental observations.

2.2.1 Signatures of QGP

The QGP that is created by heavy-ion collisions expands and cools down very quickly, lasting only on the order of 10^{-23} seconds, meaning it never moves from the collision point and enters our detectors. Therefore we can only observe the particles that are formed as a result of the hadronization of the QGP. Various properties of these particles, such as the types of particles, number of particles, their energies and the direction in which they fly may be used as indicators for the presence of QGP and even enables us to study some of the properties of the QGP. Some of the measured and some only theoretical signatures of QGP are discussed below.

Direct photons

Directly produced photons are interesting because they can be used to estimate the temperature of the QGP. Since they only interact electromagnetically their mean free path is much larger than that of other measurable particles and is even larger than the size of the reaction volume [25, 26]. Photons also don't undergo final state interactions

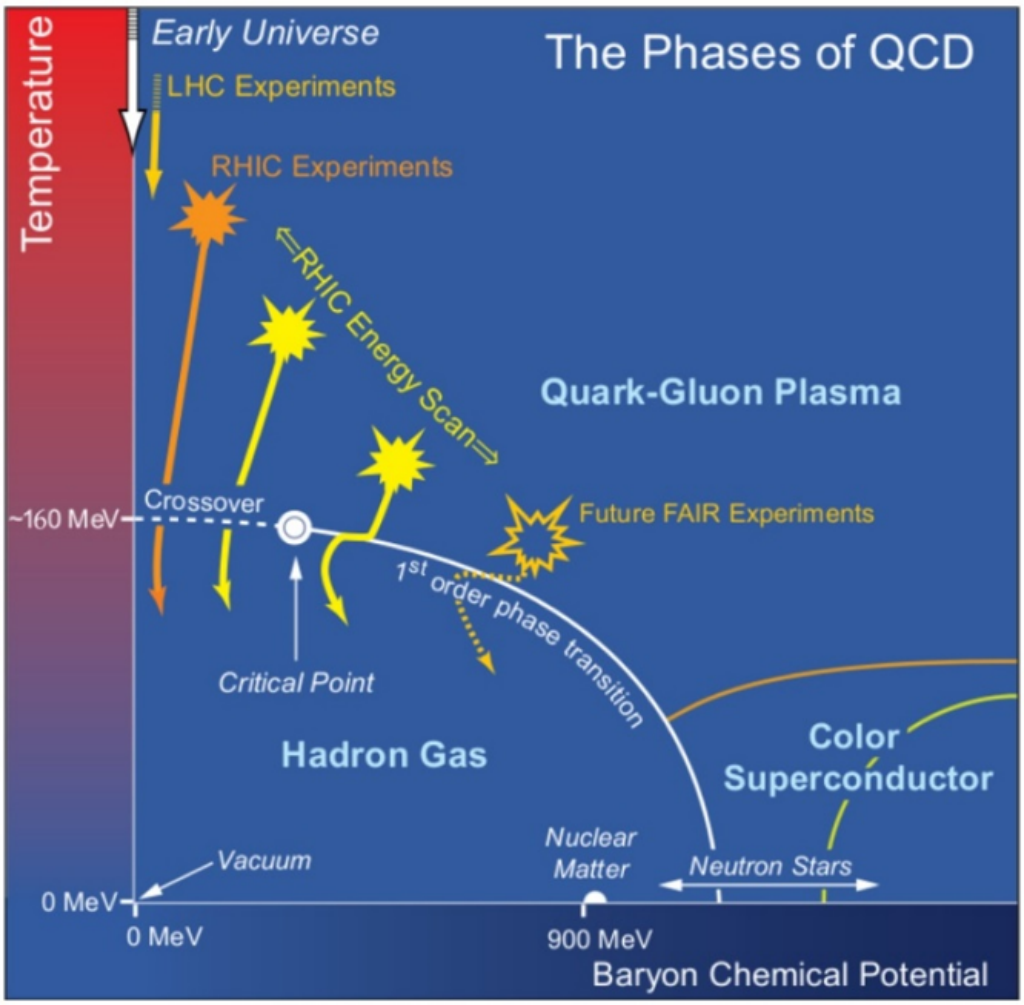

Figure 2.4: A possible phase diagram of quark matter. The position of the critical point is still unknown [24].

as hadrons do, meaning they can serve as a direct probe of the interaction. The photons can be separated into two categories; prompt photons and thermal photons. Prompt photons are the photons that are produced in the initial hard parton collision. These are present even in collisions where QGP is not formed. They originate from quark-gluon Compton scattering, jet fragmentation and quark-antiquark annihilation. On the other hand, thermal photons are produced in the QGP phase (as well as in the hadron gas phase after hadronization) where thermalized photons are scattered. An increase in the emmision of thermal photons would be a signature of QGP. Measuring this increase is difficult because the production rate of these photons is low and there is a large background from neutral meson decays, such as $\pi^0 \to \gamma\gamma$. An excess of photons at low p_T can be seen in the ALICE results shown on figure 2.5. The excess is present compared to the direct photon fit from NLO calculations from scaled pp collision data (blue line). The effective

temperature of the thermalized system that produced the photons is extracted from the low p_T measurements using an exponential fit $\frac{dN}{p_T d_{p_T}} \sim e^{-p_T/T}$. This yields an effective temperature of $T = 304 \pm 51$ MeV which is above the predicted temperature for QGP formation $T \approx 170$ MeV meaning that QGP could have formed [27].

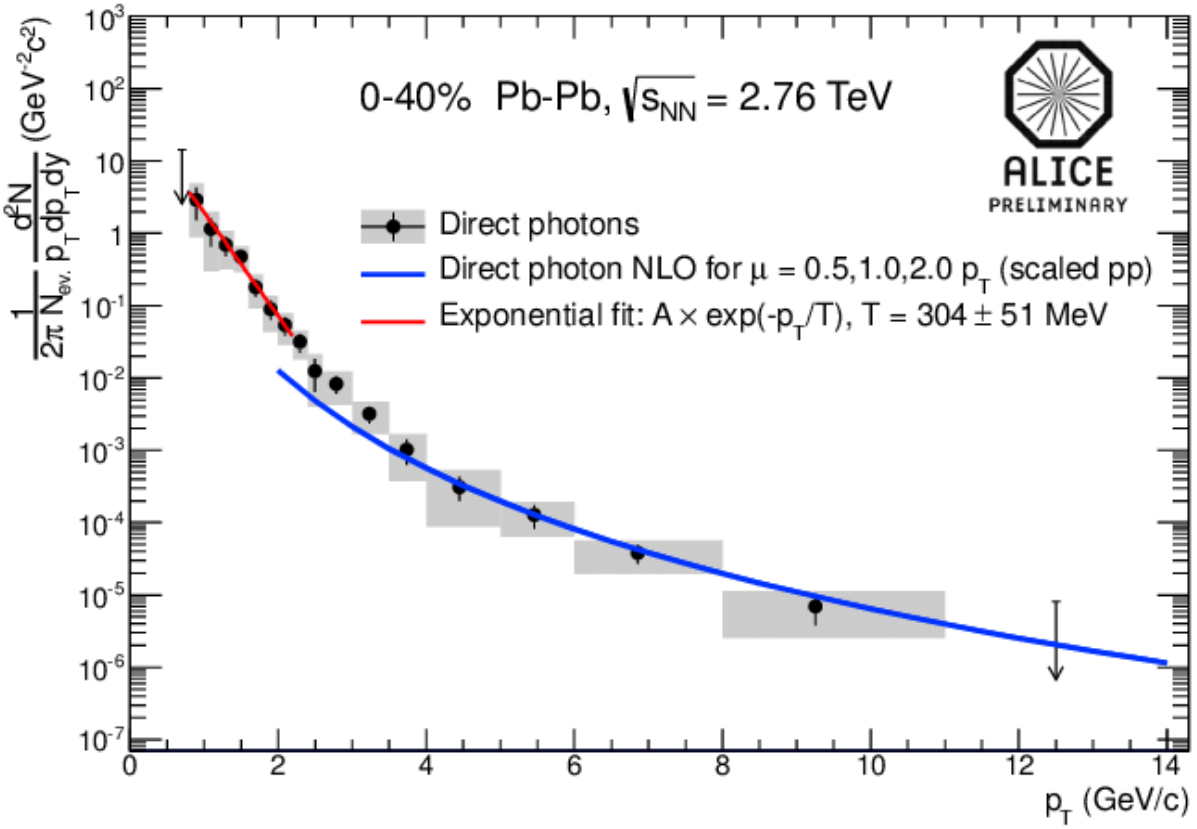

Figure 2.5: ALICE measurement of the direct photon invariant yield in Pb-Pb collisions at $\sqrt{s_{NN}} = 2.76$ TeV for the top 40% central events. There is an excess of photons at low p_T compared to the direct photon NLO fit (blue line). The effective temperature of the medium is extracted from the low p_T measurements using an exponential fit [27].

Kinematic Probes

Certain thermodynamic properties can be extracted, or at least approximated, using collision observables [25]. The temperature T of a system can be linked to the average transverse momentum of the particles in that event $\langle p_T \rangle$, the entropy of the system s to the hadron rapidity distribution $\frac{dN}{dy}$ and the energy density ϵ can be linked to the transverse energy density $\frac{dE_y}{dy}$. Plotting the temperature of the system as a function of energy density could show the nature of the phase transition. A steady rise in the $T - \epsilon$ function followed by a plateau and then a further rise would indicate a first order phase

transition. This has not yet been measured since current experiments might not obtain high enough densities to cross over the phase transition.

Jet Quenching

Jets are often formed in high energy particle collisions when a quark or gluon hadronizes and forms a narrow cone of particles. If QGP is present, the original parton or even the jet itself can interact strongly with the medium leading to a reduction in the energy of the jet. This is known as jet quenching. Some jets that pass through a larger volume of the QGP medium can even disappear entirely. This phenomenon is even more obvious in cases when back-to-back jets are formed off-centre from the QGP medium. Due to momentum conservation these jets should have equal energies, however if the trajectory of one of the jets passes a longer distance through the QGP medium than the other, the two jets will emerge with a lopsided momentum or maybe only one of the jets ends up emerging from the medium. One way of quantifying this is by observing R_{CP} for charged jets, which is the ratio of the normalized number of particles belonging to jets in central collisions (where QGP forms) and in peripheral events (where QGP doesn't form). If this ratio is equal to 1 then the physics present in both systems is the same. If jet quenching is present in QGP then we expect the ratio to be less than 1 to account for some loss in particles from the jets and the jets themselves. This can be seen on figure 2.6 which shows ALICE R_{CP} results for charged jets. The results are consistent with jet quenching showing a larger suppression for more central events.

High p_T suppression

Similarly to the case with jet quenching, individual high-energy particles will lose energy as they traverse the QGP medium. This is due to collisional energy loss from multiple elastic collisions with thermal particles in the medium. This means that we expect fewer high-energy particles in cases where QGP is formed. This can be quantified using the nuclear modification factor R_{AA} for charged particles. This compares the number of particles produced in central heavy-ion collisions to the number of particles produced in *pp* collisions, where QGP is expected not to form. The number of *pp* collisions is scaled to the number of colliding nuclei in the ion collision. Figure 2.7 shows R_{AA} for charged

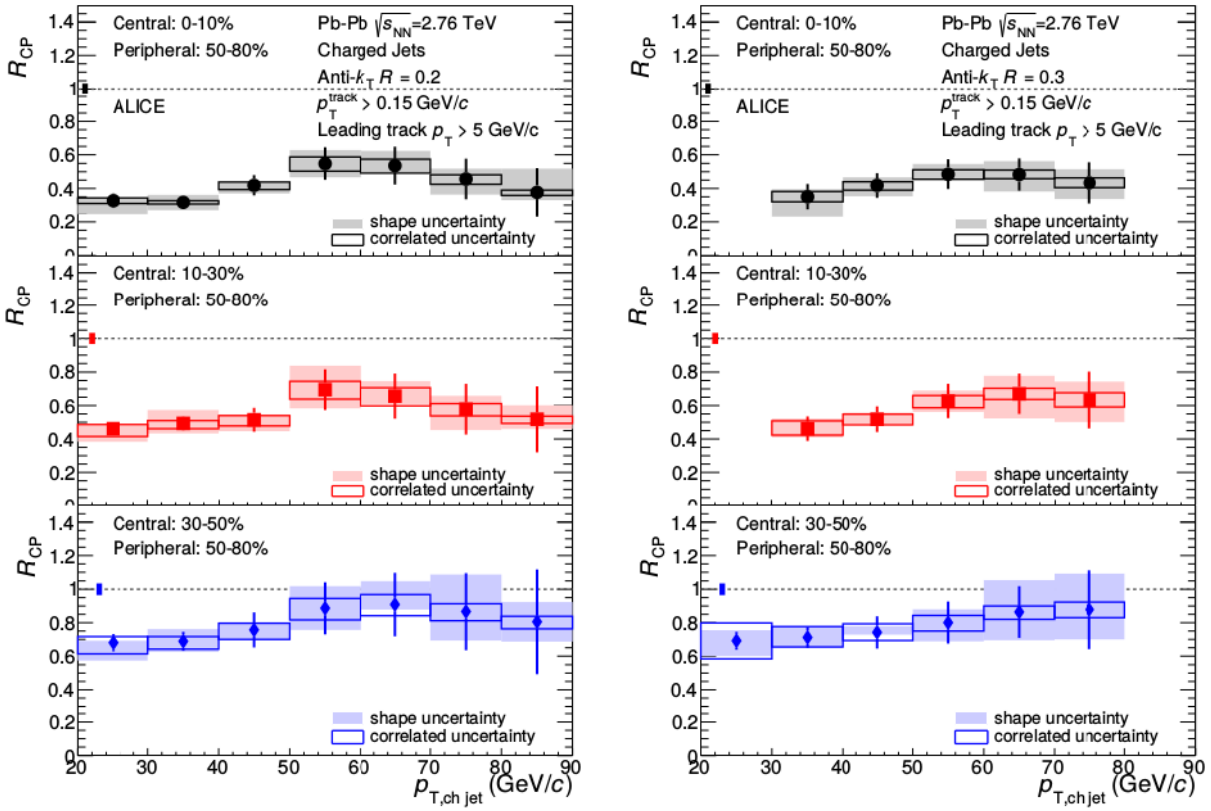

Figure 2.6: R_{CP} for charged jets of 3 different centralities from ALICE. A larger suppression for more central events is observed [28].

particles from ALICE, STAR and PHENIX all showing a suppression.

J/Ψ suppression

Studying the amount of quarkonia in an event can be another indicator of the presence of QGP. A quarkonium is a flavourless meson which is made up of a heavy quark and its own antiquark. Quarkonia consists of 2 types of particles, charmonium ($c\bar{c}$) and bottomonium ($b\bar{b}$). Toponium does not exist since the top quark decays before a bound state can be formed. The J/Ψ meson is the ground state of charmonium. Since heavy quarks are not present in the initial ions being collided, they must all be produced in the collision. A good way for these quarks to be produced is in quark-antiquark pairs. If these pairs are produced in a QGP medium it is more likely that they will be separated due to Debye screening of colour charges. Therefore when hadronization occurs the $q\bar{q}$ pair is less likely to be close to each other and more likely to combine with other quarks. This effect is present for all quarkonia but is most easily seen for the J/Ψ meson. This can be seen in

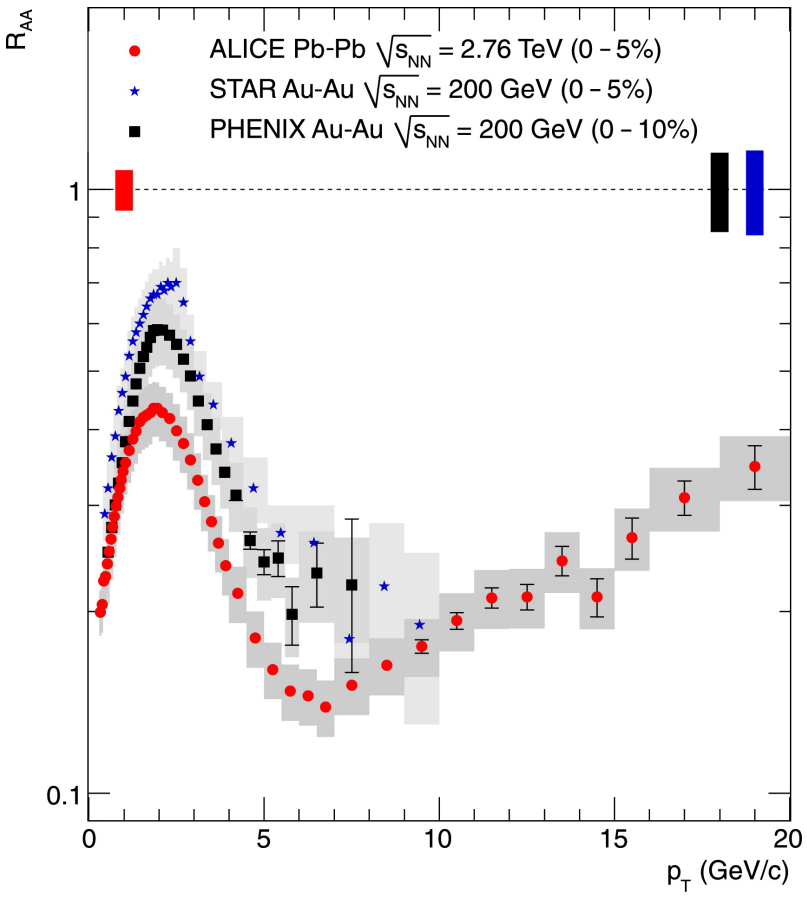

Figure 2.7: R_{AA} for charged particles from ALICE, STAR and PHENIX [29].

the ALICE measurements of the nuclear modification factor R_{AA} for J/Ψ mesons shown in figure 2.8. The figure shows the ratio of the yield of J/Ψ mesons in Pb-Pb collisions to the scaled yield of J/Ψ mesons in pp collisions. A clear supression can be seen indicating the presence of QGP.

Strangeness enhancement

In the initial interaction of colliding nuclei a certain number of strange quarks is produced in hard collisions. This number of s quarks might be suppressed compared to the number of u and d quarks due to the higher masses of s quarks, but additional s quarks can be produced in the presence of QGP. In such a medium, the production of additional $u\bar{u}$ and $d\bar{d}$ pairs might be suppressed due to their large numbers and the Pauli exclusion principle and so the creation of $s\bar{s}$ pairs would be enhanced despite their larger mass. The temperature of the QGP medium is higher than the energy of an $s\bar{s}$ pair so their production is possible, for example via gluon fusion. ALICE measurements

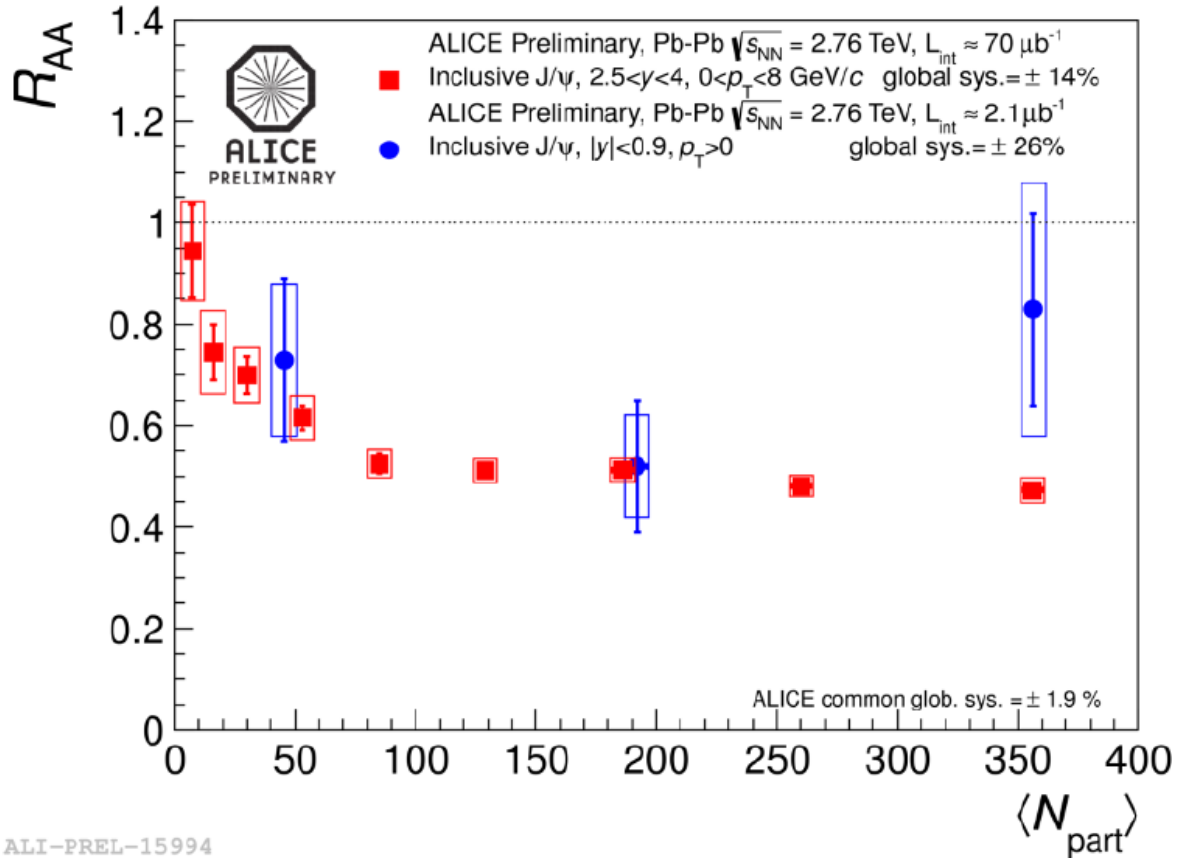

Figure 2.8: R_{AA} for J/Ψ mesons from ALICE [30].

of strangeness enhancement in Pb-Pb collisions can be experimentally seen in figure 2.9. The plot shows a clear enhancement of strange hadrons and that as the multiplicity of the event increases, there is an increase in the enhancement. The enhancement is also higher for hadrons composed of more strange quarks with the enhancement being highest for the omega baryon which is composed of 3 strange quarks and lowest for the lambda baryon which contains only a single strange quark.

Flow

If the QGP that is produced in heavy-ion collisions behaves like a drop of perfect liquid, then signatures in the final state particles resulting from the hydrodynamic flow of the drop would be an important signature of the QGP itself. Studying flow in QGP systems can give us information on various properties of the system such as the viscosity, the initial conditions and the equation of state of the system, mainly regarding the different phases present in the system. The flow in the transverse plane is the most interesting

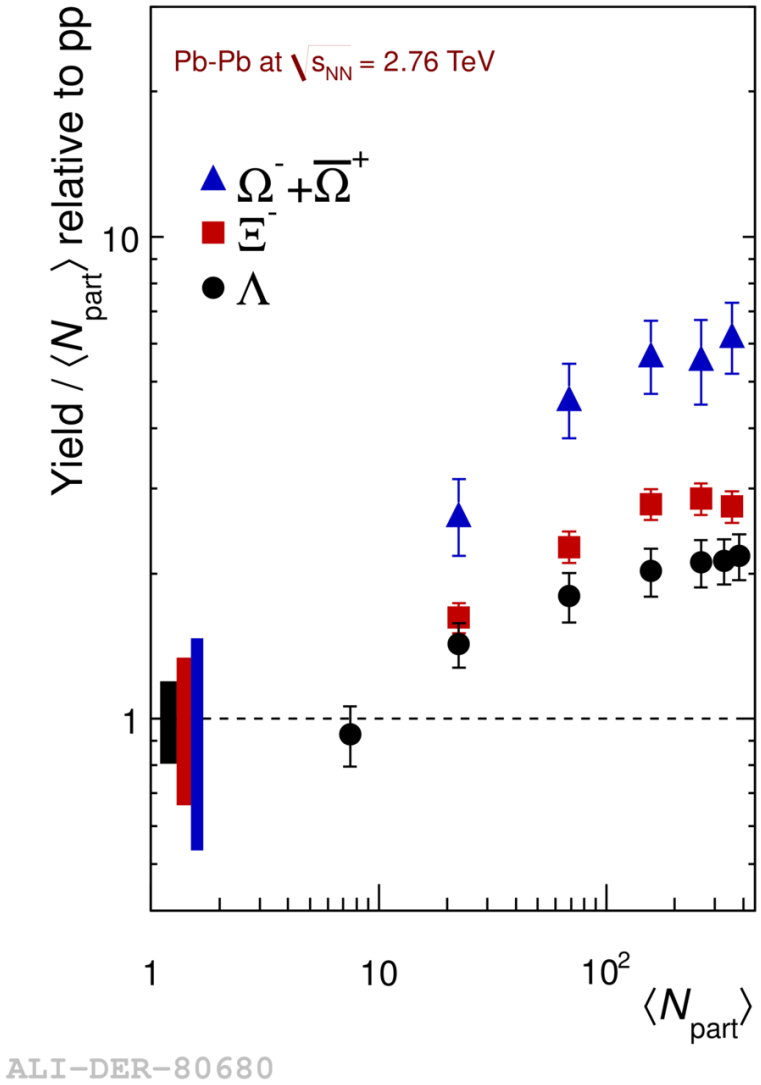

Figure 2.9: ALICE measurements showing the yields of strange hadrons in Pb-Pb collisions relative to *pp* collisions. The plot shows an increase in yield with both multiplicity and hadron strangeness content [31].

since it can only arise as a result of a pressure gradient between the dense system and the vacuum surrounding it. The existence of hydrodynamic flow is what changed the mind of physicists from thinking about QGP as a weakly interacting gas to a strongly-coupled liquid.

The flow in the transverse plane can be separated into a radial and an anisotropic flow. The radial flow is the component of the flow that describes the isotropic expansion of the particles. The anisotropic flow is the more interesting of the two components. It measures the momentum space anisotropy of particle emission as a function of the azimuthal angle. This anisotropy arises from the fact that not all collisions occur perfectly centrally and so

the overlapping parts of the two colliding nuclei do not form a round shape when looking along the beam line, but an almond shape. A schematic illustration of this can be seen in figure 2.10. There is a difference in the pressure gradient between the centre and the edge of the medium for different azimuthal angles. Different pressure gradients lead to differences in the momentum distribution of the emitted particles.

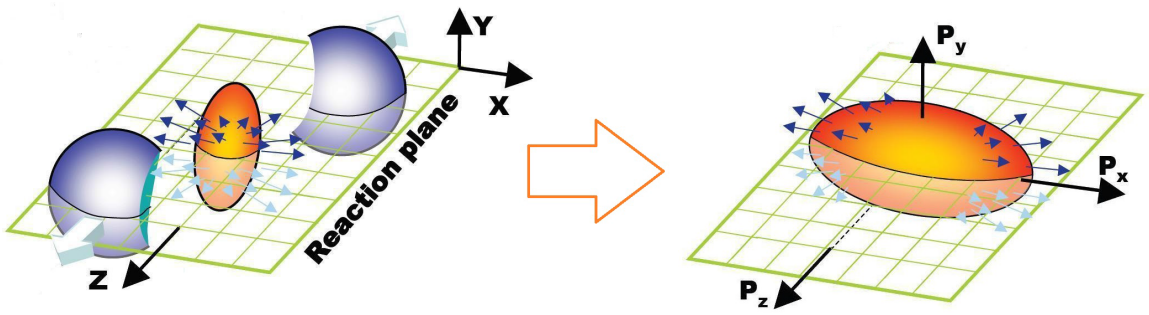

Figure 2.10: An illustration of the almond shaped impact region resulting from a semi-central heavy ion collision on the left as well as the corresponding momentum space anisotropic expansion on the right.

An interesting way to qualitatively describe the anisotropy in the flow is to calculate the azimuthal Fourier decomposition of the momentum distribution. This can be done as a sum over the cosines for each harmonic where each term will represent a different shape of anisotropy: $1 + 2v_1 \cos[\phi - \Psi] + 2v_2 \cos[2(\phi - \Psi)] + 2v_3 \cos[3(\phi - \Psi)] + \ldots$. The coefficients v_n accompanying each term can be calculated by $v_n = \langle \cos[n(\phi - \Psi_n)] \rangle$, where ϕ is the azimuthal angle, Ψ represents the angle of the reaction plane and n represents the order of the harmonic. The magnitude of the coefficient v_n represents how anisotropic the events are. The largest contribution to anisotropic flow and most commonly studied component is v_2 and is known as elliptic flow. As its name suggests, it represents how elongated the flow is in the shape of an ellipse. Figure 2.11 shows ALICE v_2 measurements as a function of centrality[1]. It can be seen that in events with small centralities v_2 is also small but increases as centrality increases. This is because as a larger part of the ion participates in the collision, there exists a larger probability for QGP to form. However, as centralities get very large, v_2 starts to fall again since the overlapping part of the two nuclei start to

[1]Centrality is a variable in heavy-ion collisions that measures the overlap of the two colliding nuclei from 0% (head-on collision) to 100% (nuclei miss each other).

approach a circular shape. Other higher orders of v_n are also interesting to look at. While all odd coefficients (such as v_3, also known as triangular flow) were originally expected to vanish for symmetry reasons, fluctuations in the positions of the partons in the colliding ions in the initial state can lead to non-zero contributions of these higher coefficients.

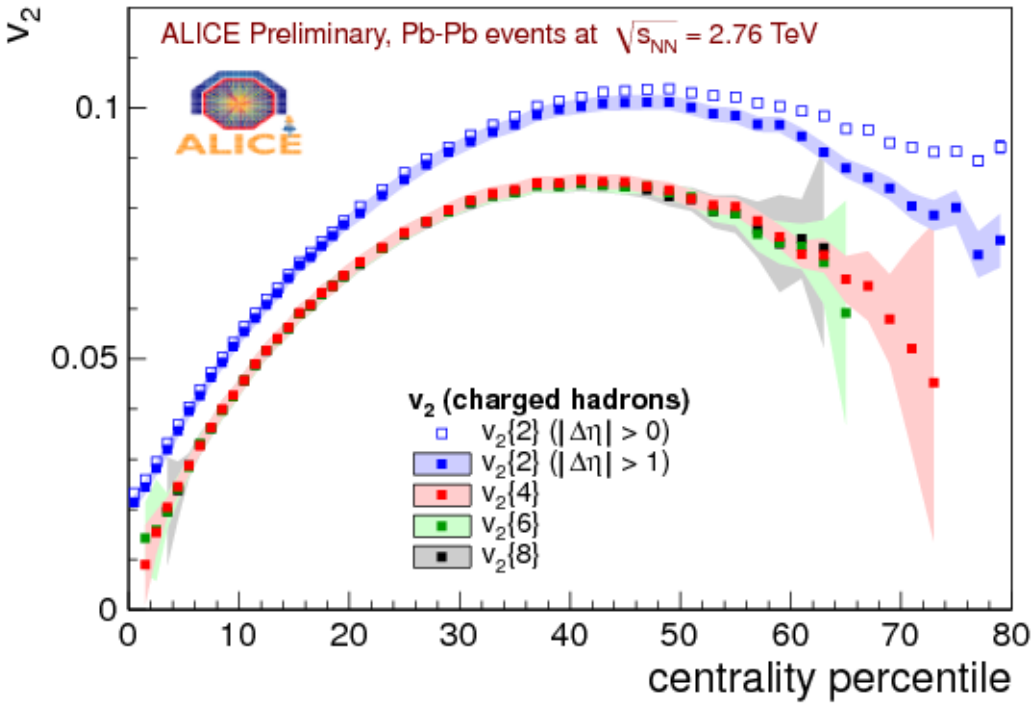

Figure 2.11: ALICE measurement of elliptic flow dependence on centrality, measured for Pb-Pb collisions at $\sqrt{s_{NN}} = 2.76$ TeV [32].

The Ridge

The ridge is a long range angular correlation whose presence could be dependent on the existence of QGP in the system. This is the main topic of this thesis and is explained in detail in the next Chapter.

2.3 Heavy-ion collisions

The most useful tool for studying the strong interaction are ultra-relativistic heavy-ion collisions. They are also the only known experimentally viable way of studying quark-gluon plasma. The LHC collides lead nuclei with a centre-of-mass energy of around 5.5 TeV/nucleon which corresponds to speeds of more than 99.9999% the speed of light. At these speeds, the Lorentz factor is on the order of $\gamma \sim 1000$ so the colliding nuclei can be thought of as flat pancakes colliding head-on due to relativistic length contraction. An example of this can be seen in figure 2.12. The parameter b in the image is called the impact parameter and is defined as the distance between the centres of the two nuclei. This can be used to quantify the overlap or centrality of the collision with $b = 0$ corresponding to a perfectly central collision and $b > 2R_{nucleus}$ corresponding to two nuclei that miss each other. The nucleons in the nuclei can be separated into two groups. Participants are the nucleons that are in the region of overlap of the two nuclei and undergo collisions. Spectators are the nucleons that are outside the region of overlap of the two nuclei and do not participate in the collisions. Measuring the number of spectators can indirectly tell us about the number of participants in the collision and can therefore be used to determine certain parameters of the event such as centrality.

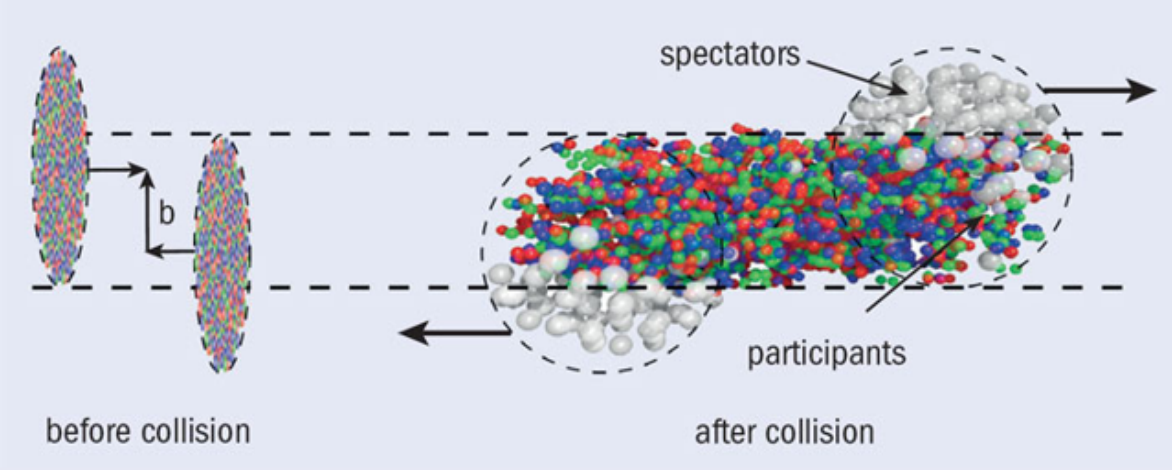

Figure 2.12: An illustration of heavy ions colliding in a high energy collision [33].

2.3.1 Heavy-ion collision evolution

There are several stages in the evolution of a heavy-ion collision starting from the collision itself and ending with the hadrons that fly out into our detector. A schematic of this evolution can be seen in figure 2.13 represented on a space-time diagram for both the cases where (a) QGP is not formed and (b) QGP is formed. Since QGP is the phenomenon of interest, only case (b) will be discussed.

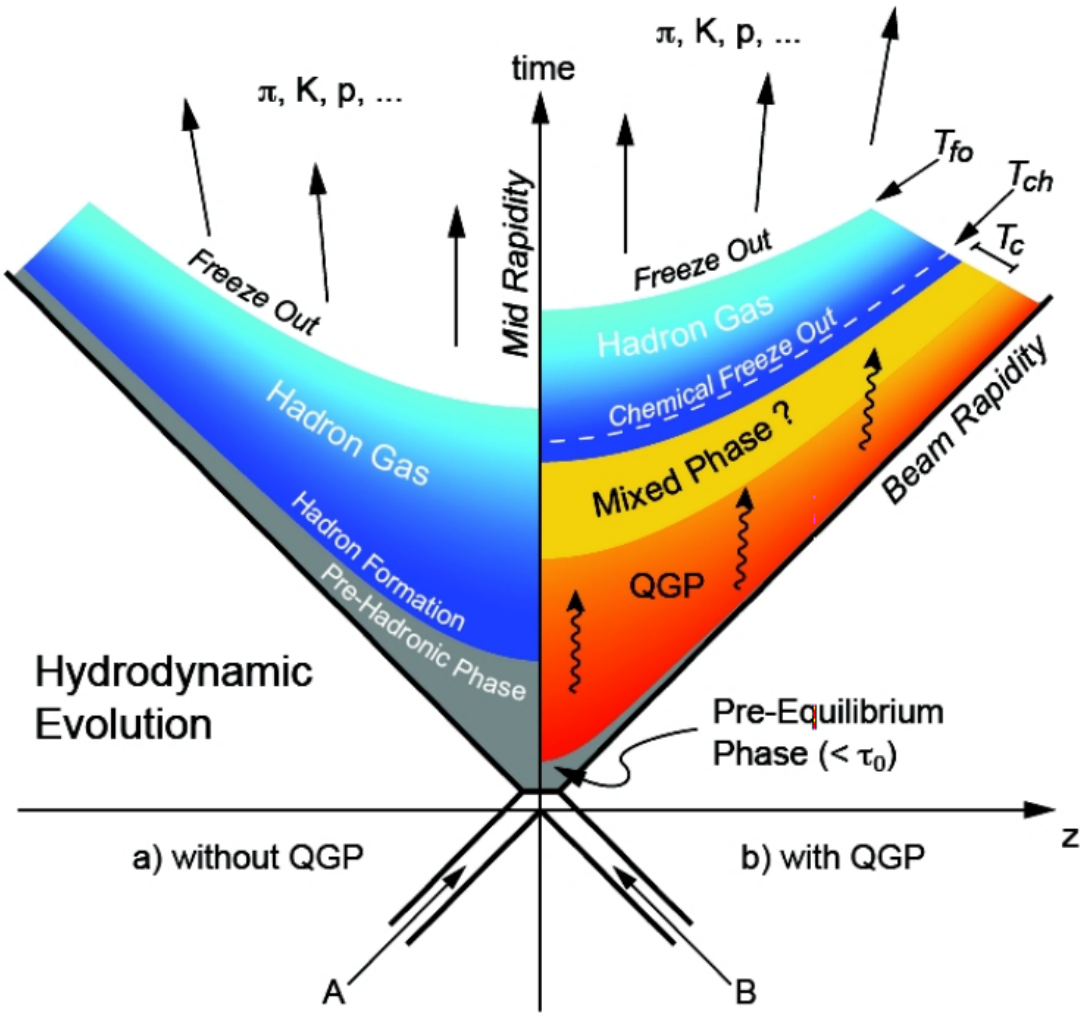

Figure 2.13: The evolution of a system created in a heavy-ion collision assuming (a) no QGP is formed and (b) QGP is formed [34].

The evolution of the collision starts with two flat, length-contracted nuclei moving towards each other. As the nuclei move through each other, individual nucleons collide and deposit much of their energy producing various partons in hard processes. The method in which these partons are created is not completely understood as these production

processes cannot be calculated perturbatively. This is a pre-equilibrium state as the partons have not yet had enough time to interact with many of their neighbours and thermalize. As the partons interact they thermalize and QGP is formed. In this phase relativistic hydrodynamics can be used to describe the system. The QGP behaves like a near-perfect liquid, expanding due to pressure gradients according to the laws of hydrodynamics and producing collective flow which boosts particles radially outward. As the system expands it cools until the temperature and energy density drop below the critical values for QGP to exist. The partons in the QGP start to combine into hadrons, temporarily forming a mixed phase until all of the partons are confined to hadrons. This moment is called chemical freeze-out, where the system fully transitions into a hadron gas and the chemical composition of the system becomes fixed. The system is referred to as a hadron gas since the hadrons can still participate in elastic scatterings with each other so energy can still be exchanged. After some time the system becomes too spread out for any interactions to occur between particles. This is known as kinetic freeze-out, after which the particles fly out into the detector maintaining their trajectories and momenta.

Chapter 3

Two-particle angular correlations

This chapter will discuss two-particle angular correlations. These correlations are a useful tool to study the mechanisms of particle production, the dynamics of the collision process and the properties of the produced medium. The observables used in this work will be discussed first followed by the definition of the correlation function and finally an overview of the origin of structures in it.

3.1 Observables

The correlation function in this work is defined in terms of the azimuthal angle φ and pseudorapidity η. These coordinates are better suited to studying high energy particle collisions when compared to traditional Cartesian coordinates. These two observables are enough to indicate in which direction the particle left the interaction point. The system which consists of two particles colliding in opposite directions in a point contains two symmetries around which it makes sense to build a coordinate system. Firstly, there is a cylindrical symmetry to the system with the main axis (z) being the one along the beam line, with the transverse plane being defined as the plane perpendicular to the main axis. The x and y coordinates would be in this transverse plane but their position is quite arbitrary since all directions perpendicular to the main axis should be equivalent. Secondly, there is a spherical symmetry to the system since the collision and subsequently produced particles occur in a point and the particles that they produce fly out in all directions from that point. Therefore some combination of the spherical and cylindrical coordinate systems should be used to most effectively describe the colliding system.

3.1.1 Azimuthal angle

Both the cylindrical and spherical coordinate systems have the azimuthal angle φ in common, so it makes sense to use it as one of coordinates. The azimuthal angle φ is zero at the positive x axis increasing towards the positive y axis. The φ of a particle is defined as the angle between the projection of the particle's momentum in the transverse plane p_T and the positive x-axis:

$$cos\,(\varphi) = \frac{p_x}{p_T}. \tag{3.1.1}$$

The value of the angle φ of a single particle is meaningless, and depends entirely on where we choose to define the position of the positive x-axis. However, the difference in the azimuthal angle between two particles is independent on the axis we choose as the zero value of the azimuthal angle:

$$\Delta\varphi = \varphi_2 - \varphi_1. \tag{3.1.2}$$

If two particles are produced independently then all values of $\Delta\varphi$ are equally likely. On the other hand, if they are produced in the same event and are correlated in some way then we expect some values of $\Delta\varphi$ to be more likely than others depending on how the particles were produced and the physical mechanisms between them.

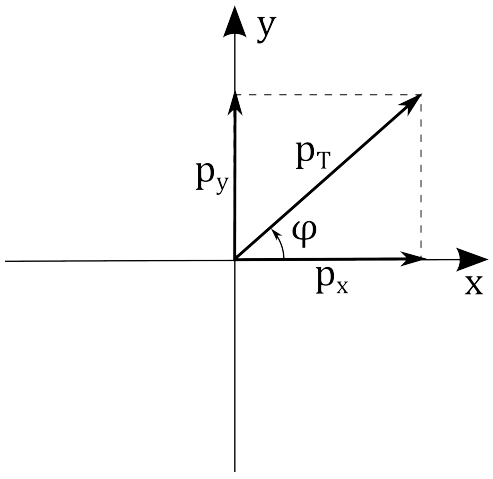

Figure 3.1: Definition of the azimuthal angle φ in the transverse plane.

3.1.2 Pseudorapidity

The remaining two coordinates z and θ in our chosen coordinate systems (cylindrical and spherical respectively) can both be useful when considering our particular system. Since the collisions are not always perfectly centred, z can be used to describe the position of the original collision (see chapter 4 about LHC and the ALICE detector). The polar angle θ is also a useful coordinate when observing the system in the reference frame of the center of mass. The polar angle θ is zero at the positive z axis increasing to π at the negative z axis:

$$cos\,(\theta) = \frac{p_z}{|\vec{p}|}. \tag{3.1.3}$$

While the azimuthal angle is a useful coordinate for most high energy physics research, the polar angle is not the most reliable of coordinates. This is because the protons within the colliding bunches (and partons within the protons) are not stationary but moving within the bunches (protons) (see chapter 4). This means that even though the particles collide from both sides in (or close to) the origin of the coordinate system, the centre of mass of the collision could have a net velocity different from zero in that system, causing a boost along the z axis. The difference in the azimuthal angles between two produced particles will not depend on this boost. However, the difference in the polar angles between the same particles would depend on the boost. That is why the most common substitute coordinate for θ in high energy physics is pseudorapidity η (or rapidity y for lower energies).

Pseudorapidity is defined as:

$$\eta \equiv -\ln\left[\tan\left(\frac{\theta}{2}\right)\right]. \tag{3.1.4}$$

This would give a value of $\eta = 0$ to particles in the $x - y$ transverse plane ($\theta = \frac{\pi}{2}$) increasing to ∞ as θ goes to 0 and symmetrically to $-\infty$ as θ goes to π. Pseudorapidity can alternatively be defined in terms of the particle momentum $\vec{p}$ and the projection of that momentum on the z axis p_z:

$$\eta = \frac{1}{2}\ln\left[\frac{|\vec{p}| + p_z}{|\vec{p}| - p_z}\right] \tag{3.1.5}$$

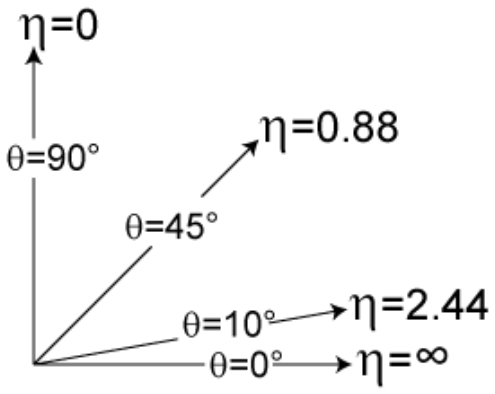

Figure 3.2: Comparison of pseudorapidity to the polar angle θ.

In the limit where the speed of a particle approaches the speed of light (or in the case where the particle mass is negligible), the energy of a particle can be approximated with its momentum:

$$E = \sqrt{(mc^2)^2 + (pc)^2} \approx pc. \tag{3.1.6}$$

Since in this limit $mc \ll p$ and therefore the particle's pseudorapidity converges with its rapidity $\eta \approx y$:

$$y = \frac{1}{2} ln \left[\frac{E + p_L}{E - p_L} \right]. \tag{3.1.7}$$

Rapidity and pseudorapidity are better variables to observe relativistic systems since they are defined using logarithms. Since a boost along the z axis adds a multiplicative factor of γ to all particles, taking the logarithm would cause this multiplicative factor to become additive and cancel out when looking at the difference in pseudorapidities (rapidities) between two particles. Rapidity is also useful since particle production is constant as a function of rapidity. Therefore the difference in pseudorapidity $\Delta\eta$ will be taken as an observable in this analysis:

$$\Delta\eta = \eta_2 - \eta_1. \tag{3.1.8}$$

Pseudorapidity is chosen over rapidity because it is easier to measure. Rapidity requires two independent properties of the particle to be measured simultaneously, such as energy

and momentum (mass), which can be difficult. On the other hand, pseudorapidity requires only the particle's momentum vector to be measured.

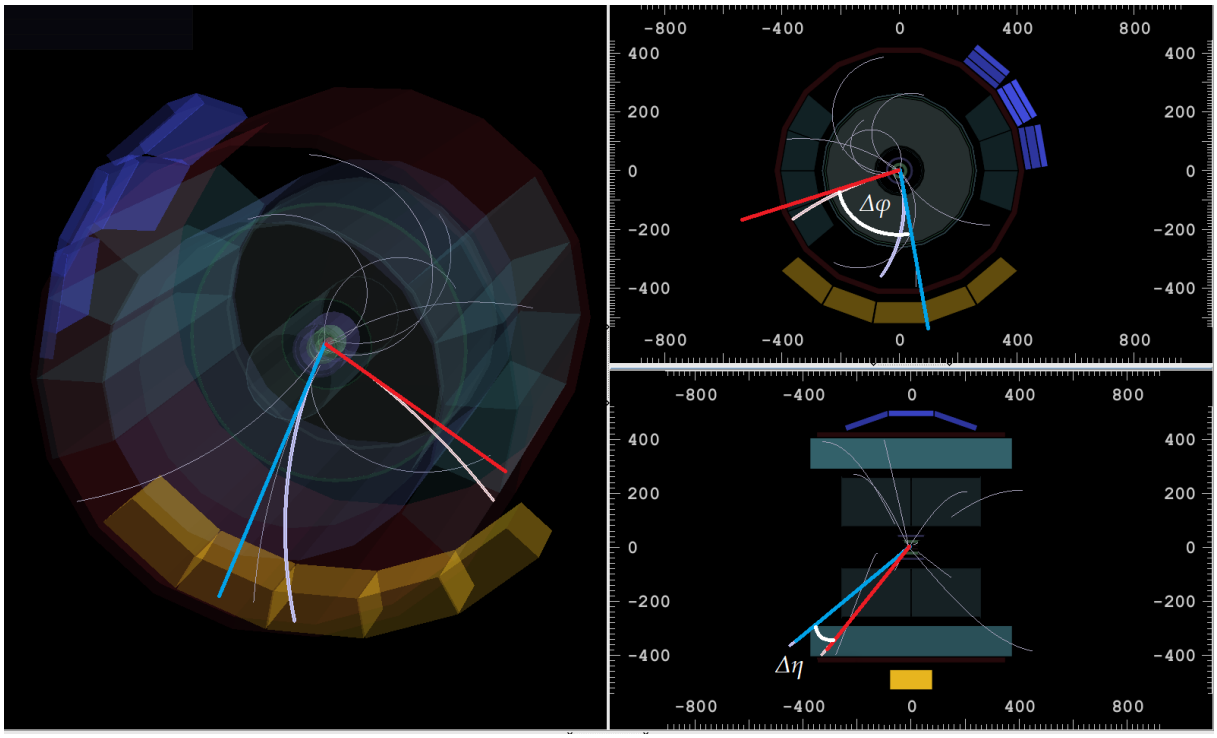

Figure 3.3: An example of a pp collision event taken by the ALICE detector with 10 produced particles. The initial trajectories of two of the particles are shown in red and blue (left image). The difference in the particle's azimuthal angles $\Delta\varphi$ can be seen in the top right figure showing the transverse plane by looking along the beam pipe. The difference in the particle's pseudorapidity $\Delta\eta$ can be seen in the bottom right figure showing the ALICE detector from the side with the beam passing left to right.

3.2 Correlation function

The correlation function $C(\Delta\eta, \Delta\varphi)$ gives a measure of the angular distribution of particles relative to one another. It is calculated by looking at the differences in η and φ between pairs of particles in an event. The simple distribution of these differences within a single event can be defined as follows:

$$S(\Delta\eta, \Delta\varphi) = \frac{\mathrm{d}^2 N_{\text{pairs}}^{\text{signal}}}{\mathrm{d}\Delta\eta \mathrm{d}\Delta\varphi}. \tag{3.2.1}$$

It is usually constructed in such a way that the particles in an event are separated into two groups, the trigger particles and the associated particles (a single particle can belong

to both or neither of these groups). These groups are defined in terms of some physical characteristic, such as p_T, where the group of trigger (associated) particles can be defined as all particles in the event that fall into a certain p_T range. These ranges can overlap or can even include all particles in the event in which case we call the correlation function untriggered. In this analysis the trigger and associated particles come from the same p_T range.

Each of the trigger particles is compared to each individual associated particle and the difference in their η and φ is calculated and added to the distribution. This gives a measure of how particles tend to be distributed in an event or more precisely, for a given particle, what is the probability that we will find another particle in a certain part of the $\Delta\eta - \Delta\varphi$ phase space. For example, a peak around $\Delta\eta = 0$ and $\Delta\varphi = 0$ would tell us that particles tend to be clumped up together.

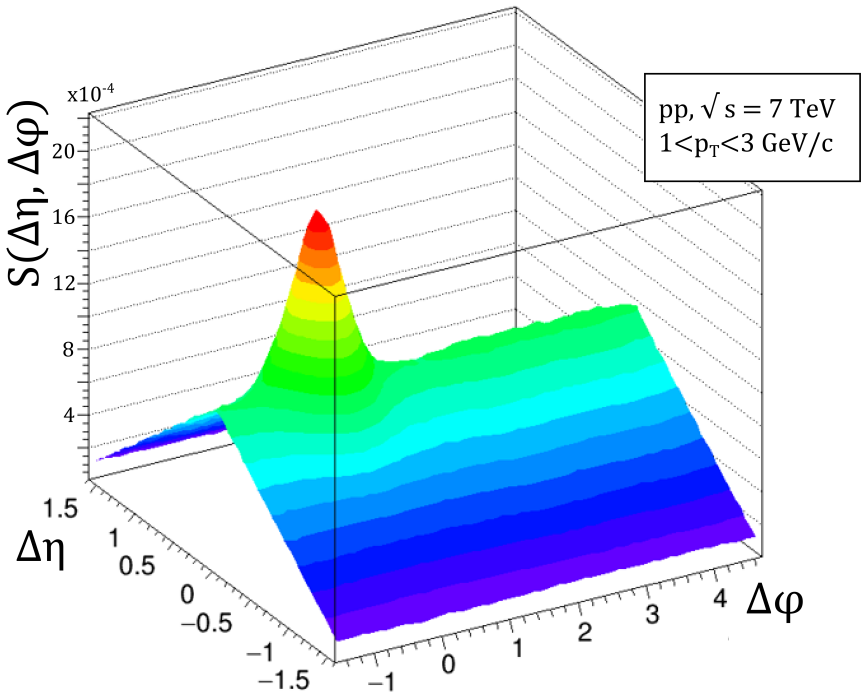

Figure 3.4: An example of a scaled $S(\Delta\eta, \Delta\varphi)$ distribution.

This distribution includes physical two-particle correlations which are of interest to us, however, it also includes trivial two-particle and correlation structures due to detector acceptance and single-particle distributions. In order to avoid the background of these trivial effects masking the real physical correlations, we create another correlation distribution

as follows:

$$B(\Delta\eta, \Delta\varphi) = \frac{\mathrm{d}^2 N_{\mathrm{pairs}}^{\mathrm{mixed}}}{\mathrm{d}\Delta\eta \mathrm{d}\Delta\varphi}. \tag{3.2.2}$$

This distribution takes trigger particles and associated particles from different events. Since both of these groups still come from the same physical system and are measured by the same detector, the $B(\Delta\eta, \Delta\varphi)$ distribution will still include the trivial correlations due to the detector acceptance as well as any single-particle distributions. It will not, however, contain any information about any physical two-particle correlations since the two particles come from separate events and there is no way for them to be correlated. To improve the quality of this signal, each of the events is mixed with ten other events that are similar to it (have similar multiplicities and primary vertex locations).

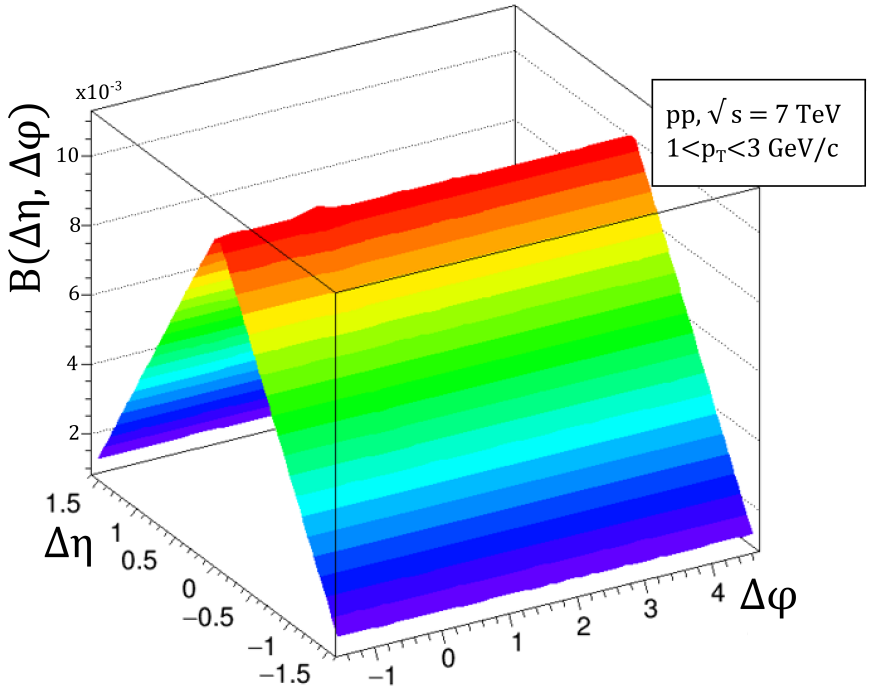

Figure 3.5: An example of a scaled $B(\Delta\eta, \Delta\varphi)$ distribution.

An example of a trivial effect relating to single-particle detector acceptance is the triangle shape in $\Delta\eta$ in both the $S(\Delta\eta, \Delta\varphi)$ and $B(\Delta\eta, \Delta\varphi)$ distributions. This shape comes from the fact that the pseudorapidity range of our detector is limited. This means that the pseudorapidity of each individual particle follows a uniform distribution from η_{min} to η_{max}. The distribution coming from the sum or difference of two such finite uniform

distributions is the convolution of those two uniform distributions and has a triangle shape ranging from the smallest to the largest possible value.

The correlation function $C(\Delta\eta, \Delta\varphi)$ is constructed by dividing the $S(\Delta\eta, \Delta\varphi)$ distribution also called the Signal distribution by the $B(\Delta\eta, \Delta\varphi)$ distribution also called the Background distribution:

$$C(\Delta\eta, \Delta\varphi) = \frac{\frac{1}{N_{\text{pairs}}^{\text{signal}}} S(\Delta\eta, \Delta\varphi)}{\frac{1}{N_{\text{pairs}}^{\text{mixed}}} B(\Delta\eta, \Delta\varphi)}. \tag{3.2.3}$$

The distributions are normalized before dividing so $N_{\text{pairs}}^{\text{signal}}$ is the number of particle pairs in the signal distribution and $N_{\text{pairs}}^{\text{mixed}}$ is the number of pairs of particles in the background distribution. The correlation function can further be normalized by the factor $\frac{B(0,0)}{N_{\text{pairs}}^{\text{signal}}}$ where $B(0,0)$ is the value of the background function in its highest point $(0,0)$ causing the new normalized background function to have a maximum at 1. Normalized in this way, the correlation function itself becomes normalized and describes the Associated yield per trigger particle, or in other words, the integral of the function in some $\Delta\eta\Delta\varphi$ interval describes the probability of finding an associated particle in that interval around a certain trigger particle.

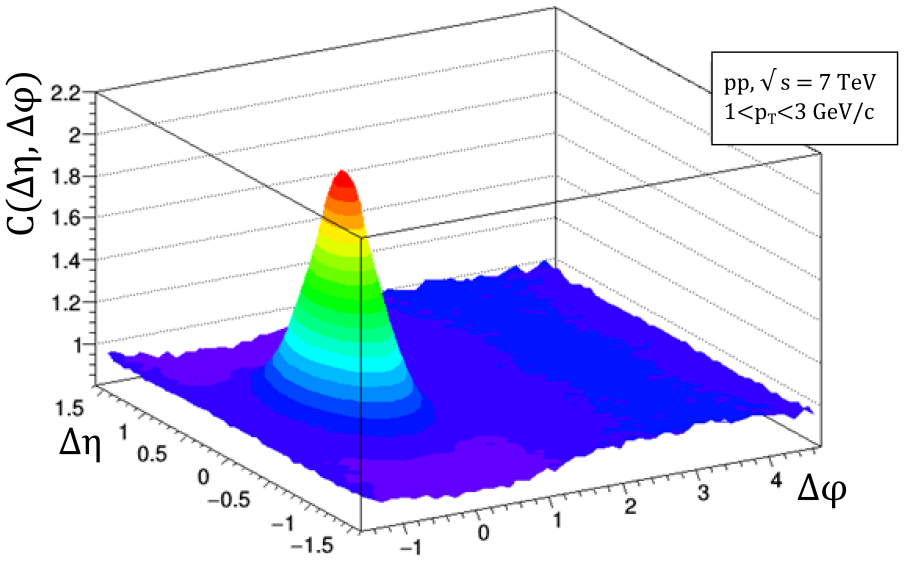

Figure 3.6: An example of the correlation function $C(\Delta\eta, \Delta\varphi)$.

3.3 Correlation sources

The correlation function gives us an overall picture of all the correlations present in our system. This overall correlation is composed of many different overlapping sources. Each of these sources correlates the particles in different ways, causing a different structure in the correlation function. These sources include conservation laws, jets and minijets, Bose-Einstein correlations, resonances, photon conversions, gluon strings, Coulomb interactions, flow, the Ridge, etc. In this section we will discuss the physical origin of some of these sources as well as how they manifest in the correlation function. The main goal of this analysis is to test whether some of these structures, particularly the Ridge, can be isolated by studying the shape of the events and obtaining some information about them individually.

3.3.1 Origin of correlation sources

Conservation laws

Conservation laws state that in an isolated physical system, a particular measurable property of that system does not change over time. The laws of conservation of energy and momentum are amongst the most important and universal principles in physics. These are examples of exact conservation laws which are conserved in all types of physical processes. Other quantities of a system that are exactly conserved are angular momentum and electric and colour charges. Baryon and lepton numbers are also conserved exactly in the standard model of physics, however, since phenomena have been discovered outside of the standard model, physical processes could theoretically exist which violate the conservation of baryon and lepton numbers, meaning they are governed only by approximate conservation laws. Each of the exact conservation laws is a result of a differentiable symmetry of nature. For example, the conservation of momentum arises from the fact that there is a translational symmetry in the physical system (i.e. there is no absolute coordinate system), while the conservation of energy follows from the time invariance of the system (the coordinate $t = 0$ can be placed anywhere, just the relative times between events are important). Finally, these exact conservation laws have to be valid locally in addition to being valid globally (i.e. on the scale of the entire universe). If some amount of energy were to appear in

one location at the same moment that it disappears in another location, the total energy in the system would be conserved (only from the inertial reference frame in which these two events occur simultaneously). Other inertial reference frames exist where the events would not be simultaneous breaking the conservation law. The exact conservation laws require that there must be a flux of the quantity into or out of a point for the amount of the conserved quantity to change in that point.

The collision system in this experiment consists of two protons colliding head-on along a single axis. Each collision is an independent and an isolated system, so there are many quantities that should be conserved. In the reference frame of the lab, the initial system has a baryon number of 2, a lepton number of 0 and most importantly zero momentum in the transverse plane. The momentum conservation influences the shape of the correlation function, especially in collisions with fewer produced particles. For momentum in the transverse plane to be conserved, for each particle leaving the interaction point in one direction (φ) we expect a deficit of particles going in the same direction and an excess of particles going in the opposite direction. In other words, in our correlation function we expect a deficit around $\Delta\varphi = 0$ and an excess around $\Delta\varphi = \pi$ which can be seen in figure 3.7.

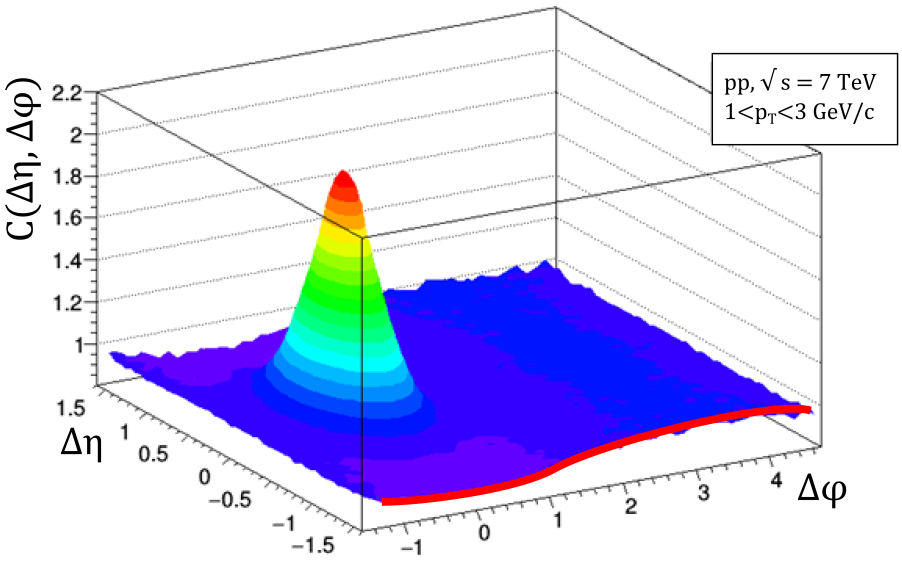

Figure 3.7: Momentum conservation contribution to the correlation function $C(\Delta\eta, \Delta\varphi)$ (marked in red).

The same cannot be said about the momentum along the beam axis since the protons oscillate back and forth within their bunches before collision (see chapter 4) so the centre of mass of the collision could have some net velocity in the laboratory system, but only along the direction of the beam.

Momentum conservation is also important when analysing the jet contribution to the correlation function which is discussed in the next subsection.

Jets

A jet is a narrow cone of particles, mainly hadrons, produced by the hadronization of a gluon or a quark. Since quarks and gluons carry a colour charge they cannot exist by themselves due to colour confinement which allows only a colourless state. If a colourless object containing quarks and gluons fragments, each fragment carries some of the colour charge so each fragment individually is not colourless. In order to obey QCD confinement, these fragments create other coloured objects until all objects are colourless. Since the original fragments tend to have a high momentum (which is needed in order to eject them from the original object) all of the created objects tend to travel at high speeds in the same direction as the original fragment. This group forms a narrow collimated "jet" of particles and is therefore simply called a jet. Minijets are a subset of jets that have an anomalously small number of particles in the jet and are often narrower than typical jets of similar energies. They are an interesting subset of jets because they can be produced by simple processes such as a hadronic decay of a tau lepton. It is hypothesised that several signals of new physics beyond the Standard Model could produce minijets.

Events containing jets often contain more than one jet. This occurs since if a colourless object loses a coloured fragment, the remainder of the fragments must have some net colour as well. All of the coloured fragments will create their own jets travelling in their original directions. Furthermore, the total momentum of all of these fragments needs to be conserved when compared to the original object meaning the jets need to fly out in opposite directions when looking in the reference frame of the original object. The simplest and most prevalent case is that of two jets that travel in opposite directions called back-to-back jets. When looking at an event with only two back-to-back jets in the lab system we can observe that they fly out at an azimuthal angle of $\varphi = \pi$ one from the

other since the original momentum in the transverse plane was zero and it is the only way for the total momentum of the system to be conserved. The same cannot be said for the difference in their polar angle and their pseudorapidity since they might have some unknown boost along the beam line. These two effects create two distinct structures in the shape of the $\Delta\eta - \Delta\varphi$ correlation function. When comparing the angles of the particles to one another we have the case where both of the particles come from the same jet. In this case the particles will be travelling in the same direction with very similar values for their η and φ giving small values of both $\Delta\eta$ and $\Delta\varphi$. This effect produces a peak centred around $(\Delta\eta, \Delta\varphi) = (0, 0)$ which is called the near-side peak. The second effect comes from the case where the two particles come from different jets. The $\Delta\varphi$ of these particles will be around π and the $\Delta\eta$ of these particles will be some value depending on the boost of the original source. Since the particles in both of the jets are very collimated, this second case will produce a peak centred around $(\Delta\eta, \Delta\varphi) = (\Delta\eta', \pi)$ where $\Delta\eta'$ is the angle in η between the centres of the two jets.

The correlation function is not calculated for a single event but for many events. Adding the contributions from each pair of back-to-back jets from different events will cause the nearside peak to become large since they are all adding to the same part of the $\Delta\eta - \Delta\varphi$ phase space. On the other hand, each pair of back-to-back jets will be separated by a different angle in η so the total contribution from the pairs of particles taken from different jets will cause the peaks at $\Delta\varphi = \pi$ to blend together forming a wide uniform distribution in $\Delta\eta$ centred around $\Delta\varphi = \pi$. This structure is called the away-side-ridge. The contributions to the correlation function from jets can be seen in figure 3.8.

Bose-Einstein correlations

A substantial fraction of the particles produced in high energy collisions are mesons. Since mesons have integer spins they are bosons and they obey Bose-Einstein statistics. In contrast we have fermions which are particles with a half-integer spin. When looking at the total wavefunction comparing 2 identical particles, the wavefunction for particles of integer spins must be symmetric under the exchange of the particles whereas the wavefunction for particles of half-integer spins must be antisymmetric. This means that for fermions the wavefunction vanishes identically if the particles are in the same state, meaning that the probability of them occupying the same state is zero, or in other words that it is impossible

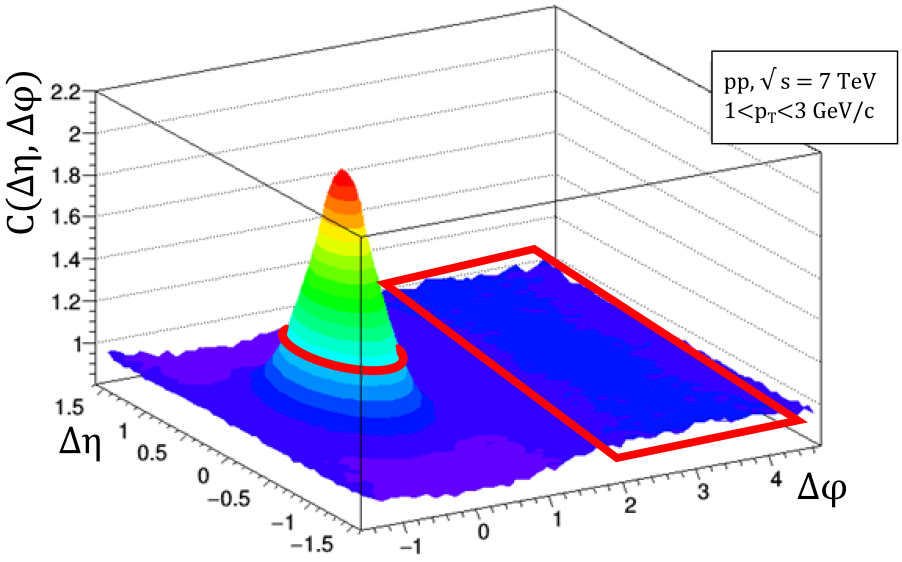

Figure 3.8: Jet contributions to the correlation function $C(\Delta\eta, \Delta\varphi)$ (marked in red).

for both fermions to occupy the same state. This effect is known as the Pauli exclusion principle and manifests as an apparent force that repels the two fermions. The opposite is true for bosons with their wavefunction being larger if they are in the same state meaning that there is an increased probability for two identical bosons to occupy the same state. This manifests as an apparent attractive force between the bosons so to us it appears as if they are emitted in similar directions. This adds an additional contribution to the near side jet peak of the correlation function shown in figure 3.9.

Resonances

Resonances, also called resonance particles, are particles that are formed in hard processes that have an exceptionally short half-life. They decay so quickly that even travelling at the speed of light they barely traverse the diameter of a proton meaning that for us they decay in the same location as the hard process that produced them. The decay of the resonance will occur isotropically in its rest frame. The contribution of the resonance to the overall correlation function depends on the original momentum of the resonance as well as the energy of decay of the resonance in its rest frame. If the original momentum of the resonance is high and the decay energy of the resonance is low, the produced particles will fly out together in the original direction of the momentum

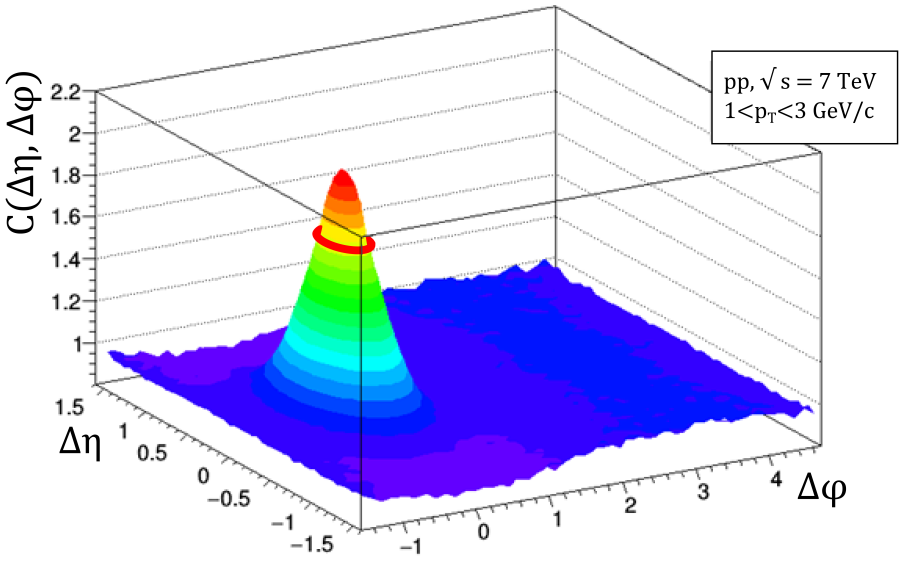

Figure 3.9: The Bose-Einstein correlation contribution to the correlation function $C(\Delta\eta, \Delta\varphi)$ (marked in red).

of the resonance contributing to the near side jet peak. On the other hand, if the decay energy of the resonance is large and there are several decay products, the differences in azimuthal angles between the particles will tend to be random but they will be more likely to fly out at similar pseudorapidities. This creates a ridge structure perpendicular to the away-side-ridge called the longitudinal ridge structure, located at $\Delta\eta = 0$ and spreading over the entire range in $\Delta\varphi$ shown in figure 3.10.

Photon conversion

Photon conversion is a type of pair production where a particle and its antiparticle are produced from a neutral boson, in this case a photon. This most often refers to a photon creating an electron-positron pair but it can also result in the production of a muon-antimuon pair or a proton-antiproton pair. Pair production requires the energy of the photon to be at least the sum of the rest masses of the particle and antiparticle (or simply twice the rest mass of the particle) for energy to be conserved as well as for there to be an additional object nearby that interacts with the photon, so that momentum can be conserved. The particles that we take into account when calculating the correlation function have significantly higher energies than the rest mass of an electron so if any

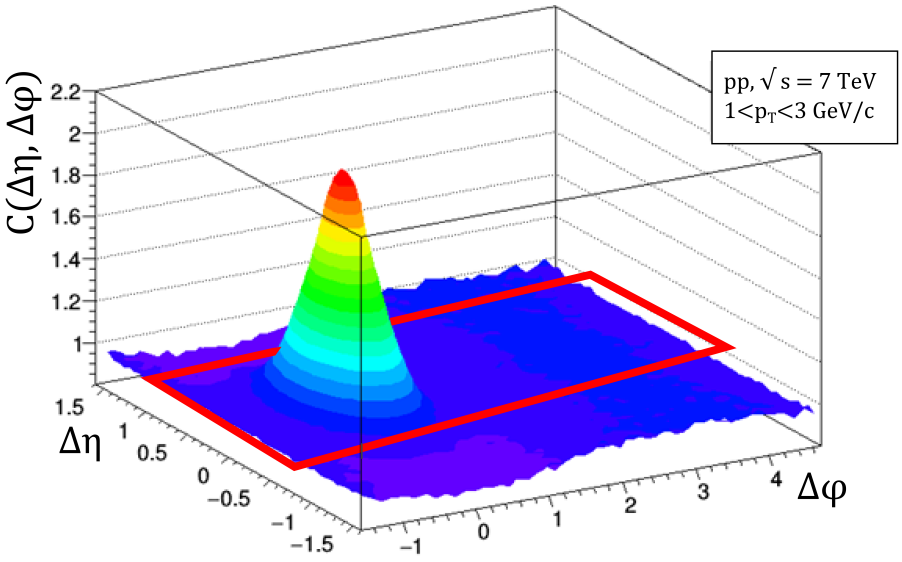

Figure 3.10: Resonance contribution to the correlation function $C(\Delta\eta, \Delta\varphi)$ (marked in red).

of the electrons are formed by photon conversion, the photon would have had a much higher energy than the electron. This means that the electron and positron formed in this way would tend to go in the same direction. Therefore photon conversions add another contribution to the near-side jet peak structure in the correlation function.

Gluon strings

When two protons collide at sufficiently high energies the partons of the two protons may interact with one another. If this happens with two gluons, they will be attracted to one another due to the gluon self interaction causing a narrow area of strong colour field lines to form between the gluons which can be referred to as a gluon string. This string can stretch, increasing the energy in the colour field, until it breaks, resulting in the production of new quarks which then hadronize, forming particles that fly out. The particles produced in this way will be correlated along the direction of the string or in our case along the direction of the beam axis. These particles will have a similar η with no correlation in their φ causing them to contribute to the longitudinal ridge in addition to resonances located at $\Delta\eta = 0$ spreading over the entire range in $\Delta\varphi$.

Coulomb interactions

The Coulomb interaction causes a force between electrically charged particles. Particles with the same electric charge repel each other and particles with opposite electric charges attract each other. This force has an infinite range and is stronger the smaller the distance between the particles is. Therefore, it mainly influences the particles inside the near-side peak. For particles with the same charge it will tend to lower and broaden the peak and for particles of opposite charge it will tend to narrow and increase the height of the peak. In total, this contribution slightly changes the shape of the near-side peak.

Flow

Flow describes the collective effects of particles produced in relativistic heavy-ion collisions. It describes how the energy, momentum and number of particles varies with direction. Elliptic flow gives a measure to which extent the flow is not uniform in the transverse plane. It is thought to be a consequence of the production of quark-gluon plasma and therefore is not expected to be present in pp collisions.

Ridge

The Ridge, sometimes also called the near-side ridge, is a correlation structure around $\Delta\varphi = 0$ extending across a broad range in $\Delta\eta$. The origin of the Ridge is still under theoretical debate. It is usually attributed to interactions between the QGP medium and jets, as well as initial state density fluctuations and the development of collective motion in the QGP phase [35]. While QGP is widely believed not to form in pp collisions, the Ridge has surprisingly been observed in these collisions. A detailed explanation of the Ridge is given in the next section.

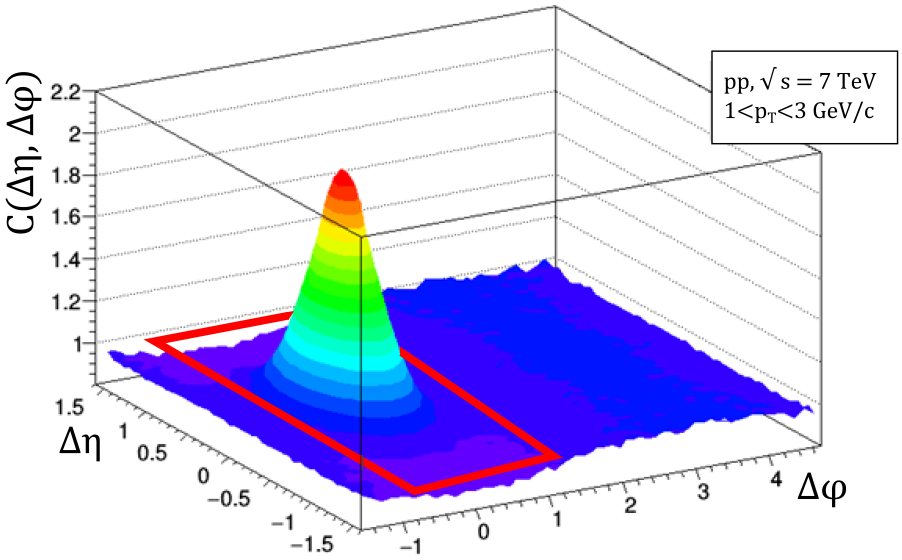

Figure 3.11: The contribution of the Ridge to the correlation function $C(\Delta\eta, \Delta\varphi)$ (marked in red).

3.4 The Ridge

The Ridge, also called the near-side ridge or the long-range correlation, is characterized by an excess of particles separated by a small azimuthal angle $\Delta\phi \approx 0$ without any specific separation in pseudorapidity. This manifests in the correlation function as a ridge-like structure of more or less constant height, centred around $\Delta\phi = 0$ and extending over a broad range in $\Delta\eta$. The Ridge was initially observed by the STAR collaboration at RHIC in gold ion collisions at a centre of mass energy per nucleon of $\sqrt{s_{NN}} = 200$ GeV [36]. This structure was first observed using high momentum trigger particles ($p_T > 4$ GeV/c), however, it was later expanded to include include trigger and associated particles in an intermediate range and even using untriggered particles [37, 38]. Both STAR and PHOBOS observed the Ridge extending the full range of their respective detectors corresponding to several units in $\Delta\eta$. It was also confirmed by experiments at the LHC in Pb-Pb collisions. In figure 3.12 a prominent ridge-like structure is visible in the untriggered correlation function measured at STAR.

The Ridge in heavy-ion collisions is most commonly attributed to correlations within QGP. The most common explanations involve some hydrodynamic flow, which describes

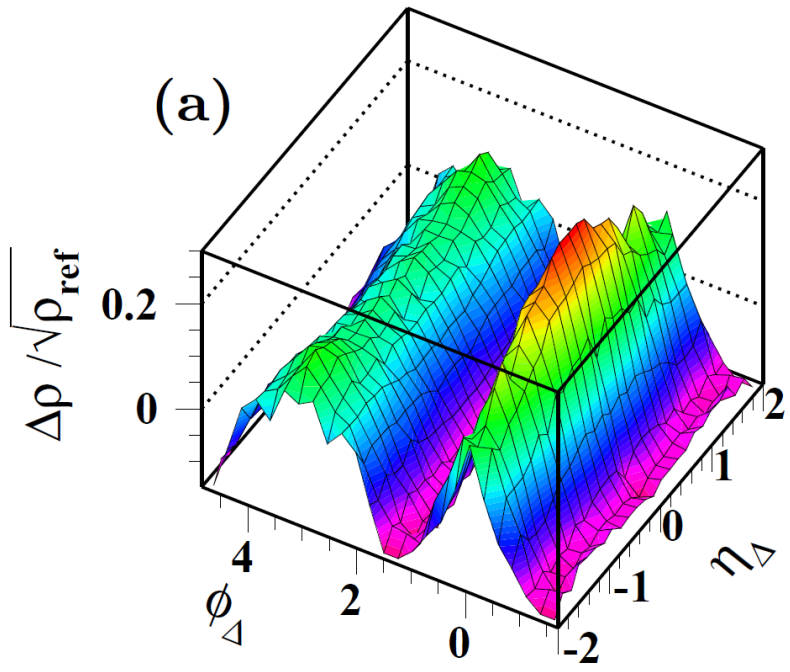

Figure 3.12: The correlation function measured in the top 5% of central Au-Au collisions at $\sqrt{s_{NN}} = 200$ GeV by STAR [39].

the evolution of QGP once it has formed [40, 41]. While some models only include flow itself as the mechanism, others include interactions of the QGP medium with jets. A typical example of such an explanation goes as follows: the excess particles forming the Ridge are produced by jets that are quenched in the QGP medium. This quenching produces excess particles along the beam by QCD bremsstrahlung, causing a wide pseudorapidity distribution. These particles are then boosted out by the transverse flow of the medium in similar azimuthal angles [40, 42]. Other models include correlations in the Glasma, which is a type of non-equilibrium matter that theoretically forms as a precursor to QGP [43]. In all of the cases, the angular collimation in the azimuthal angle is credited to the transverse flow of the QGP medium. Hence, the presence of the Ridge could theoretically be used as an indicator for the formation of the QGP, in contrast to other methods which compared phenomena in heavy-ion collisions to those from smaller systems (mainly pp but also p-A). Smaller systems are used as a comparison since they are too small for QGP to form and there is not enough time for thermalization to occur so all the particles are produced in hard processes.

It was therefore a great surprise when the CMS collaboration announced the discovery of a long range rapidity correlation corresponding to the Ridge in pp collisions. It was

discovered in a high multiplicity subset of pp collisions at $\sqrt{s} = 7$ TeV [44]. This discovery is often touted as not only the first discovery of the LHC but also as one of the only truly unexpected results of the LHC [45]. It was also subsequently observed in proton-ion collisions at the LHC. Further measurements of the Ridge in pp collisions at both $\sqrt{s} = 7$ TeV and $\sqrt{s} = 13$ TeV by the CMS collaboration in 2016 clarified certain aspects of the Ridge shown in figure 3.13[46]. This includes a steady linear increase in the yield of the Ridge structure with increasing event multiplicity (right panel of figure 3.13) and a measurement indicating that the Ridge is dominantly present for trigger and associated particles in the $1.0 < p_T < 3.0$ GeV/c range (left panel of figure 3.13).

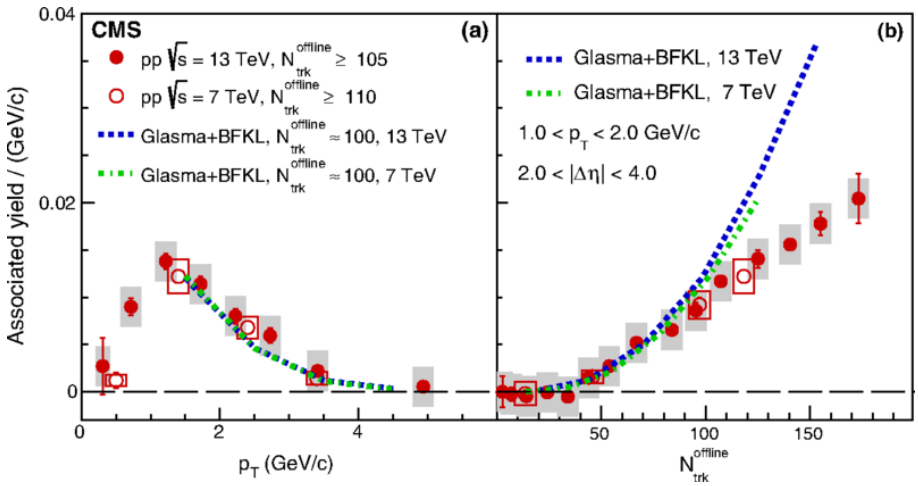

Figure 3.13: The associated yield (i.e. integral over the phase space participating in the Ridge $2 < |\Delta\eta| < 4$) as a function of p_T (left panel) and multiplicity (right panel) [46]

As already mentioned, based on our current understanding of pp collisions, no QGP is formed, which could lead us to three possible interpretations of this data. The first possibility is that the Ridge, even in heavy-ion collisions, is not formed in the ways previously thought, but is a remnant of the initial state. Alternatively, the Ridge could be produced in heavy-ion collisions through hydrodynamic flow as originally postulated, but is caused by new different physics of the initial state in the collisions of smaller systems.

Both of these possibilities would severely constrain our current models. Currently the frontrunner is the colour glass condensate model (CGC) [47]. The CGC is a type of matter thought to exist in the classical field theory approximation of QCD in very dense parton systems. Such high densities can be achieved in the lab system by the length contraction of a high energy hadron or nucleus, flattening them along the direction of motion, greatly decreasing the particle's volume but keeping the number of partons the

same. In such situations the gluons in the flat particle "pancake" appear almost stationary because of time dilation in addition to their greatly increased density, hence the name: Coulor - referring to the charge in quarks and gluons; Glass - referring to materials that are disordered and act like solids on short time scales but more of a liquid on longer time scales; and Condensate - referring to the drastic increase in density compared to the normal state. The CGC is an intrinsic property of the particles and can only be observed during high energy collisions. In these collisions two such sources of CGC collide and interact creating strong colour fields between them that, in theory, would coalesce, forming correlated particles and manifest as the Ridge. The CGC model has been used to some success in describing features seen in lepton-proton collisions at HERA (geometric scaling) and in the modeling of the initial conditions in heavy ion physics [48]. If it is the case that initial state effects and saturation physics are the answer to the Ridge in smaller systems, a new state of matter would have been discovered opening new fields of research for both experimental and theoretical physicists.

Finally, some physicists have proposed that, similarly to what we see in heavy-ion collisions, this Ridge may actually be formed by the collective motion of particles in pp collisions, which would imply that QGP is formed in these collisions. If this would be confirmed it would constitute a great discovery. While hydrodynamics is a successful framework to describe long range correlations in the macroscopic hot matter (QGP) created in heavy ion collisions, it was not supposed to be applicable in small systems like pp collisions. This is because these small systems produce only a few particles per unit of pseudorapidity and the QGP source would be tiny (on the order of 1 fm^3) and extremely short lived, meaning it would have not enough time to thermalize. Additional evidence for the hydrodynamic model came with the first proton-nucleus measurements at CERN (p-Pb at $\sqrt{s_{NN}} = 5\,\text{TeV}$ [49]). The strength of the Ridge correlation in p-Pb turned out significantly stronger than in pp at the same multiplicity. Other factors supporting this hypothesis include the fact that strength of the correlation is almost the same when observing four particle correlations as it is with two, which would be the case if the particles had a collective origin. Additionally, the dependence of the correlation strength on particle mass was exactly what was expected from hydrodynamic flow. All of the characteristics of the p-Pb Ridge are in good agreement with the theory that the correlation is caused by hydrodynamic flow. Even hydrodynamic models that assume that

the system behaves like a macroscopic ideal fluid with reasonable initial conditions for the size ($\sim$ 1 fm) and lifetime ($\sim$ 1 fm/c) of the fluid give the correct order of magnitude for the values of the strength of the correlation signal and its multiplicity dependence. These models also give accurate predictions for matter created in Pb-Pb collisions, just taking into account the original drop of fluid to be on the order of 5000 times larger by volume. Despite this considerable evidence, the question remains how such a tiny system could have the time to thermalize practically instantly forming a drop of QGP.

One possible explanation could be that at sufficiently high energies, collisions of a proton would qualitatively behave like that of a small nucleus in that it is made up of a sea of partons which can simultaneously undergo independent scatterings. The final state particle density in certain pp collisions can even be larger than that of central heavy ion collisions since they are generally accelerated to higher energies per nucleon. Theoretical studies have shown that the time scale for the thermalization of QGP matter could be less than 1 fmc^{-1} meaning that the volume required for thermalization could indeed be on the order of 1 fm^3 [50]. Since the density in these collisions would be high, the mean free path of particles in the medium would be very small, much smaller than the system dimensions. Hydrodynamic models are not sensitive to the absolute size of the medium but depend on ratios (such as *mean free path/system size*) meaning that this could indeed be happening in high energy pp collisions. If QGP is indeed being created in these smaller systems, a plethora of new measurements can be made revealing additional information on correlation lengths, finite size effects and relaxation time scales.

Whatever the case may be, the discovery of the Ridge in these smaller systems has profound implications for high energy physics.

Chapter 4

Experimental Setup

This chapter will discuss the LHC (Large Hadron Collider) and ALICE (A Large Ion Collider Experiment) which are respectively the particle accelerator/collider and the detector used to create and measure the data used in this thesis.

4.1 The Large Hadron Collider

The LHC is currently the largest functioning machine in the world. It was built by and is run by the European Organization for Nuclear Research (CERN) which was established in 1954 as a European joint venture and now has 23 member states. CERN operates the largest particle physics laboratory in the world where the fundamental structure and properties of the universe are studied. Providing state of the art infrastructure needed for high-energy physics research is CERNs main function, resulting in many important achievements made through experiments at CERN. These achievements include many important discoveries as well as the development of many new technologies resulting in several Nobel prizes for physics. Examples of such discoveries include the discovery of the W and Z bosons in the early 1980s, the discovery of direct CP violation in 1999 and most recently the discovery of a Higgs-like boson with a mass of around 125 GeV/c^2. Technologies developed at CERN have countless applications in society including a plethora of uses in the medical and aerospace industries as well as the development of the World Wide Web.

4.1.1 The LHC accelerator complex

Currently the main accelerator complex at CERN consists of a network of six accelerators and one decelerator. The accelerators form a chain with each one increasing the energy of a particle beam before delivering it to certain experiments or the next more powerful accelerator. The complex is optimised for accelerating both protons and lead ions. Protons are obtained by stripping hydrogen atoms of their electrons using an electric field. They are then accelerated to 50 MeV using Linac 2, which is a linear accelerator, before being injected into the Proton Synchrotron Booster (PSB), which accelerates them to 1.4 GeV. The PSB is followed by the Proton Synchrotron (PS) and Super Proton Synchrotron (SPS), where they are accelerated to 25 GeV and 450 GeV respectively, before being finally transferred to the LHC. Lead ions follow a similar route to protons, however, they start being accelerated in Linac 3 followed by the Low Energy Ion Ring (LEIR) before being transfered to the PS.

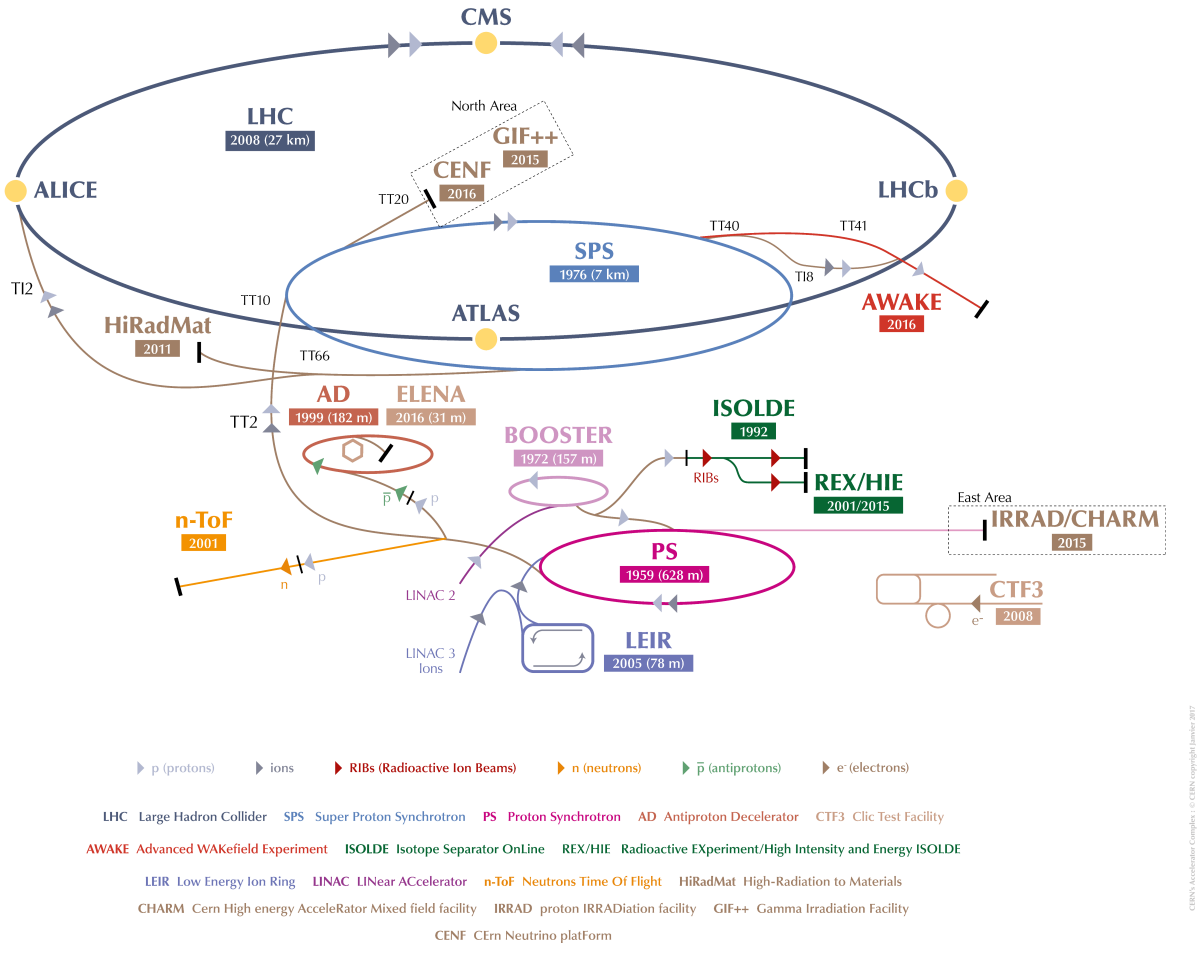

Figure 4.1: The accelerator complex at CERN leading up to and including the LHC [51].

The LHC is a synchrotron type particle accelerator designed to accelerate protons to energies up to 7 TeV and lead ions up to 2.76 TeV per nucleon [52]. Two beams of particles are accelerated in opposite directions in separate beam pipes leading to collisions at center of mass energy of 14 TeV for protons and 5.52 TeV per nucleon for lead ions, making the LHC the most powerful particle collider in the world. When in operation, the LHC accelerator and detectors draw about 120 MW of power. Approved by CERN in 1994, the LHC was constructed between 1998 and 2008 in the same tunnel used by the CERN Large Electron-Positron (LEP) collider. The tunnel is 27 km in circumference and lies up to 175 m underground beneath the Frace-Switzerland border near Geneva. The LHC started colliding particles in late 2009 and its first official research run took place from March 2010 to February 2013, when it collided protons at energies of 3.5 to 4.0 TeV ($\sqrt{s}$ = 7 to 8 TeV), which was about four times the previous record set by Fermilab [53]. In 2013 the LHC was taken offline and upgraded until it was restarted in early 2015 for its second research run reaching energies of 6.5 TeV per proton beam ($\sqrt{s}$ = 13 TeV).

4.1.2 Radiofrequency Cavities

The charged particles of the LHC are accelerated using 16 radiofrequency (RF) cavities, which are metallic chambers that contain an electric field. The two evacuated LHC beam pipes each pass through two sets of four RF cavities where the entirety of the acceleration takes place. The rest of the LHC ring serves to turn the particles back to RF cavities for further acceleration as well as focus the beams and cross them at collision points. The electric fields are generated by klystrons with a waveguide directing the energy into the cavities. The shape of the cavities is such that their resonant frequency corresponds to that of the periodic electric field generated by the klystrons. Thus, the intensity of the electromagnetic waves in the cavities will build up creating a maximum potential difference of 2 MV per cavity or a total of 16 MV per beam. Over a period of about 20 minutes the particles pass through the RF cavities over 10^7 times increasing their energy more than 14 fold, 0.5 MeV per turn, from 0.45 TeV to 6.5 TeV. Due to the oscillating nature of the field inside the cavities, there exists a sweet spot in the arrival time and speed of the particles passing through the cavity where no acceleration is felt. Particles in this spot will maintain their current speed. Particles which arrive slightly too early will feel a backwards force depending on how early they arrive, which will slow them down pushing

them towards the sweet spot. On the other hand, particles that arrive slightly too late will feel a forward force accelerate them towards the sweet spot. A consequence of this method of acceleration is that the particles in the beams are not continuous but are grouped into packs called "bunches" in which the particles oscillate forwards and backwards. The electric field in the cavities oscillates at a frequency of 400 MHz causing subsequent RF "buckets", where bunches of particles could potentially be placed, to be separated by 2.5 ns in time. However the LHC is designed for only every tenth bucket to be filled with particles corresponding to a bunch spacing of 25 ns in time and 7.5 m in space, or an effective freuency of 40 MHz. At 7 TeV each bunch has a RMS length of 7.6 cm and a RMS spread in energy of 0.011%.

4.1.3 LHC magnets

The beams are kept on their circular path using superconducting dipole magnets. Each of these magnets is 15 meters long and consists of two coils of copper-clad niobium-titanium wire cooled using superfluid helium-4 to their operating temperature of 1.9 K. The coils are positioned in such a way that their magnetic field is constant and vertical, perpendicular both to the radius of curvature of the LHC ring and to the velocity of the particles. This causes all of the charged particles in the beams to experience the same Lorentz force, acting towards the centre of curvature of the LHC ring acting as a centripetal force maintaining the circular path of the particles. A total of 1232 of these dipole magnets are installed spanning a combined length of over 18 km making them one of the largest components of the LHC.

Due to the fact that all of the particles in the bunches are positively charged (be they protons or ions), they repel each other causing the bunches to spread out. This problem is exacerbated by imperfections in the magnetic field at the edges of the LHC magnets causing further spreading. Spreading of the bunches along the direction of the beam is not a problem since it is corrected automatically during the natural functioning of the resonant cavities. On the other hand, spreading in the transverse direction is a problem since it will firstly cause the probability of collision of two bunches to decrease and will eventually cause the particles to collide with the walls of the beam pipe knocking them out of the beam. Several other factors can also cause the quality of the beam to deteriorate even if it were not charged. For example, the particles can "fall" due to gravity. Even

neutral massless particles would diverge over time if their injection parameters such as angle or position were to differ ever so slightly. Two particles injected at an angle difference of only 10^{-6} rad would separate by more than 1 m after only 5 ms. Therefore there is a need for focusing the beams which is done by quadrupole magnets. While the dipole magnets have a constant magnetic field pushing each charged particle by same amount, the quadrupole magnets have a linearly increasing magnetic field. The field is zero in the centre and increases positively on one side and negatively on the other. Particles moving along the centre of the beam pipe will feel no force while passing through the quadrupoles while particles to the right of the centre will feel a force to the left and vice versa. Since the magnetic field increases as the distance from the centre increases, particles that are further from the centre will feel a larger force and will be turned by a greater angle to the centre. Additionally, since the increase of the field is linear, the quadrupole will act as a convergent optical lens with a focal point, directing all parallel particles towards that point. This focusing, however, only works along one axis. Due to the nature of the quadrupole magnet, the field is such that the perpendicular axis acts as a divergent lens, defocusing the particles. To focus a beam of particles along both axes, a succession of at least 2 perpendicular quadrupole magnets is needed, one focusing and the other defocusing the beam along each axis. A combination like this allows for an equal net focusing along both axes with the focal lengths given by $F = (\frac{1}{f_1} + \frac{1}{f_2} - \frac{d}{f_1 f_2})^{-1} = \frac{f^2}{d}$ since the focal lengths for focusing and defocusing are the same $f_1 = -f_2 \equiv f$ with d being the distance between the two quadrupoles. There is a total of 858 quadrupole magnets at the LHC.

Higher moment magnets, such as sextupole, octupole and decapole correctors are also used to correct imperfections in the magnetic field at the ends of the dipole and quadrupole magnets. Without these, the particle trajectories would become unstable after only a few minutes or the order of 10^6 turns. A total of around ten thousand superconducting magnets are used at the LHC requiring almost 100 tonnes of superfluid ^{4}He.

The magnets of the LHC are organised into cells in which the individual magnets are arranged in what is called a FODO pattern. F stands for a quadrupole that focuses vertically and defocuses horizontally, D defocuses vertically and focuses horizontally and O is a space or a set of deflector magnets (dipole). On the ends of each of the quadrupoles and dipoles are smaller corrector magnets of higher order. The basic multipolar magnetic cell (FODO) is 110 m long and consists of two perpendicular quadrupoles, six dipoles and

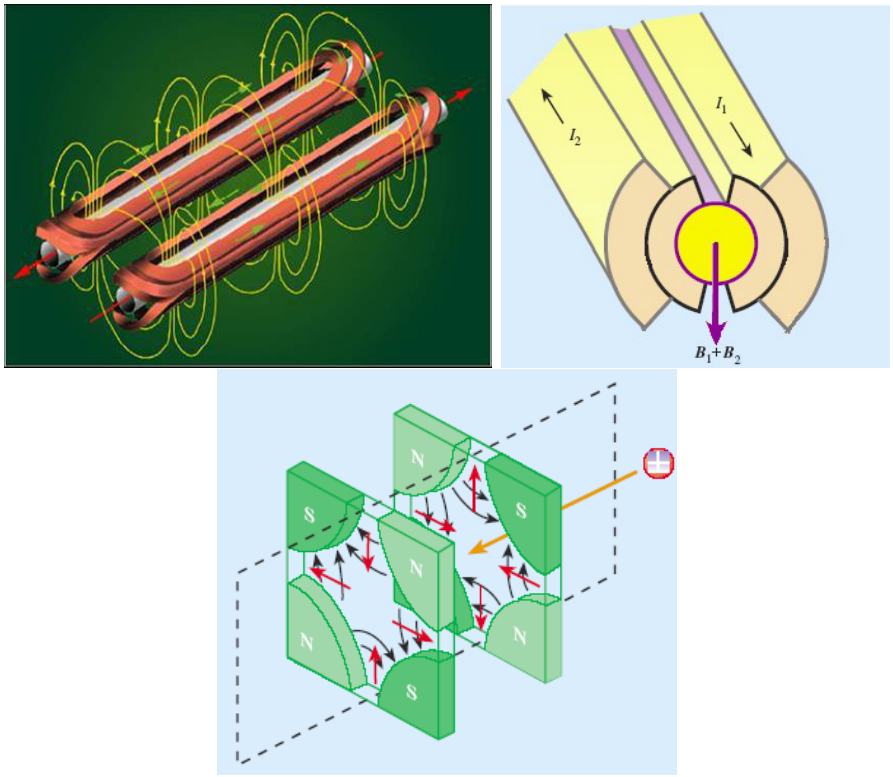

Figure 4.2: Magnetic field of the dipoles for turning the beam (top two images) and quadrupoles for focusing the beam (bottom image) of the LHC [54].

many of the smaller corrector magnets.

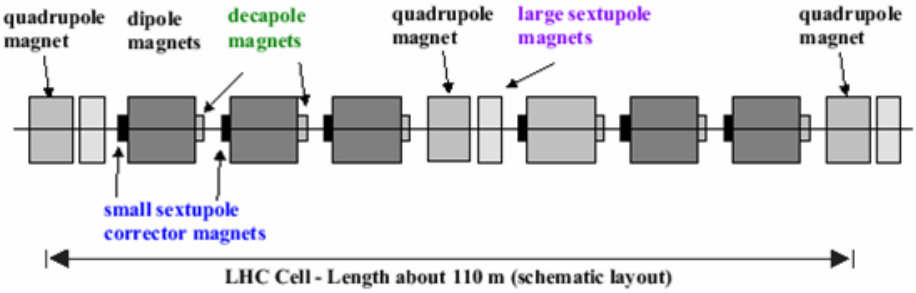

Figure 4.3: The FODO structure of one cell [54].

The two antiparallel beam pipes cross at four locations where the particle collisions take place. At these crossings there are an additional eight sets of magnets called “inner triplets”, one set per beam per crossing. These magnets focus the beams into the four areas where the collisions will take place. They reduce the size of the bunches from 0.2 mm to 16 μm at the interaction points. This reduction is important since the luminosity is inversely proportional to the product of the two beam dimensions at the interaction point. Reducing this increases the luminosity and thus increases the number of new

particles produced in collisions per unit of time. This is because the number of "new particles" produced per unit of time is directly proportional to the luminosity as well as the differential cross section of the particles being collided $\frac{N}{\Delta T} = L[cm^{-2}s^{-1}] \cdot \sigma[cm^2]$. In addition to being inversely proportional to the product of the two beam dimensions $\sigma_x \cdot \sigma_y = (16\ \mu\text{m})^2$, luminosity is also proportional to the number of protons per bunch in each ring $N_1 = N_2 = N$, the revolution frequency f and the number of bunches per beam n_b:

$$L = \frac{N^2 \cdot f \cdot n_b}{4 \cdot \pi \cdot \sigma_x \cdot \sigma_y}. \tag{4.1.1}$$

The original design of the LHC was for there to be about 10^{11} protons per bunch, 2808 bunches and a revolution frequency of 11246 Hz, determined by the speed of the particles and the length of the beam pipes. This gives a luminosity of about $10^{34}\text{cm}^{-2}\text{s}^{-1}$ which handily beats the luminosity of the LEP and Tevatron achieveing luminosities of the order of $10^{31} - 4 \cdot 10^{32}\text{cm}^{-2}\text{s}^{-1}$.

4.1.4 LHC experiments

Large experiments are placed at each of the four locations where the particle collisions take place. There are four large detectors, each placed at their own intersection point, and three much smaller detectors which share an intersection point with one of the larger detectors. The two largest detectors are the ATLAS experiment (A Toroidal LHC AparatuS) [55] and the CMS experiment (Compact Muon Solenoid) [56]. These two are general-purpose particle detectors and are mainly concerned with proton collisions. They are the two experiments involved in the discovery of the Higgs boson in July 2012. The other two large detector experiments are ALICE (A Large Ion Collider Experiment) [57] and LHCb (LHC beauty) [58]. ALICE is the detector used in this work and will be discussed in detail in the next section. LHCb is a specialized b-physics experiment, designed to measure CP violation parameters in b-hadron interactions, which could lead to a better understanding of the matter-antimatter asymmetry in the Universe. The three small experiments are the TOTEM experiment (TOTal Elastic and diffractive cross section Measurement), the MoEDAL experiment (Monopole and Exotics Detector at the LHC) and the LHCf experiment (Large Hadron Collider forward). TOTEM shares an

interaction point with CMS and aims to measure total cross sections, elastic scatterings and diffractive processes. MoEDAL shares an interaction point with LHCb and its aim is to search for the magnetic monopole or other highly ionizing stable/pseudo-stable massive particles. LHCf shares an interaction point with ATLAS and is designed to study particles generated in the forward region of collisions.

4.2 The ALICE experiment

ALICE (A Large Ion Collider Experiment) is the name of one of the largest physics collaborations in the world as well as the name of the large detector array that they use and maintain at the LHC. The collaboration consists of over 1800 members coming from 177 institutes in 41 countries. The main goal of the ALICE collaboration is to be the dedicated heavy-ion programme of the LHC, focusing its studies on QGP [59]. The collaboration was originally formed to find QGP however by the time the LHC and ALICE started taking data, it was determined by the heavy-ion community that QGP had already been created and discovered at RHIC. This did not change ALICE's main goals much, simply adding an emphasis on studying the characteristics and physical properties of QGP as well as exploring the phase diagram of strongly-interacting matter to try and find the location and the nature of the phase transitions between QGP and regular hadronic matter. In addition to QGP physics, ALICE also studies other phenomena in heavy ion collisions as well as in smaller systems such as proton-nucleus (p-A) and proton-proton (pp) collisions, which is important since the LHC is only colliding protons the majority of the time. These smaller systems are often used, along with ultra-peripheral heavy-ion collisions, as a reference to which central heavy ion collisions can be compared. However, they also exhibit their own set of interesting physics phenomena and are thoroughly studied as well. The ALICE detector can also be used to study cosmic rays.

The detector itself is located at the second interaction point of the LHC (called Point 2) in the cavern where the LEP L3 experiment used to be and even inherited its main magnet. The detector consists of two major parts, the central barrel and the muon spectrometer (muon arm). The central barrel is centred around the nominal interaction point which is also the origin of the global ALICE coordinate system, with the muon arm being off to the side. The global ALICE coordinate system is a right-handed cartesian system where the z

axis follows along the beam direction, the x axis is horizontal, pointing towards the centre of the LHC ring and the y axis points vertically upwards. These cartesian coordinates are not the most practical coordinates for the collisions and physical processes studied and so they can be converted to more useful ones like φ and η discussed in the previous chapter.

The central barrel part of the ALICE detector can be used for the detection and identification of hadrons, electrons and photons in the mid-rapidity region ($|y| < 0.9$) and the muon arm part is placed on the negative z side of the central barrel covering a pseudorapidity range of $-4.0 \leq \eta \leq -2.5$. Both parts of the ALICE detector cover the full azimuthal range. An overview of the ALICE detector layout can be seen in fig 4.4.

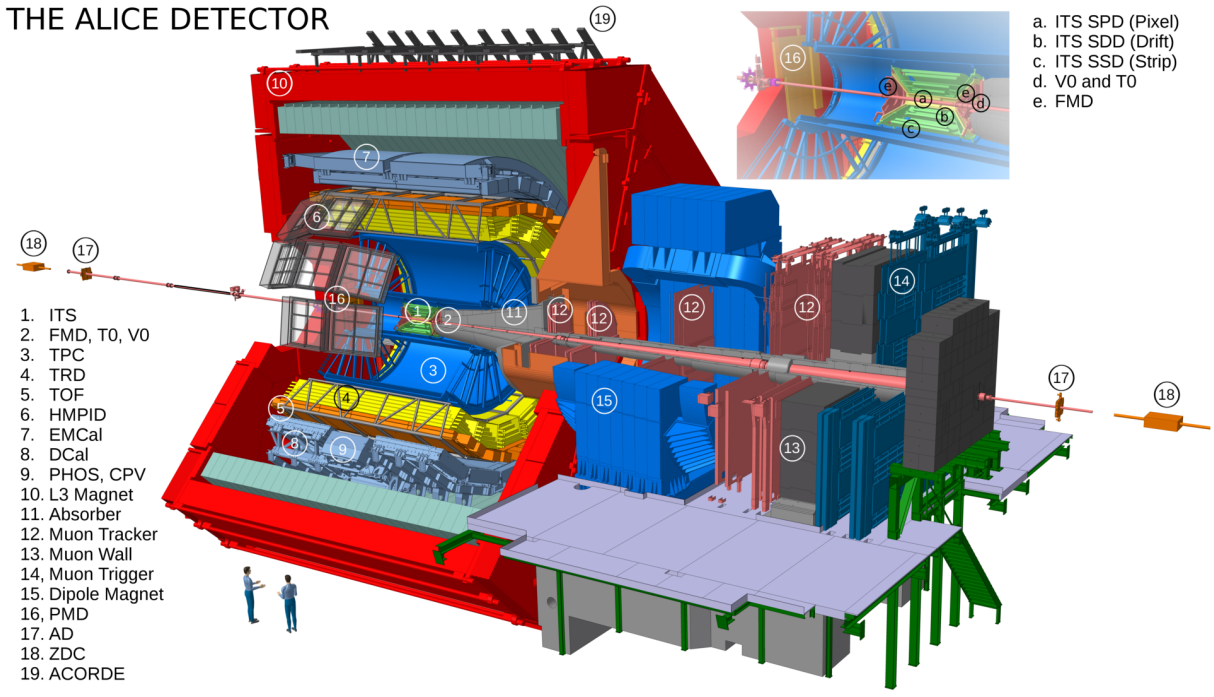

Figure 4.4: Setup of the ALICE detector during RUN 2 [60].

4.2.1 ALICE sub-detectors

A short description of the ALICE sub-detectors is given below with detectors involved in this analysis being described in more detail in the following section.

- Inner Tracking System (ITS) [61]: The ITS is the detector closest to the beam line. It consists of a total of 6 layers of semiconductor silicon detectors. Its main purpose is tracking and vertexing, determining the position of the primary vertex

from the collision, the position of any secondary vertices for strange, charm and beauty reconstruction as well as giving information on the pathing of the particles. It can also be used for particle identification and can improve momentum and angle measurements of other detectors. More information about the ITS can be found in the next section.

- Time Projection Chamber (TPC) [62]: The TPC is the main tracking detector of the ALICE central barrel and is one of the most important detectors of the ALICE experiment as a whole. It is a gaseous detector used for finding tracks of charged particles, measuring particle momenta and plays a role in particle identification. More information about the TPC can be found in the next section.

- Transition Radiation Detector (TRD) [63]: The TRD detector serves to differentiate different types of charged particles at high momenta which can be problematic for other detectors. For example, the TPC starts having problems differentiating electrons and pions for momenta above 3 GeV/c when pions enter the relativistic rise of the Bethe formula. The TRD differentiates particles by means of transition radiation (TR) which is emitted in the x-ray spectrum when a charged particle passes a boundary between two materials with different dielectric constants. The amount of TR produced is different for different particles. To increase the amount of TR produced the TRD uses a radiator containing a foam-like substance causing particles to pass over many such boundaries increasing the probability of TR emission. The rest of the TRD functions similarly to the TPC, being a gaseous detector with a drift region and an amplification region, the difference being the amount of TR deposited into the drift region for different particles. The TRD is located around the TPC detector at a radius of 2.9 m to 3.7 m from the beam pipe. It is segmented in the azimuthal direction into 18 supermodules, each consisting of 5 stacks in the η direction from $-0.9 < \eta < 0.9$ and 6 radial layers, accounting for 540 chambers. Each chamber has over 2000 readout pads meaning that the TRD can contribute to track reconstruction. The TRD can also serve as a fast trigger for charged particles with an online tracking and PID time of less than $8\mu s$ after the primary interaction. The ability of the TRD to differentiate electrons and pions can be seen in figure 4.5.

- Time Of Flight (TOF) [65]: The main function of the TOF detector is to provide

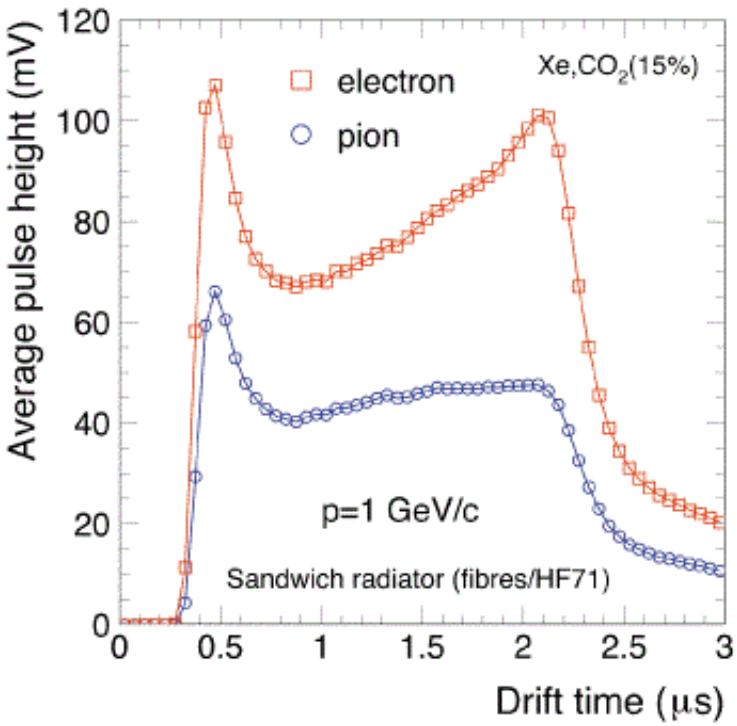

Figure 4.5: Response of the TRD detector for electrons and pions [64].

particle identification in conjunction with other detectors, especially at intermediate momenta ($p_T < 5$ GeV/c). It precisely measures the time between the collision and the arrival of the particles in the TOF which is used to determine the particle's speed. It is located just outside the TRD detector at 3.7 m from the beam line. More information about the TOF can be found in the next section.

- High-Momentum Particle Identification Detector (HMPID) [66]: The HMPID is a ring-imaging Cherenkov (RICH) detector with a caesium iodide photocathode and an active area of 11 m^2. It is used for identifying hadrons that have a higher momentum range than what the TPC and TOF are able to discern. For pion-kaon discrimination it has a momentum range of up to 3 GeV/c and for kaon-proton discrimination a momentum range of up to 5 GeV/c. The HMPID particle identification performance can be seen in figure 4.6.

- Electromagnetic Calorimeter (EMCal) [68]: The EMCal is a lead-scintillator sampling calorimeter. Lead is used as a high density and high Z material to trigger showering of incident electromagnetically interacting particles. Polystyrene with certain additives (fluorescent emitter and wavelength shifter) is used as the scin-

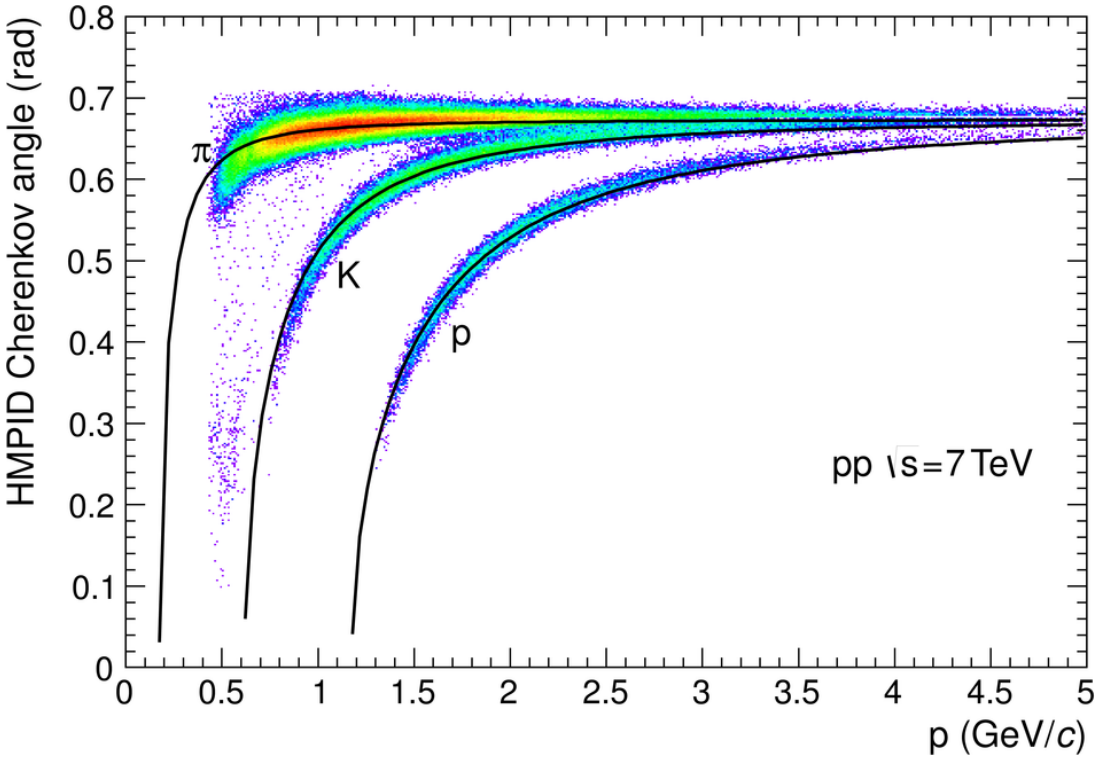

Figure 4.6: HMPID particle identification performance [67].

tillator, as it is easy to manufacture and has a bonus of being cheap. In contrast to gaseous detectors like the TPC, which have a larger relative error on the momentum measurement with increasing momentum ($\frac{\sigma_p}{p} \sim p$), the relative error on the energy measurement of the EMCal decreases with increasing energy ($\frac{\sigma_E}{E} \sim \frac{1}{\sqrt{E}}$). The particles lose some of their energy in the EMCal converting it into proportional amount of detectable light. Charged particles mainly lose their energy by means of bremsstrahlung and high-energy photons lose their energy by e^+e^- pair creation. The EMCal is the outmost detector before the L3 magnet and has a thickness of 24 cm (about 20 radiation lengths) weighing in at a total of about 100 tonnes. It covers an azimuthal angle of 110 degrees and a pseudorapidity range of $|\eta| < 0.7$. It enables the full reconstruction of high energy jets, allowing ALICE to study certain hard processes and improves measurements of high energy photons and electrons.

- Photon Spectrometer (PHOS) [69]: PHOS is a high resolution electromagnetic calorimeter specialized for photon identification capable of detecting photons in the 0.5 to 10 GeV/c range. It can also provide identification of neutral mesons through the two-photon decay channel. It is made up of fast scintillating lead tungstate

($PbWO_4$) crystals with a set of multi-wire proportional chambers placed in front of them for charged particle rejection and is located at the bottom of the ALICE central barrel.

- The L3 Magnet: While not a detector in and of itself, the magnet is key to functioning of many of the other detectors. The detectors of the central barrel are housed in the octagonal magnet which provides a magnetic field of up to 0.5 T, bending the trajectories of charged particles. From the direction of bending the sign of the charge can be determined and from the radius of curvature $\frac{p}{q}$ can be determined for each particle. It is one of the largest non-super-conducting magnets in the world that was inherited from the LEP L3 experiment and was only slightly modified by adding octagonal end caps to improve the uniformity of the magnetic field.

- Forward Multiplicity Detector (FMD) [70]: The FMD provides measurements of the charged particle multiplicity in the forward regions (small angles relative to the beam, $-3.4 \leq \eta \leq -1.7$ and $1.7 \leq \eta \leq 5.0$). It also provides information on the inclination of the event planes and can give an independent measurement of v_2. It consists of 5 discs, each with 10240 silicon strip channels placed around the beam pipe covering the full azimuthal angle.

- ALICE Cosmic Ray Detector (ACORDE) [71]: ACORDE consists of an array of 60 plastic scintilator modules placed on top of the upper three faces of the ALICE magnet. It acts as a Level 0 cosmic ray trigger and, together with other ALICE sub-detectors, it provides precise information on cosmic rays with primary energies around 10^{15-17} eV.

- Zero-Degree Calorimeter (ZDC) [72]: The ZDCs are calorimeters which detect the energy (number) of the spectator nucleons in a heavy-ion collision and are thus able to measure the centrality of said collisions. A ZDC is located on either side of the ALICE detector at a distance of 115 m away from the interaction point exactly along the beam line. They consist of a proton calorimeter called ZP and a neutron calorimeter called ZN. The ZDCs are made of a stack of heavy metal plates grooved to allocate a matrix of quartz fibres. The metal plates are made of a tungsten alloy for neutrons and brass for protons.

- T0 Detector [70]: The T0 detector consists of two arrays of Cherenkov counters positioned at opposite sides of the interaction point and placed as close to the beam pipe as possible. The two parts, T0-A and T0-C are located 375 cm and −72.7 cm from the nominal vertex and cover a pseudorapidity range of $4.61 \leq \eta \leq 4.92$ and $-3.28 \leq \eta \leq -2.97$ respectively. Its primary goal is to generate a start time (T0) for the TOF detector. It also serves to measure the vertex position for each interaction and to provide a L0 trigger if the position falls within desirable values, as well as to provide a "wake-up" call for the TRD.

- V0 Detector [70]: The V0 detector consists of two arrays of 32 scintillator counters installed on both sides of the interaction point. The two parts, V0-A and V0-C are located 340 cm and −90 cm from the nominal vertex and cover a pseudorapidity range of $2.8 \leq \eta \leq 5.1$ and $-3.7 \leq \eta \leq -1.7$ respectively. The V0 detector has several functions, mainly serving as an L0 trigger. It provides minimum-bias triggers for the central barrel detectors and also has the ability to provide multiplicity and rough centrality triggers (semicentral vs. central). It contributes to the background rejection of asymmetric events which are caused by the interactions of protons with the residual gas of the vacuum chamber and generate tracks through the other detectors of ALICE.

- MUON Spectrometer [73]: The muon spectrometer is located outside of the central barrel in the pseudorapidity region of $-4.0 \leq \eta \leq -2.5$, corresponding to a polar angle range of $171° - 178°$. It consists of a large muon dipole magnet, a high-granularity tracking system of 10 detection planes, four planes of trigger chambers and three absorbers: a passive front absorber to absorb hadrons and photons from the main interaction point; an inner beam shield to protect the chambers from particles produced at large rapidities and a passive muon-filter wall. The muon spectrometer is used to study the complete spectrum of quarkonia including $\phi, J/\psi, \psi', \Upsilon, \Upsilon'$ and Υ'' via their $\mu^+\mu^-$ decay channel. Measuring all of the quarkonia species simultaneously with the same apparatus allows for a direct comparison of their production rates.

In December 2018, the LHC started its second long shut down which is planned to last until 2021. During this time the performance of the LHC will be upgraded, increasing the luminosity and energy (from 13 TeV to 14 TeV) of the collider among other improvements.

During this time many of the detectors will undergo improvements themselves. Some of the changes will simply serve to repair or exchange damaged or broken components, however, some changes will drastically alter the architecture of the detectors to allow them to cope with the increased performance of the LHC. The detector descriptions in this work represent the state the detectors were in during the first two data taking runs of the LHC during which the data for this work was taken.

4.2.2 The Inner Tracking System

The ITS is the innermost subdetector of ALICE [61], directly surrounding the beam pipe which is made of a 0.8 mm thick beryllium cylinder of 3 cm outer radius. The ITS is centred around the interaction point and ranges from 4 cm to 43.6 cm radially from the beam line and covers a pseudorapidity range of $|\eta| < 0.9$ for all vertices located within ± 5.3 cm from the nominal interaction point along the beam direction. The ITS consists of six coaxial cylindrical layers of silicon detectors. The two inner layers are silicon pixel detectors (SPDs), the two middle layers are silicon drift detectors (SDDs) and the two outer layers are silicon strip detectors (SSDs). Charged particles leave a signal in each of these layers allowing for their trajectory to be reconstructed as they leave the interaction point. The main purpose of the ITS is to track individual particles near the interaction point and thus measure the location of the primary vertex with an accuracy better than 100 μm. The ITS is also used to determine the locations of secondary vertices, which are used for the reconstruction of short-lived charm and strange particles and even some particles containing heavier quarks. Additionally, the ITS is used for PID (particle identification) of low-momentum particles and can improve the momentum and angle measurements of the TPC, especially those which travel along dead zones in the TPC (between TPC sectors).

SPD

The two innermost layers of the ITS are Silicon Pixel Detectors [61]. The layers cover pseudorapidity ranges of $|\eta| < 2$ and $|\eta| < 1.4$ and are located at radii of 3.9 cm and 7.6 cm respectively. The SPD is based on hybrid silicon pixels which are made up of a 2D array of reverse-biased silicon detector diodes directly bonded to readout chips. Each individual silicon cell measures 50 μm ($r\varphi\hat{\varphi}$) by 425 μm ($z\hat{z}$) and is 200 μm thick. The cells are

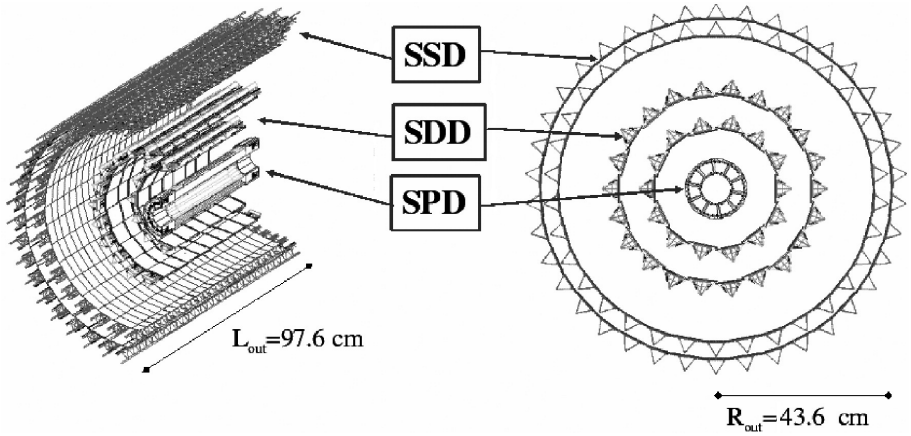

Figure 4.7: An overview of the ITS [74].

Table 4.1
Specifications of the ALICE ITS [61].

Layer	r (cm)	± z (cm)	Resolution (μm)	
			$r\varphi$	z
1 pixel	3.9	14.1	12	100
2 pixel	7.6	14.1	12	100
3 drift	15.0	22.2	35	25
4 drift	23.9	29.7	35	25
5 strip	38.0	43.1	20	830
6 strip	43.0	48.9	20	830

organized into chips containing 256 ($r\varphi\hat{\varphi}$) by 32 ($z\hat{z}$) cells. The minimum threshold of these cells is 1000 electrons and they have an operating clock frequency of 10 MHz.

The SPD's most important role is determining the position of the primary vertex. It is vital for the SPD to be reliable, precise and have a high granularity since it is the detector closest to the interaction point, where an excess of 50 particles/cm^2 are expected to pass for some events. It is also important for the SPD to be radiation hard since it operates closest to the interaction point in a high-radiation environment. It is designed to tolerate an excess of 0.1 MGy of radiation.

In the future, all of the layers of the ITS will be replaced by silicon pixel detectors since they have the best all-round performance.

SDD

The two intermediate layers of the ITS are Silicon Drift Detectors [61]. In addition to the SDD layers having good multitrack capabilities, they have an analog readout so they can provide dE/dx samples needed for the ITS particle identification. The SDDs are produced from a 300 μm thick layer of homogeneous high-resistivity (3 kΩcm) Neutron Transmutation Doped silicon. They have a sensitive area of 70.17 mm ($r\varphi\hat{\varphi}$) by 75.26 mm ($z\hat{z}$) which is split into two drift regions by a central cathode to which a HV bias of -2.4 kV is applied fully depleting the detector volume and generating a drift field parallel to the detector surface. Along the edge of the surface is a row of 256 collection anodes which read out the signal from the SDD. The 2 SDD layers cover the pseudorapidity region of $|\eta| < 0.9$ and are located at distances of 15 cm and 23.9 cm from the beam line, where charged particle density is expected to reach up to 7 particles/cm^2.

SSD

The outermost layers of the ITS are Silicon Strip Detectors [61]. They are vital for the matching of tracks from the ITS to the TPC which is the main tracking detector of ALICE. They also provide dE/dx information for particle identification. The SSD uses 300 μm thick double sided sensors with 768 silicon strips on each side with a 95 μm pitch. The strips are arranged under a stereo angle of 35 mrad and positioned nearly parallel to the magnetic field to reduce ambiguities from high particle densities and to optimize the resolution in the bending direction. The SSD covers a pseudorapidity range of $|\eta| < 0.97$ and is located at distances of 38 cm and 43 cm from the beam line.

The PID capabilities of the ITS are shown in figure 4.8 which plots dE/dx measurements as a function of momentum as measured by the ITS.

4.2.3 The Time Projection Chamber

The TPC is the main tracking detector of the ALICE central barrel and arguably the most important detector for high-multiplicity environments such as heavy-ion collisions, where up to 20000 individual particles can be produced in a single event [62]. Its sensitive volume stretches out radially from 85 cm to 250 cm and 500 cm along the beam direction

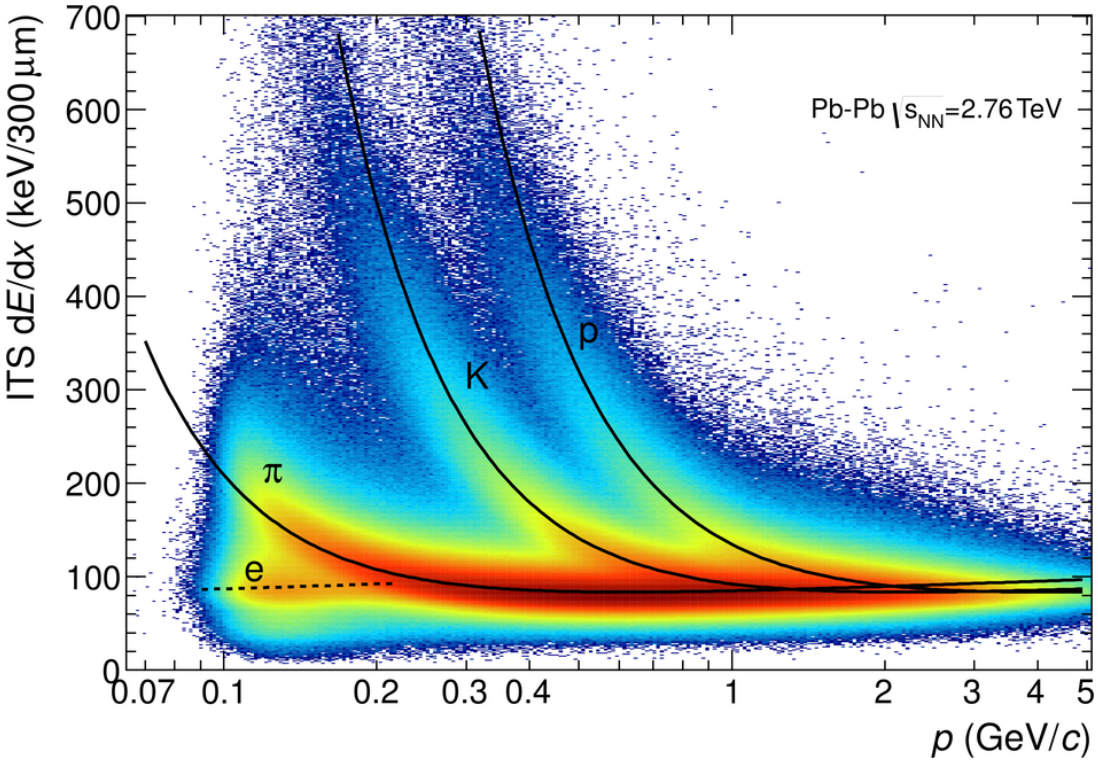

Figure 4.8: Particle identification performance of the ITS [67].

giving it an effective volume of almost 90 m^3. This volume is filled with a Ne-CO_2-N_2 (90:10:5) gas mixture which is the detector's detecting medium. The TPC covers the full azimuthal angle and has a pseudorapidity range of $|\eta| < 0.9$ for full radial length tracks and a higher pseudorapidity range of $|\eta| < 1.5$ for reduced track lengths.

The ALICE TPC is a traditional drift chamber where charged particles ionize the gas along their trajectory. Electrons formed along this track then drift in an electric field to the end plates of the detector where cathodes are situated. The TPC is separated into two parts by the central electrode which is located at $z = 0$ in the middle of the detector. A drift field of 100 kV is applied between the central electrode and the two readout planes located at both sides of the detector ($z = \pm 250$ cm). The readout planes are segmented into more than 570000 pads which register the electron tracks after they have drifted towards them. The tracks are amplified by multi-wire proportional chambers located just before the readout planes where the drifting electrons experience a large enough electric field to cause a cascade and form a measurable signal. The r and φ coordinates of the particle are determined by measuring which pad received the signal, since the drift field is entirely in the z direction, these coordinates are simply translated. The z coordinate of

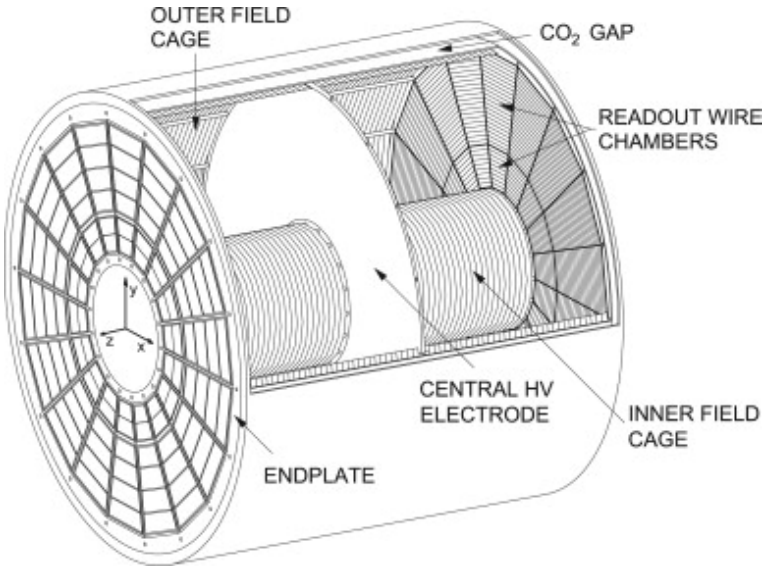

Figure 4.9: The TPC schematic overview [62].

the track is determined by the time taken by the electrons to drift to the end plate. The ALICE TPC has a track position resolution of about 1 mm in both $r\varphi\hat{\varphi}$ and $z\hat{z}$ and can measure particles with transverse momenta in the 200 MeV/c to 100 GeV/c range for the nominal value of the ALICE magnetic field of 0.5 T.

The TPC also uses energy loss per unit path length (dE/dx) measurements in combination with particle momentum measurements for particle identification. For a given particle type, $\langle \mathrm{dE/dx} \rangle$ can be described by the Bethe-Bloch formula $\langle \mathrm{dE/dx} \rangle = \frac{C_1}{\beta^2}(\ln(C_2\beta^2\gamma^2) - \beta^2 + C_3)$ where C_1, C_2 and C_3 are detector parameters, $\beta = \frac{v}{c}$ and γ is the Lorentz factor of the particle. Particles of different mass will have a different dE/dx depending on their momentum. The dE/dx spectrum versus momentum in the TPC for pp collisions at $\sqrt{s} = 7$ TeV is shown in figure 4.10 with the lines being Bethe-Bloch curves for specific particle types.

4.2.4 TOF

The Time Of Flight (TOF) detector measures the time it takes for a particle to reach it enabling a direct measurement the speed of the particle [65]. The time of flight is calculated by taking the initial time of the interaction from the T0 detector and subtracting it from the time detected by the TOF detector. The length of the particle's trajectory is taken from the other detectors (TPC and ITS) and is simply used to calculate the speed. The

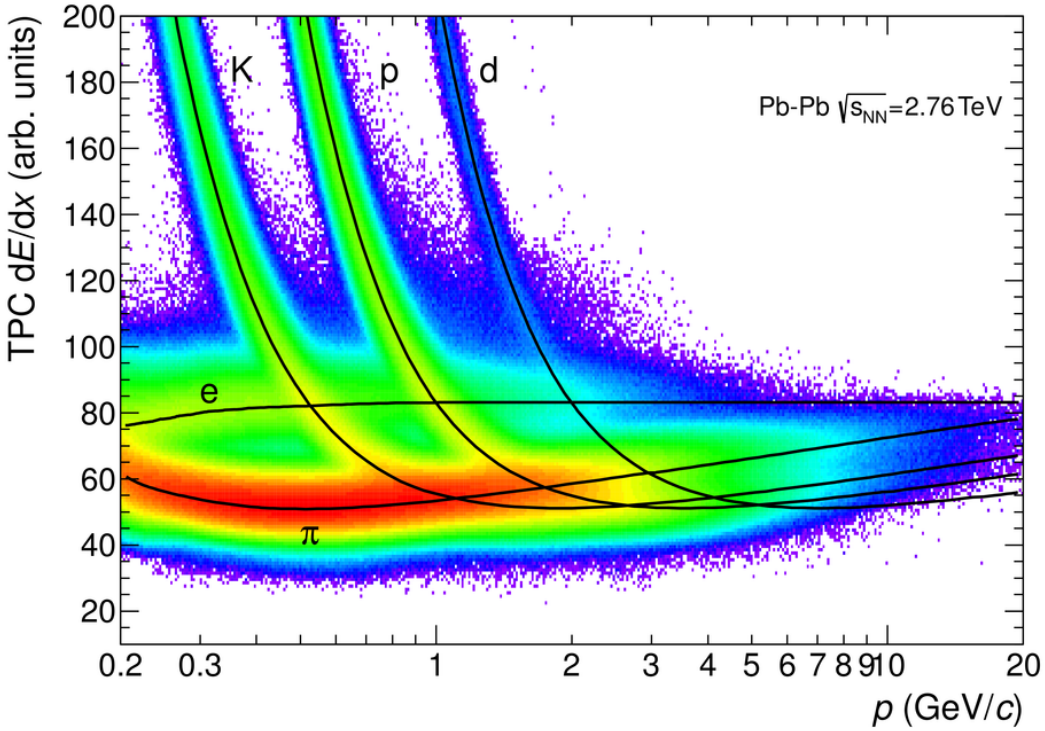

Figure 4.10: The PID capabilities of the TPC [67].

particle's momentum can then also be taken from measurements done by other detectors and can be used, together with the speed calculated by the TOF, to calculate the mass of the particle and hence its species.

The TOF is made up of Multigap Resistive Plate Chambers (MRPCs), which consist of two stacks of 400 μm thick glass plates separated by 250 μm thick gas gaps. This is placed between two electrodes creating an electric field in the gas. A traversing particle ionizes the gas and creates a cascade which is detected. The MRPCs are organized into a cylindrical surface at a radius of 370 cm from the beam line covering a pseudorapidity range of $|\eta| < 0.9$ creating a total active area of 141 m^2. The time resolution of the ALICE TOF is on the order of 80 ps for pions around 1 GeV/c. This allows kaons to be distinguished from pions up to 3 GeV/c and kaons from protons up to 5 GeV/c with a separation of two sigma.

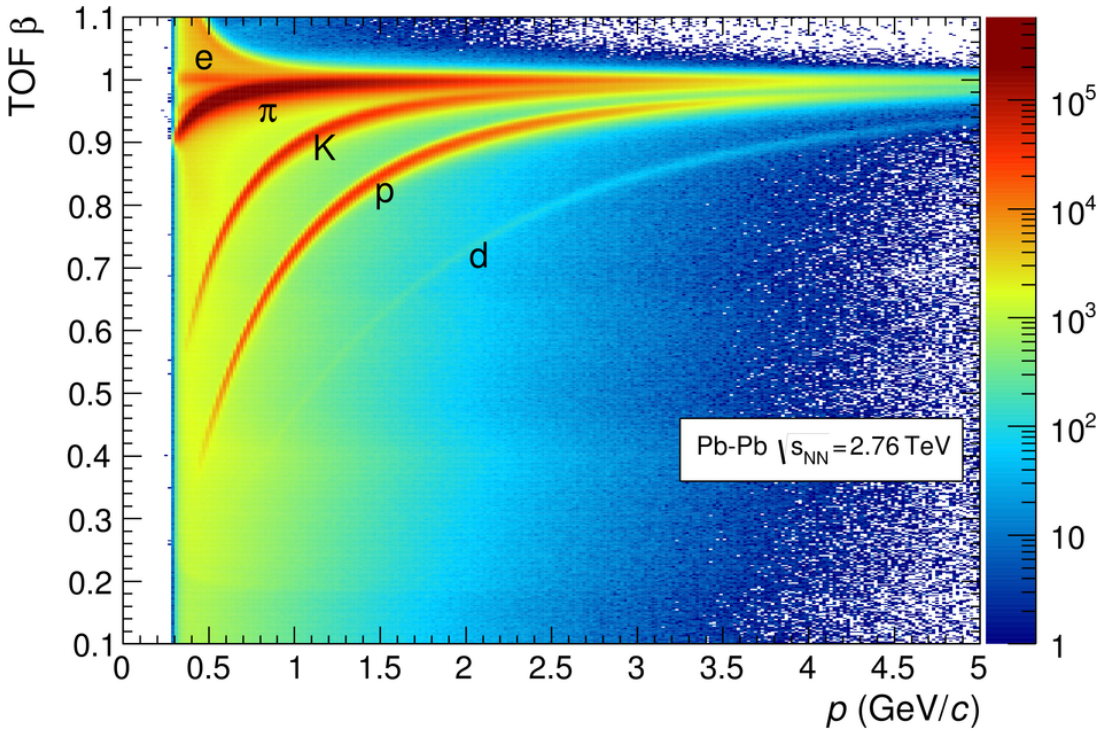

Figure 4.11: The PID capabilities of the ALICE TOF detector [67].

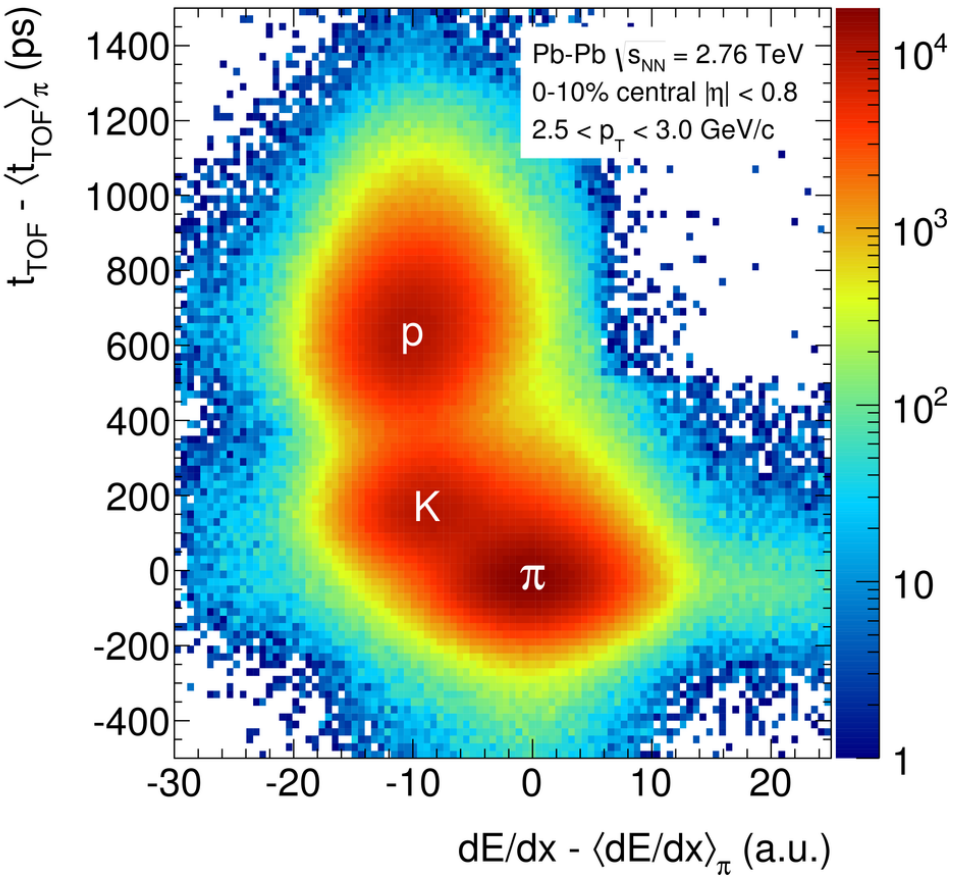

Figure 4.12: The combined particle identification capabilities of the TPC and the TOF detectors [75].

Chapter 5

Data selection

This chapter will discuss the data selected for this thesis. This includes the data, event and track selections used as well as the event level variables used to differentiate the data. These variables include multiplicity, transverse momentum and transverse sphericity.

5.1 Data sample

The data used in this thesis is from proton-proton (pp) collisions recorded in 2010 during the LHC run 1. The events were recorded at a centre-of-mass energy of $\sqrt{s} = 7$ TeV. The data is denoted internally in ALICE as LHC10d and only the second reconstruction pass over the data is observed, obtained with the AOD 147 dataset. The ten runs[1] with the highest quality[2] and that had the highest number of events were selected for this thesis. The total number of good events that pass the event selection criteria below is $33 \cdot 10^6$. These runs were selected because they include only events corresponding to actual physics data sets (no data corresponding to cosmic particle measurements, or LHC luminosity scans), they were among the runs that had the highest reconstruction efficiency and also all detectors needed for this analysis were included in the data taking.

Corresponding Monte Carlo data was generated to accompany the real data. The MC simulations were performed with settings corresponding to the state of the LHC collider and the ALICE detector at the time of the data taking. Pythia 6 was used to generate the events with a Perugia0 tune and GEANT3 was used to simulate the detector response.

[1] The exact internal run numbers are: 126403, 126404, 126405, 126406, 126407, 126408, 126409, 126422, 126424, 126432

[2] ALICE tool for observing run quality and statistics http://alimonitor.cern.ch/configuration/

5.2 Event and Track selection

For an event to be selected for the analysis it has to pass the minimum bias trigger. Events that contain background interactions such as beam-gas or beam-halo as well as events with pile-up are rejected from the minimum bias trigger. Additionally, to pass this trigger an event is required to have a signal in one of the two inner layers of the SPD or in one of the V0 detectors. Furthermore, a condition is placed on the position of the primary collision along the beam line i.e. the position of the z_{vtx}. This is due to the limited acceptance of the ALICE central barrel. Events occurring too far along the beam line could partially miss parts of our detector causing a reduced efficiency. Therefore a requirement is placed that the primary vertex must be within 10 cm from the center of the detector or $|z_{vtx}| < 10$ cm. There are about $33 \cdot 10^6$ events that correspond to the selection criteria thus far.

There are additional selection criteria for tracks in these events. Firstly, only particles with a transverse momentum $p_T > 0.15$ GeV/c were selected since particles of lower transverse momentum can spiral within the magnetic field of the detector and are detected with a lower efficiency in general. Secondly, only primary tracks in the pseudorapidity range $|\eta| < 0.9$ were selected due to limitations of the detector. The trajectories of the particles were measured and calculated using the ITS and the TPC detectors. A track is required to have at least 70 clusters in the TPC (out of a maximum possible number of 159) with a maximum value of χ^2 per TPC cluster of 4.0 corresponding to 2 degrees of freedom per cluster. The track must also project back to the vertex of primary collision. With respect to the primary vertex location, the cut-off on the distance of closest approach of each primary particle has a p_T dependence and must be less than $0.018 + 0.035 p_T^{-1.01}$ cm in the transverse plane and 2 cm in the beam direction. Particles outside these parameters are not considered to be part of the event.

An additional selection is implemented for particles used to calculate the correlation function. As was shown in section 3.4 in figure 3.13 the Ridge is only present for particles with a transverse momentum in the range $1 < p_T < 3$ GeV/c and therefore only particles that fall into this range are used to calculate the correlation function in this thesis.

5.3 Event shape analysis

Multiplicity is one of the main observables used to differentiate high energy particle collisions. However, as an observable, it is not particularly sensitive to the underlying physical mechanisms leading to the production of particles in an event. A single high energy "hard" parton scattering causes the emission of jets which can result in a high multiplicity event. On the other hand, a collision containing many low energy "soft" scatterings can also create an event of high multiplicity. While it is true that the ratio of hard to soft events can change slightly at different multiplicities, multiplicity itself is not enough to efficiently differentiate these kinds of events. This is where an event shape analysis can be useful. Events with single hard parton scatterings are in the perturbative QCD regime and tend to lead to back-to-back jets resulting in a very anisotropic or "jet-like" event with collimated particle trajectories. These events tend to have isolated "islands" of particles in the final state angular phase space. In contrast, multiple soft interactions characterised by non-perturbative QCD particle production will tend to produce a more isotropically distributed event with the final state particles and their momenta spread more evenly in the angular phase space. A final state event shape variable should be more efficient at differentiating events with these different types of underlying processes. By classifying events according to their event shape, it should be possible to significantly enhance the fraction of the desired type of events in the analysed event sample.

5.3.1 Transverse sphericity

Transverse Sphericity (S_T) is a momentum space event shape observable. It describes how isotropically tracks and their momenta are distributed in an event. It is a scalar observable calculated using the eigenvalues of the transverse momentum matrix S_{XY}:

$$S_{XY} = \frac{1}{\sum_i p_{T\,i}} \sum_i \frac{1}{p_{T\,i}} \begin{pmatrix} p_{x\,i}^2 & p_{x\,i} p_{y\,i} \\ p_{x\,i} p_{y\,i} & p_{y\,i}^2 \end{pmatrix}. \tag{5.3.1}$$

The transverse momentum matrix is defined using the transverse momenta of all of the primary charged particles in an event. Only transverse momenta are considered in order to avoid a bias from the boost along the beam axis. The eigenvalues of the transverse momentum matrix λ_1 and λ_2 ($\lambda_1 \leq \lambda_2$) are sensitive to differences in the total momentum

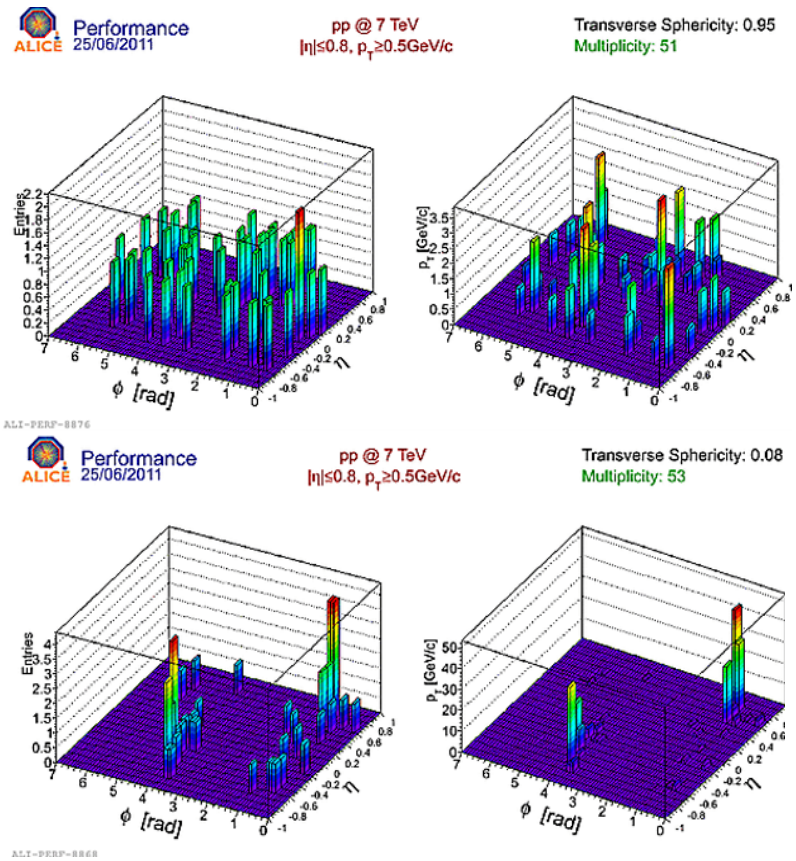

Figure 5.1: Comparison between two events of similar multiplicities. The particle distribution and the transverse momentum distribution for an event with an isotropic structure can be seen on the top panels, corresponding to a high sphericity event. The bottom panels show the particle and transverse momentum distributions for an event with a jet-like structure corresponding to a low sphericity event [76].

in the transverse plane. Let $\hat{a}$ be the axis in the transverse plane with the highest projection of momentum $p_a = \sum_i |\vec{p}_{T\,i} \cdot \hat{a}|$ and $\hat{b}$ be the axis in the transverse plane perpendicular to $\hat{a}$. The closer the value of the projection of transverse momentum along the $\hat{b}$ axis ($p_b = \sum_i \left|\vec{p}_{T\,i} \cdot \hat{b}\right|$) is to p_a the closer the two eigenvalues λ_1 and λ_2 are to each other. The two extreme cases are when $\frac{p_b}{p_a} = 1$, corresponding to when the total momentum projection along axis with the highest momentum projection is equal the momentum projection along the axis perpendicular it, and $\frac{p_b}{p_b} = 0$, corresponding to the case when all the momentum is directed along a single axis in the transverse plane. In these extreme cases, the ratios of the eigenvalues would be $\frac{\lambda_1}{\lambda_2} = 1$ and $\frac{\lambda_1}{\lambda_2} = 0$ respectively. This allows the transverse sphericity to be constructed as:

$$S_T = \frac{2\lambda_1}{\lambda 1 + \lambda 2}. \tag{5.3.2}$$

Defined in this way, S_T is a scalar that can have values ranging from 0 to 1, where $S_T \approx 0$ for events with all of the transverse momentum going along a single axis, i.e. "pencil like" events, usually indicating the presence of back-to-back jets, and $S_T \approx 1$ for events where the transverse momentum projection along the main axis is equal to the projection along the perpendicular axis, i.e. "spherical" or isotropic events. Figure 5.2 shows the transverse sphericity distribution of pp events simulated in pythia at $\sqrt{s} = 7$ TeV.

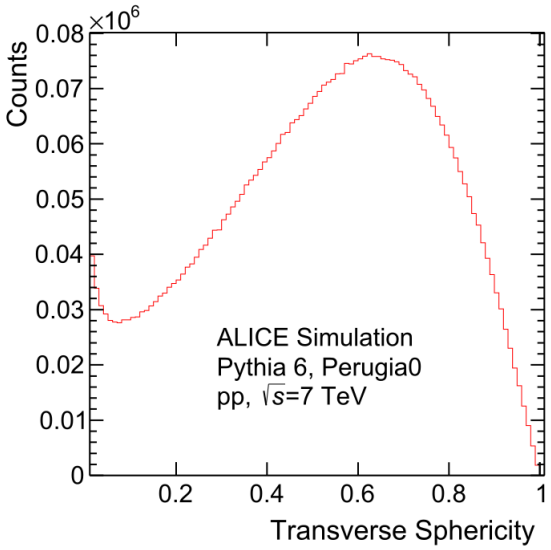

Figure 5.2: The transverse sphericity distribution for simulated pp events.

5.3.2 Multiplicity and p_T dependence on transverse sphericity

There is a weak but inherent correlation between multiplicity and transverse sphericity. On average, events of higher multiplicities will tend to have higher sphericities as well. On the other hand, events with low multiplicities tend to be equally likely to have low and high sphericities. This can be seen in figure 5.3. A measure of correlation between sphericity and multiplicity can be given using the linear correlation coefficient:

$$r_{s_T N_{ch}} = \frac{n \sum_i s_T^i N_{ch}^i - \sum_i s_T^i \sum_i N_{ch}^i}{\sqrt{n \sum_i \left(s_T^i\right)^2 - \left(\sum_i s_T^i\right)^2} \sqrt{n \sum_i \left(N_{ch}^i\right)^2 - \left(\sum_i N_{ch}^i\right)^2}}. \tag{5.3.3}$$

In general the value of the correlation coefficient ranges from -1 to 1. A value of 1 (or -1) would mean that a linear equation describes the relationship between the two variables perfectly with all data points lying on a line. A value of 0 would imply that there is no

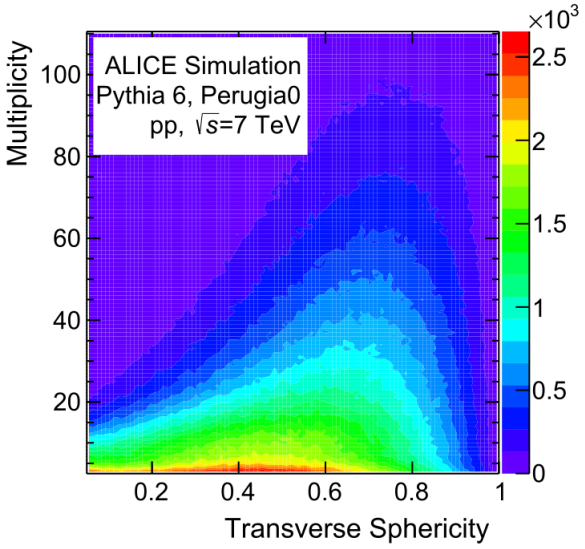

Figure 5.3: Transverse sphericity vs. multiplicity distribution. The linear correlation coefficient for this data is $r = 0.29$ indicating a weak linear relationship.

linear correlation between the two variables. Values of $|r| > 0.7$ indicate a strong linear relationship and values of $|r| < 0.3$ indicate a weak linear relationship. The values of r for transverse sphericity and multiplicity for both simulated real data is always in the $0.15 < r < 0.3$ range, indicating the presence of a weak correlation. This justifies the attempt to use transverse sphericity as a variable of interest since it could be sensitive to physics to which multiplicity is not sensitive.

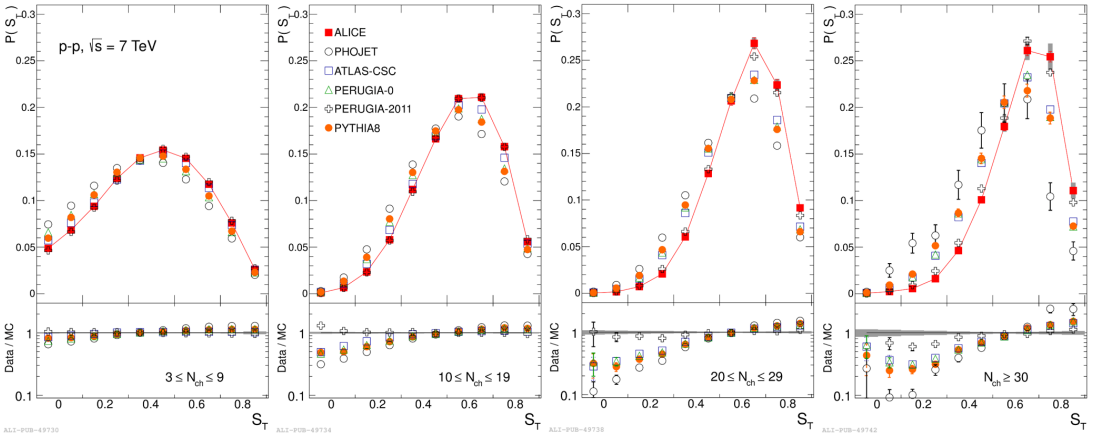

Figure 5.4: The transverse sphericity distribution in several multiplicity classes for both ALICE data and several different MC simulations. The y-axis represents the probability that an event will fall into the given multiplicity range and have the given S_T [77].

Chapter 6

Data Analysis

The practical implementation of the $\Delta\eta - \Delta\varphi$ correlation function described in chapter 3 is presented in this chapter. Due to imperfections in our detector and in data taking, the data that is taken in the experiment is not identical to the particles that are actually produced in our collisions. The procedure used to extrapolate what is seen in the detector to what is actually happening physically is described in this chapter. Finally, the procedure used to quantitatively describe the structures in the correlation function is described.

6.1 Correlation function

The measured correlation function is defined slightly differently to the one described in section 3.2. This is because we want our results to represent reality and not the distorted representation of reality given by our detectors. This distortion needs to be accounted for, which is done by implementing a correction factor f to both the signal and background distributions. This is done for each particle pair, taking into account the probability of seeing the two particles as wee see them, given they were actually produced. The calculation of the correction factor f is shown in the next section.

The corrected correlation function calculated from the data can be defined in terms of the corrected signal $S_C(\Delta\eta, \Delta\varphi)$ and background $B_C(\Delta\eta, \Delta\varphi)$ distributions in the same way as in equation 3.2.3:

$$C'(\Delta\eta, \Delta\varphi) = \frac{\frac{1}{N_{pairs}^{signal}} S_C(\Delta\eta, \Delta\varphi)}{\frac{1}{N_{pairs}^{mixed}} B_C(\Delta\eta, \Delta\varphi)}, \tag{6.1.1}$$

or in terms of the associated yield per trigger particle as is the case in this work:

$$C(\Delta\eta, \Delta\varphi) = \frac{\frac{1}{N_{pairs}^{signal}} S_C(\Delta\eta, \Delta\varphi)}{\frac{1}{B_C(0,0)} B_C(\Delta\eta, \Delta\varphi)}. \tag{6.1.2}$$

The corrected signal and background distributions are calculated as follows:

$$S_C(\Delta\eta, \Delta\varphi) = \sum_{p_{T,1}, p_{T,2}} f(p_{T,1}, p_{T,2}) S(\Delta\eta, \Delta\varphi, p_{T,1}, p_{T,2}), \tag{6.1.3}$$

$$B_C(\Delta\eta, \Delta\varphi) = \sum_{p_{T,1}, p_{T,2}} f(p_{T,1}, p_{T,2}) B(\Delta\eta, \Delta\varphi, p_{T,1}, p_{T,2}). \tag{6.1.4}$$

This procedure calculates the corrected signal and background distributions by summing up the contributions to the uncorrected distribution of each individual pair of particles, weighted by some factor f called the correction factor. This factor depends on the properties of the particular pair of particles being observed.

An additional correction is done to the background distribution. The background distribution mixes particles from different events, and therefore it is possible for particles originally produced at similar angles relative to the beam line to fly into different parts of the detector. This is because the primary vertex location of events taken into consideration in this analysis can vary by up to 20 centimetres. Mixing particles from different events with vastly different z-vertex locations could potentially create new signatures or alter existing signatures in the background distribution that are not present in the signal distribution. All particle pairs comprising the signal distribution originate from the same event and thus also from the same z-vertex position. Therefore, to improve the estimation of the background, each event is only mixed with other events which fall within the same, 2 cm wide, z-vertex bin. The angles between particles in these mixed events are then compared and added to the background distribution.

6.2 Corrections

Several factors exist which could bias the data in some way, possibly leading to incorrect interpretations of the data. These factors need to be calculated and implemented by means

of the correction factor f. The procedure used to calculate the correction factor is described in this section.

Two sets of generated Monte Carlo (MC) events are needed to accurately calculate the correction values. The first set is generated directly from the MC simulation based on the input parameters which correspond to the primary collision specifications of the LHC (particle type, collision energy). This data set is referred to as the MC truth and consists of the all the particles that are actually formed. It is what we would see if we had a perfect detector, covering the full solid angle and had a 100% detecting and differentiating efficiency as well as energy resolution. Since this is not the case, a second set of Monte Carlo events is needed. The second set of data, referred to as reconstructed MC, contains information about which particles are actually detected by our detectors. In other words, which tracks are actually recorded by the experiment on which the analysis is done. This set is obtained by running tracks through a transport package. This package simulates the transport of the particles through the various materials that make up the beam pipe and the detector. This includes particles being scattered or absorbed by the materials that they pass through, causing some of the particles to be missing in the final state. This package also simulates the detector response, including possibilities that some aspect of the particle is misidentified or even that the particle is missed altogether by the detector. Examples of particles that can be missed by the detector are those that pass through blind or broken spots in the detector, those that pass through parts of the detector during dead times of that particular part of the detector or even particles that don't pass through any part of the detector at all. The initial events in this data set are the same as the events in the MC truth data set meaning we can have a direct comparison between the two data sets enabling us to quantify the effect of the detector on the real data. In this work, the transport package GEANT3 [78] is used, giving us both the transport of the particles through the detector volume and the detector response. After this, the entire reconstruction and track selection sequence is applied on this data set in an identical way to the actual data measured by the detector.

What we obtain in this way is a data set that mirrors our actual measured data set, specifically regarding how it has been altered during any step in our measurement and reconstruction procedure. However, in contrast with the measured data, for this set we have information about the actual "physical" events that were originally produced.

Performing an identical analysis on the two respective Monte Carlo data sets, MC truth and reconstructed MC, allows for them to be compared. Quantifying the differences between these two data sets allows us to extrapolate our measured data to some form of its own physical truth. We can calculate how many particles are lost, misidentified or influenced by our detection procedure and whether these changes are uniform or occur more often in specific parts of our phase space. This can be quantified in the form of a correction factor f.

6.2.1 Correction factor

The correction factor is the constant of proportionality linking the number of generated particles (N_{gen}) in an event with the number of particles registered by our detector and analysis procedure (N_{det}) as follows:

$$N_{\text{gen}} = f \cdot N_{\text{det}}. \tag{6.2.1}$$

This correction factor is not just a single number but rather a tensor since the efficiency of our detector is not necessarily homogeneous but can depend on various factors. These factors include which part of the detector the particle passes through, particle momentum and particle type. Since the ALICE detector covers the full azimuthal angle, the part of the sub-detectors that the particle passes through can be characterized using pseudorapidity and the position of the z vertex. The particle momentum can be characterized by the particles transverse momentum together with its pseudorapidity. The misidentification of the type of particle does not play a role in this analysis since we are taking all charged particles independently of their charge sign, mass or flavour. Neutral particles cannot be misidentified as charged particles by our detector since the main sub-detectors of ALICE (namely the TPC and ITS) are not sensitive to neutral particles at all. Thus the three variables on which the correction factor will depend in our analysis are pseudorapidity, z vertex location and transverse momentum:

$$f(\eta, z_{vtx}, p_T) = \frac{N_{\text{gen}}}{N_{\text{det}}}. \tag{6.2.2}$$

The correction factor is larger than 1 because fewer particles are detected than generated.

A deficit of particles exists because some of them are missed since we do not have an ideal detector reconstruction efficiency. Factors contributing to a surplus of particles not originally present in the event include contamination from secondaries or pileup events. Pileup is the term that refers to multiple pp collisions within a single bunch crossing, resulting in an uncertainty in which particle came from which collision. Pileup events are categorically excluded from all data and the fraction of secondaries in an event is under 1% for hadrons in the transverse momentum range of this thesis, whereas around 20% of particles are missing on average due to reconstruction efficiencies.

There are various reasons why a track might not be reconstructed in our detector:

- The particle could simply pass outside of the sensitive area of our detector,
- The particle could reach the detector but the path of the particle in the detector could be too short to be reconstructed (for example, at least 70 clusters in the TPC are required for reconstruction),
- If the particles momentum is too low it can curve too much in the magnetic field of the detector causing it to spiral inside of the detector and become unreconstructable,
- The fact that the particles curve in the magnetic field is useful since a particle that originally flies into a dead or blind part of the detector can curve out of it and still be detected. However, if a particle's momentum is too high, its track barely curves and so its entire length can be in the blind zone of the detector causing it to be missed.

A projection of the correction factor onto its main axes can be done to show how it depends on each of the variables.

Transverse momentum dependence

The correction factor dependence on the particle's transverse momentum is shown in figure 6.1. The plot shows charged particles in the p_T range used to create the correlation functions in this work, $1 - 3\,\mathrm{GeV}/c$. On this p_T scale the efficiency drop at low p_T due to excess bending in the magnetic field is not visible since this only begins to occur below the $0.5\,\mathrm{GeV}/c$ mark. In the first half of our chosen interval the efficiency is maximal acquiring

a value of about 82% and begins to drop slightly by a few percent around the 2 GeV/c mark where the tracks start to straighten out and become more likely to pass entirely in the detectors blind spots.

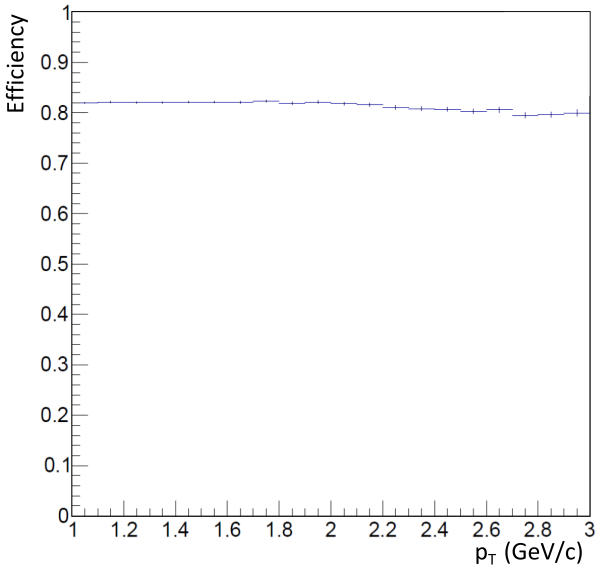

Figure 6.1: Efficiency as a function of p_T. Simulation done with Pythia Perugia-0 events at $\sqrt{s} = 7$ TeV and GEANT3 as the transport package.

Pseudorapidity dependence

The correction factor dependence on the particles pseudorapidity is shown in figure 6.2. The plot shows charged particles in the pseudorapidity range $\eta < |0.9|$. The efficiency is quite constant around the 82% mark with drops towards the edges of the pseoudorapidity range, since at those points the tracks start to leave the full radial track length pseudorapidity coverage of the TPC. Particles that only partially pass through the TPC volume have a smaller chance of leaving the requited number of clusters in the TPC for reconstruction. There is also a slight drop in efficiency around $\eta = 0$ since this is where the central drift electrode is situated. The electrons from particles have the farthest to travel and can even end up on opposite sides of the TPC if the track passes through the central drift electrode.

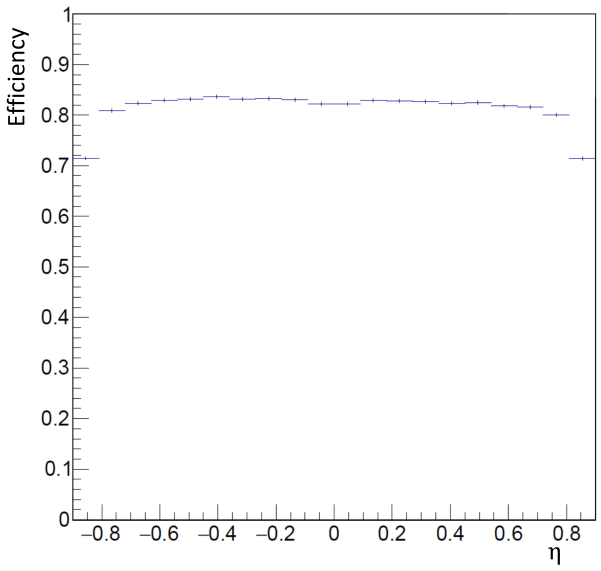

Figure 6.2: Efficiency as a function of η. Simulation done with Pythia Perugia-0 events at $\sqrt{s} = 7$ TeV and GEANT3 as the transport package.

Z vertex dependence

The correction factor dependence on the position of the primary vertex along the beam line Z_{vtx} is shown in figure 6.3. The plot shows charged particles that originate from $Z_{vtx} < |9|$ cm. The efficiency is quite constant with a slightly larger value at negative values of Z_{vtx} and has drops towards the edges of the Z_{vtx} range since at those points the tracks approach the edge of some parts of the detector, mainly the ITS. There is also a slight drop in efficiency around $Z_{vtx} = 0$ for similar reasons as in the pseudorapidity case.

6.2.2 Contamination

Contamination occurs when particles that should not be included in the analysis are mistakenly included. There are a few possible sources of contamination; mainly contamination from secondaries and from particle misidentification. The misidentification of one type of hadron as a different type plays no role in this analysis since they are all taken equally. Other types of misidentification (neutral particle as a charged particle or vice versa) are either taken into account by the correction factor already or are so small to be negligible [79]. On the other hand, contamination from secondaries could possibly play a role in the analysis, reducing the real value of the correction factor when the secondaries are removed. The problem with simply using a MC simulation and counting the fraction of

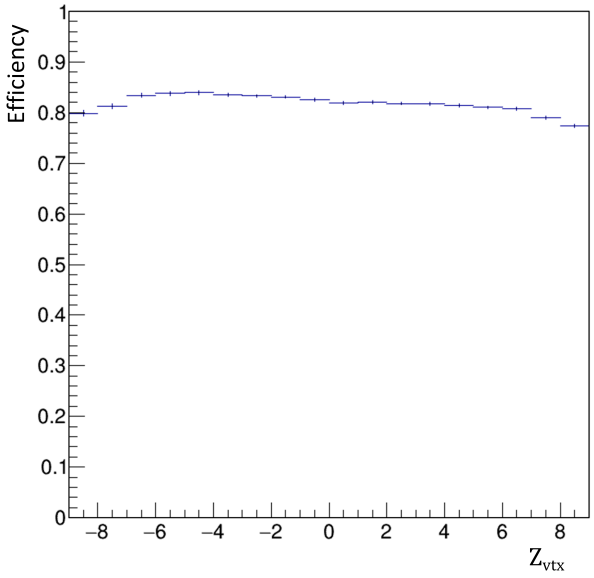

Figure 6.3: Efficiency as a function of Z_{vtx}. Simulation done with Pythia Perugia-0 events at $\sqrt{s} = 7$ TeV and GEANT3 as the transport package.

secondaries in the output event is that the fraction of secondaries is highly model dependent [80]. Using the same MC model as used for the correction factor above (Pythia Perugia-0 pp events at $\sqrt{s} = 7$ TeV) gives a flat value of about 1% (slightly decreasing with p_T) for the fraction of secondaries in the p_T range observed in this work. A model-independent, data-driven corrective procedure called the *DCA-based contamination correction* method described in [79] was found to be in agreement with the MC method with negligible differences between the two methods. Therefore the simple MC model was used to arrive at the final correction factor.

6.3 Data quantification procedure

The corrected correlation function described above gives a 3D shape with various structures of varying shapes and sizes. Observing the correlation function in this form can give a qualitative explanation of the changes to the correlation function under different conditions, however some further processing is required to quantify the data for interpretation.

In this work, two procedures are implemented in order to obtain a more quantitative description of the data. Firstly, the 3D correlation function is projected onto its axes in

various ranges. Secondly, shapes in the correlation function are fit and the fit function parameters were extracted.

6.3.1 Projections

A total of five different projections are performed in order to properly describe the data. The two primary projections are on the two main axes of the correlation function, $\Delta\eta$ and $\Delta\varphi$, for the full range of data. The other projections are also on the same two axes, however, for only specific subsections of the data.

This method of projecting the data onto the axes using only a certain subsection of the data was inspired by one of the original ways in which the Ridge was isolated by the CMS collaboration, shown in figure 6.4 [46]. The Ridge was isolated from the background of the jet peak by cutting the jet peak out, removing all data points from the correlation function within $\eta \lessapprox |2|$, looking only at the yield outside this region.

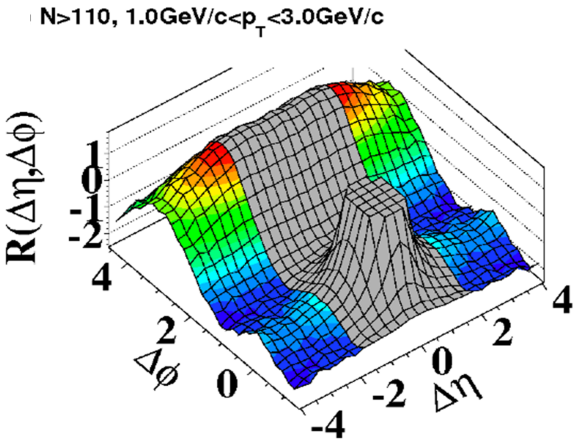

Figure 6.4: CMS cut on the most extreme values of $\Delta\eta$ in order to calculate the yield of the near side ridge [46, 81].

Since this work is focused on measuring how transverse sphericity affects the size and shape of the near side jet peak, two of the additional projections will be on the $\Delta\eta$ and $\Delta\varphi$ axes for particle pairs within the jet peak. The final projection will be for particle pairs similar to those that the CMS collaboration used to measure the ridge, namely a projection onto $\Delta\varphi$ for particle pairs outside the innermost values of $\Delta\eta$, cutting out the jet peak. Examples of these projections can be seen in figure 6.5. The jet peak was

empirically determined to by bounded by $|\Delta\eta| < 1.2$ and $|\Delta\varphi| < 1$ and thus these values were chosen as the values to cut on in order to isolate the jet.

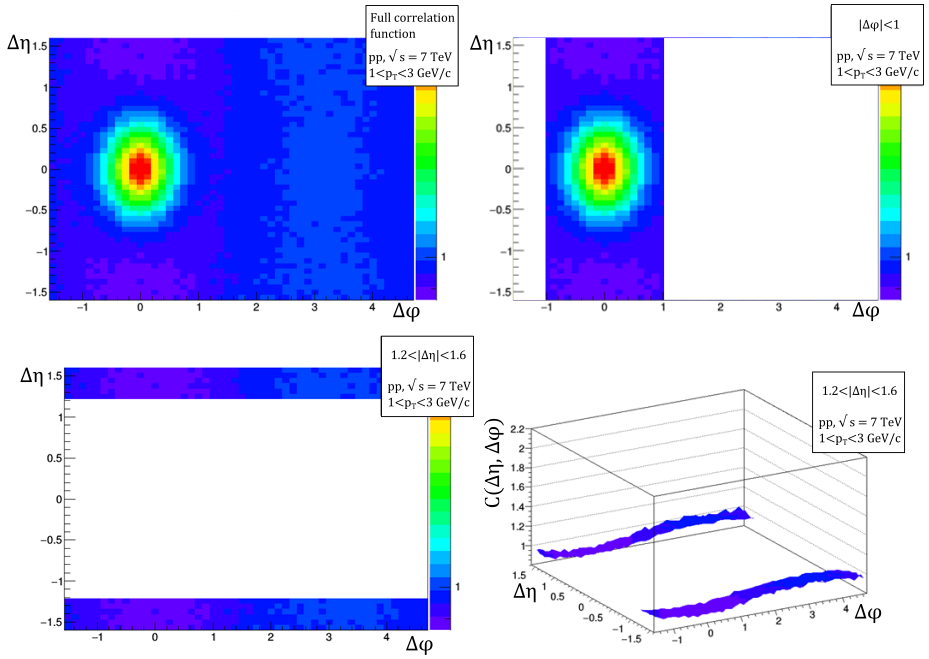

Figure 6.5: Some of the cuts on the correlation function used in this thesis to isolate the jet and the background. The bottom two plots demonstrate the same cut from a different perspective.

The shape of some of the projections are shown in figure 6.6.

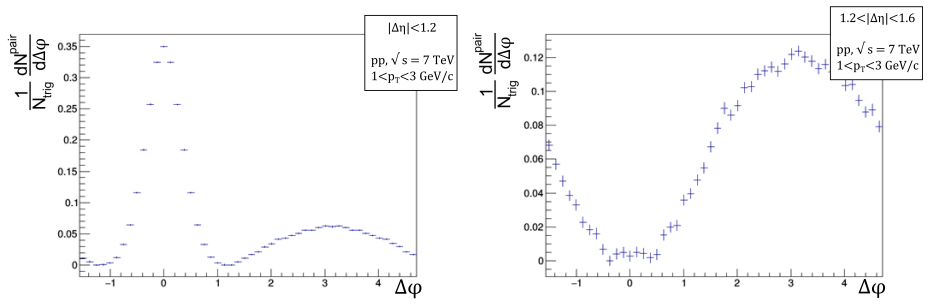

Figure 6.6: Examples of projections onto the $\Delta\varphi$ axis for a cut at $|\Delta\eta| = 1.2$. The left plot shows the projection inside the cut while the right plot shows the projection outside the cut.

6.3.2 Fitting and peak value extraction

In order to quantify the size and shape of the near-side jet peak, a function is fit to it which can then be analysed, inferring information about the peak. In this way the effect that the transverse sphericity cut has on the jet peak can be verified.

Before the fit is applied to the jet peak, it is first isolated from the background long range structures. The projection on the $\Delta\eta$ axis is performed for values of $|\Delta\varphi| < 1$ and a constant is subtracted from the projection in order to remove the underlying long range structure and look at values present only in the jet peak. This is done by implementing a "zero yield at minimum" (ZYAM) subtraction, shifting the entire projection so that the lowest points in the projection have a value of zero. Therefore only particle pairs present in the jet peak will be present in this projection. The projection on the $\Delta\varphi$ axis is performed for values of $|\Delta\eta| < 1.2$. However, the projection of the long range structure on this axis is not flat and thus a simple ZYAM subtraction is not enough to isolate the ridge from the underlying structure. Instead, a projection is performed for all values outside the jet peak $1.2 < |\Delta\eta| < 1.6$ and this shape is then subtracted to remove the background from the long-range correlations.

The Lorentzian function described in equation 6.3.1 was found to be the best fit for the shape of the near-side jet peak after the projections were performed:

$$f(x) = I\left[\frac{\gamma^2}{((x - x_0)^2 + \gamma^2)}\right] + f_0. \tag{6.3.1}$$

Three useful values can be extracted from such a fit: firstly the height of the jet peak, given by I, can be extracted. An effective way of extracting this measurement from the data is not by taking it from the fit but by measuring the yield of particles in the central bin. The yield of particles in the central bin is proportional to the height of the correlation function above that bin. Secondly, the full width at half maximum (FWHM) of the peak, from here on called the width of the peak, can be extracted from the fit and is given by 2γ. Finally, the proportion of particles contained in the peak, called the yield of the peak, is given by integrating the area under the fit of the peak.

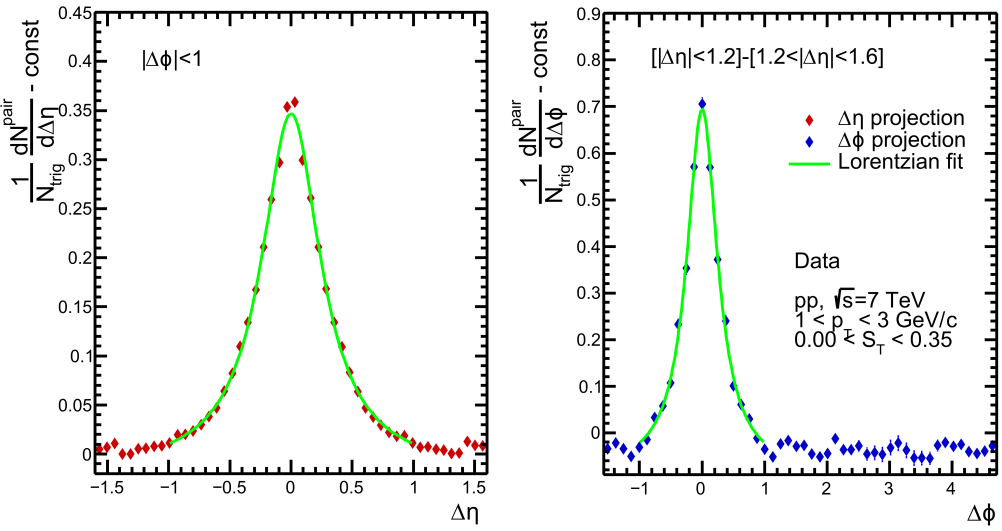

Figure 6.7: An example of a Lorentzian fit to the data for projections onto both axes.

Chapter 7

Experimental results

In this chapter, the results observing the two-particle angular correlation function in dependence on the event shape are presented. The analysis is performed for pp collisions at $\sqrt{s} = 7$ TeV. The dependence of the correlation function on the transverse sphericity is studied for all events and for the events with highest multiplicities. The results are then compared by performing projections of the correlation function onto various axes. Finally the width and yield of the jet peak are quantified in dependence to the event transverse sphericity.

7.1 Correlation function dependence on S_T

The dependence of the $\Delta\eta - \Delta\varphi$ correlation functions on transverse sphericity is shown on figure 7.1. The data shown here is for events of all multiplicities. Data corresponding to events within the top 1.5% of multiplicities appears almost indistinguishable to the naked eye and is therefore only presented in the quantitative analysis. The events are separated into five classes of S_T. The classes were chosen so that the class with the highest S_T and the class with the lowest S_T contain the same number of events. This number was chosen to be 15% of all events in order to minimize contamination from events of more central sphericities. The highest sphericity class contains events with $S_T > 0.795$ and the class with the lowest sphericity contains events with $S_T < 0.346$. The events of central S_T are then separated into three classes of equal size in S_T to create a total of five classes. The names of the classes are rounded off to 2 decimal places for the sake of brevity, however the calculations are performed with the actual calculated values. The classes are as follows: Class 1 = $0.00 < S_T < 0.35$, class 2 = $0.35 < S_T < 0.50$, class 3 = $0.50 < S_T < 0.64$, class

$4 = 0.64 < S_T < 0.80$ and class $5 = 0.80 < S_T < 1.00$. In order to enhance and clarify the structures in the correlation function, the main jet peak is truncated. The cut-off on the $z-$azis is the same for all of the plots so the underlying structures can be compared, however the height of the main jet peak is truncated by a different amount in different cases.

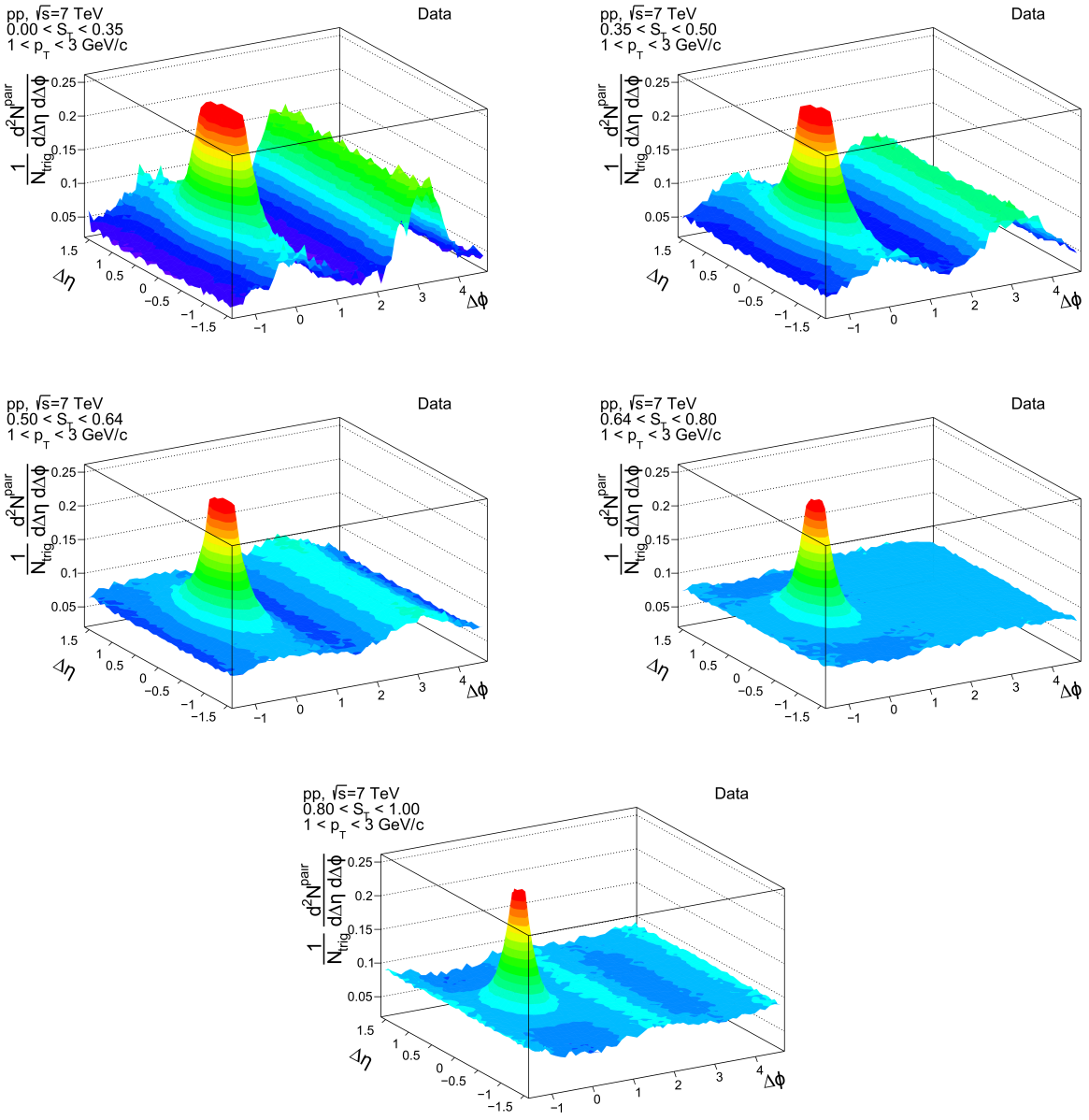

Figure 7.1: The $\Delta\eta - \Delta\varphi$ correlation functions in dependence on transverse sphericity for minimum bias events. The main jet peak is truncated for clarity.

As can be seen in the plots, there are drastic changes in the shape of the correlation function $(\Delta\eta - \Delta\varphi)$ in dependence of S_T. Several notable signatures of correlation sources

mentioned in chapter 3 can be seen in various degrees on the plots. The most visible characteristic which is clearly seen in all of the S_T cases is a clear, near-side, jet peak at $(0, 0)$. This jet peak is particularly pronounced for cases of small S_T, corresponding to jetty or pencil-like events, and appears to gradually shrink in all dimensions as the S_T of the events increases. As mentioned in chapter 3, this peak is associated mainly with hard, high-p_T processes and to a lesser extent with Bose-Einstein correlations. This would indicate that choosing events with lower S_T would indeed choose events containing a higher fraction of these hard processes and vice-versa. It is interesting to note that even in the case with highest S_T the jet peak remains present meaning that S_T as a variable cannot be used to completely eliminate all hard processes from events. The shape of the jet peak also appears to change, going from a flatter broader shape to a more circular one. This could indicate a change in the ratio of correlation sources, but it is not exactly clear from the presented figures and further analysis is needed to quantify it. An exact quantification of the change in the jet peak dimensions can be seen in the next sections.

The second noticeable feature is the away-side ridge, characterized as a correlation spanning over the full range of $\Delta\eta$ located at $\Delta\varphi = \pi$. This ridge originates from momentum conservation, primarily in the form of back-to-back jets that head in opposite directions in their center of mass frame, which corresponds to particles flying out at opposite azimuthal angles. Similarly to the near-side jet peak, the away-side ridge is extremely pronounced in cases of small S_T and decreases in size as S_T increases. Contrary to the behaviour of the near-side jet peak, the away-side ridge does not remain present across all sphericities but appears to vanish and at the highest values of S_T even appears inverted when compared to the baseline. This would indicate a reduction in the fraction of jets present in the sample with increasing S_T, but could also indicate the presence of other phenomena which will be further discussed in the discussion chapter.

A feature of the correlation functions that might be missed is the position of the baseline, or the "lowest point", in the correlation above which the other features protrude. In the cases of small S_T the baseline is consistent with zero. However, as S_T increases and the events become more "spherical", the baseline increases as the yield in the jet-peak and away-side ridge appears to decrease. The result is that the correlation function is overall more flat. This would indicate that particles may be produced at any angles with regard to one another in high S_T cases which doesn't appear to be the case for low S_T events.

Another surprising feature of the correlation is what appears to be a near-side ridge visible in low S_T events. This is characterized by a correlation spanning over a long range of $\Delta\eta$ located at $\Delta\varphi = 0$. This ridge can be seen protruding out from the jet peak at low S_T events and decreases towards medium S_T events before vanishing and becoming inverted towards the highest values of S_T. This ridge is more visible in the medium S_T events because the main jet peak appears to shrink faster with S_T than the ridge, leaving it more visible, despite being reduced in size. As mentioned previously, this correlation structure could potentially be used as an indicator for the formation of QGP. However, in this situation it doesn't appear to be the case and a more detailed discussion of this matter can be found in chapter 9.

A slight transverse ridge structure may be observed in the $0.64 < S_T < 0.80$ case. This is characterized as a correlation located at $\Delta\eta = 0$ and is spread out over a wide $\Delta\varphi$ range. Signs of this structure are hidden in the other S_T cases by other, more prominent, structures. The origin of this structure is usually attributed to resonance decays and potentially gluon string fragmentation.

The final notable structures can be seen on the $0.80 < S_T < 1.00$ case corresponding to events of the highest transverse sphericity. These structures can be seen as a correlation spanning over the full range of $\Delta\eta$ located at $\Delta\varphi = \frac{\pi}{2}$ and $\Delta\varphi = \frac{3\pi}{2}$. They arise if there is a tendency for particles to fly out at right angles relative to each other in the azimuthal direction, irrespective of their pseudorapidities. These structures are surprising as they are not present in any previously known correlation functions. The origin of these structures in the supposedly most "spherical" of events is discussed in chapter 9.

7.2 Projections

In order to compare the differences in the structures between different values of S_T in a more meaningful way, projections onto the axes of the plots can be made. These projections allow certain aspects of the plots to be more visible, and also allow for better comparisons to be made as the data from different values of S_T can be shown on the same set of axes. This can be seen in figures 7.2-7.6. A constant background value has been subtracted from all of the projections in order to push them all down to the same baseline. This greatly improves the overall visibility of the graphs and allows for better comparisons.

This constant is different for each value of S_T and for each different projection.

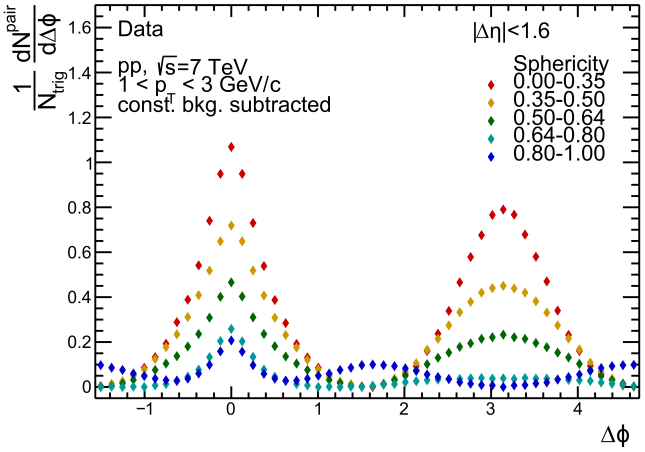

Figure 7.2: Projection of the $\Delta\eta - \Delta\varphi$ correlation function onto the $\Delta\varphi$ axis for all values of $\Delta\eta$ in five different S_T classes.

Figure 7.2 shows the projection of the $\Delta\eta - \Delta\varphi$ correlation function onto the $\Delta\varphi$ axis for all values of $\Delta\eta$ in five different S_T classes. In this view, the near-side peak is composed of the original jet peak as well as any near-side ridge while the away-side peak is composed entirely from the away-side ridge. In this representation, the area under the data points gives a measure of the yield of particles above the baseline for that particular structure. It can be seen that for lower values of S_T the yields on the near-side and the away side are similar, which was hidden from us in the original view. The near side peak is slightly taller, whereas the away side peak is slightly wider. As the value of S_T increases, both peaks decrease in size. In the largest S_T class, the near-side peak is still present, even though it is very small. However, the away-side peak completely flattens out and even becomes inverted, leaving way for two new small excesses to form around $\Delta\varphi = \frac{\pi}{2}$ and $\Delta\varphi = \frac{3\pi}{2}$.

In order to differentiate the jet peak contribution to this projection from the long-range ridge contributions, several subprojections can be made. The first of these can be seen in figure 7.3. This is a projection of the $\Delta\eta - \Delta\varphi$ correlation function onto the $\Delta\varphi$ axis for values of $1.2 < |\Delta\eta| < 1.6$. This shows the shape of the correlations far away from the jet peak, isolating the long-range contributions from the jet peak. It can be seen that the long range ridge structures are more pronounced on the away-side than on the near-side. It is also visible that the size of these ridge structures decreases with increasing S_T. At

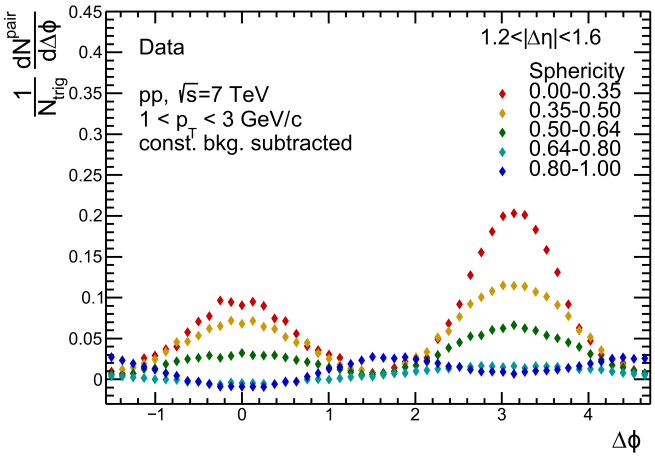

Figure 7.3: Projection of the $\Delta\eta - \Delta\varphi$ correlation function onto the $\Delta\varphi$ axis for values of $1.2 < |\Delta\eta| < 1.6$ in five different S_T classes. This shows the shape of the correlations far away from the jet peak.

the highest S_T both ridge structures vanish leaving only the two new small ridges around $\Delta\varphi = \frac{\pi}{2}$ and $\Delta\varphi = \frac{3\pi}{2}$.

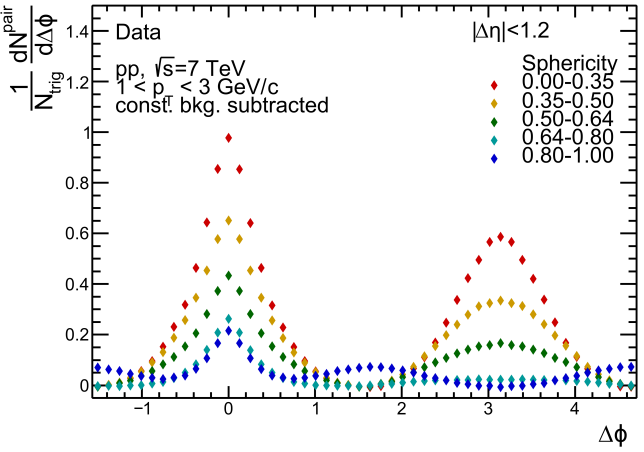

Figure 7.4: Projection of the $\Delta\eta - \Delta\varphi$ correlation function onto the $\Delta\varphi$ axis for values of $|\Delta\eta| < 1.2$ in five different S_T classes. This shows the shape of the correlations around the jet peak.

In order to isolate the jet peak from the underlying ridge structures, the inverse projection can be made projecting the $\Delta\eta - \Delta\varphi$ correlation function onto the $\Delta\varphi$ axis for values of $|\Delta\eta| < 1.2$, which can be seen in figure 7.4. This, however, is not enough since the long range ridges extend below the jet peak. To remove the long range correlations,

a dual projection must be made where the long range contributions ($1.2 < |\Delta\eta| < 1.6$) are normalized and subtracted from the jet peak contributions ($|\Delta\eta| < 1.2$). This can be seen in figure 7.5. A good way to confirm that this method worked is to observe that the away-side is completely flat and equal for all values of S_T. This is what we expect since the away-side contains only the long range correlations. The jet peak appears narrower in this representation but it still experiences a decrease with increasing S_T. It can be seen that the height of the peak shrunk for lower values of S_T but increased for higher values of S_T, indicating that there was indeed a long range depression as opposed to a ridge for these values of S_T. However, the order of jet peak heights is still maintained with inverse S_T.

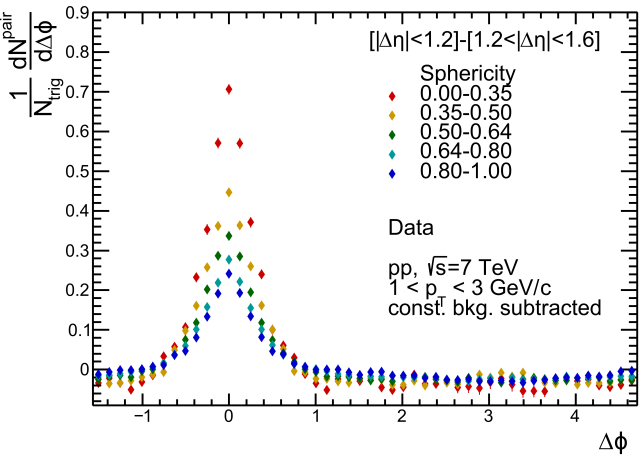

Figure 7.5: Projection of the $\Delta\eta - \Delta\varphi$ correlation function onto the $\Delta\varphi$ axis for normalized values outside the jet peak ($1.2 < |\Delta\eta| < 1.6$) subtracted from values inside the jet peak ($|\Delta\eta| < 1.2$). This subtracts the contributions of the long range correlations from the main jet peak.

Finally the projection of the $\Delta\eta - \Delta\varphi$ correlation function onto the $\Delta\eta$ axis can be made. Since the long range structures in the correlation function extend over $\Delta\eta$ and not $\Delta\varphi$, they are not visible at all when projected onto the $\Delta\eta$ axis, and are completely removed by the constant background subtraction. Therefore, only a single projection onto the $\Delta\eta$ axis is shown for values of $|\Delta\varphi| < 1$, which completely encompasses the jet peak. As expected from the previous projections, the main difference between sphericities is a reduction in the height and apparent width of the jet peak with increasing S_T with no surprising effects present.

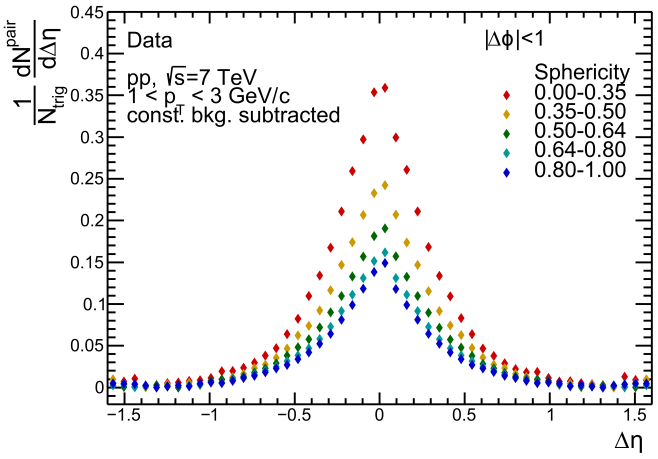

Figure 7.6: Projection of the $\Delta\eta - \Delta\varphi$ correlation function onto the $\Delta\eta$ axis for values of $|\Delta\varphi| < 1$ in five different S_T classes. This shows the shape of the jet peak from the other axis.

7.2.1 Jet peak characteristics

The effect of transverse sphericity on the shape and size of the jet peak can be quantified using a fit on the projection of the jet peak. Three quantifiable observables describing the peak can then be extracted from the fit, these being the height, width and yield of the peak. This enables us to study the S_T dependence of the jet peaks quantitatively, and also to compare the jet peak shape from different angles as well as for events of different multiplicities. The three variables are observed and compared for projections onto both the $\Delta\eta$ and the $\Delta\varphi$ axes as well as for events with all multiplicities and the 1.5% of events with the highest multiplicities. The values for the observables are calculated above the baseline background value described in chapter 6. This baseline can be different for projections onto the two different axes, so the values of the variables can be compared only approximately when comparing the two projections. However, the trends in the data points can be compared.

The first of the variables is the height of the peak and can be seen in figure 7.7. The value of the peak height is not extracted from the fit, but taken as the yield in the central bin. The central bin is the bin located in the middle of the distribution containing the highest yield. The yield of this bin is proportional to the height of the fit, however, it is more convenient to use and it also avoids introducing additional errors through the fitting

procedure. For simplicity sake, the term "height" will be used, even though the data will be showing the yield in the central bin. The height of the jet peak is consistently lower for the top 1.5% multiplicity class compared to the minimum bias class. This would indicate that events that produce more particles also tend to have those particles more spread out on average, with a smaller proportion of the particles in the event produced in jets. In all cases, the data shows a decrease in the height of the peak with increasing sphericity. This decrease in height appears to be quasi-exponential, with a sharper decrease in height for lower values of sphericity and a more gradual decrease for higher sphericities. The decrease cannot be described as a pure exponential since the S_T values on the x axis are not binned in equal intervals. Nevertheless, the decrease appears similar for all projections and multiplicity classes where the height of the peak in the highest sphericity bin is around a third of the height in the lowest sphericity bin. This is consistent with the hypothesis that events containing jets should be less prevalent among higher transverse sphericity events. However, the jet peak never vanishes, even among the events with the highest sphericities. This is contrary to the expectation that the highest sphericity events should be void of jets.

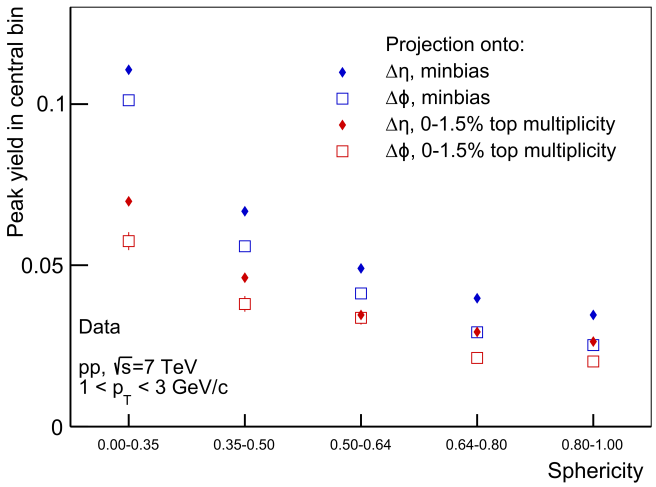

Figure 7.7: The height of the jet peak.

The width of the peak can give an indication of how much the near-side jet peak overlaps any underlying long rage correlations such as the ridge. Therefore it can give a better indication of the extent to which sphericity may be used to remove a jet background from events. The width is obtained by calculating the FWHM of the fitted Lorentzian. The width of the jet peak for all projections and multiplicity classes can be seen in figure

7.8. Unlike the height of the peak, the width of the peak appears to be completely flat within errors, independent on the transverse sphericity class. This means that as the events increase in S_T, the height of the jet peaks shrinks but their width does not. While this might initially seem surprising and unexpected, it actually makes a lot of sense. The height of the peak is reduced which corresponds to there being fewer jets present in the events of higher sphericities but the width of the peak remains unchanged, indicating that the jets that are present have the same distribution of particles within them giving them the same shape. This make sense since jets are produced by hard processes which should be the same if they occur by themselves or in the presence of other soft processes around them. Another characteristic of the width of the jet peak is that there is no significant difference between events of different multiplicities, which is in contrast to the height of the peak. It is also interesting to note that the peak appears to be symmetric with equal widths when observed from projections onto both the $\Delta\eta$ and the $\Delta\varphi$ axes.

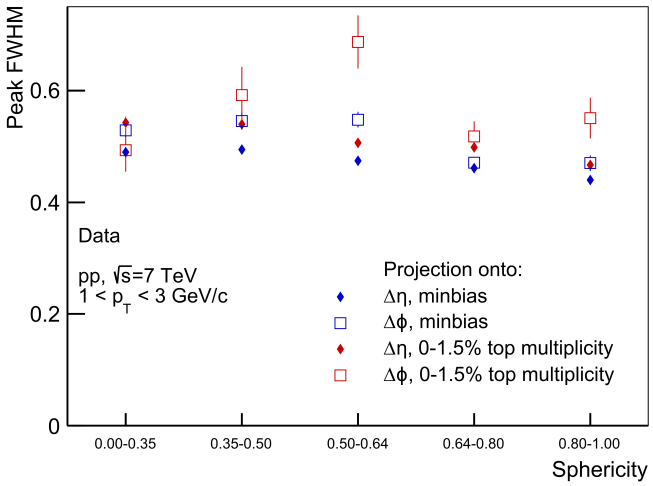

Figure 7.8: The width of the jet peak.

The final quantitative variable is the yield of the peak. The yield of the peak gives a measure of the proportion of particle pairs present in the peak and can be thought of as the volume under the peak of the correlation function. Reducing the peak yield directly reduces the background of the peak. Seeing as one of the dimensions of the peak decreases quasi-exponentially with increasing S_T (the height) and the other two dimensions remain flat (the widths in the $\Delta\eta$ and the $\Delta\varphi$ projections), one would expect that the yield also decreases quasi-exponentially in a similar manner as the height. This is indeed the case as can be seen in figure 7.9. The yield appears to decrease exponentially, by approximately

a factor of three from the lowest to the highest S_T events. The yield of the peak is also lower for the events with the highest of multiplicities than for the minimum bias events.

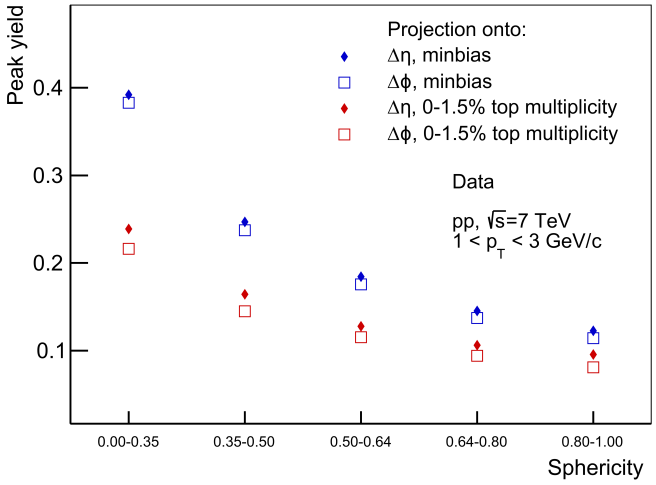

Figure 7.9: The yield of the jet peak.

Chapter 8

Uncertainties

In this section the uncertainties present in this thesis will be analysed. These uncertainties give us an indication of how far our measured quantities could be from their true value. The uncertainties come in two forms, random errors and systematic errors. Both of these errors are discussed in the following sections along with how they are estimated.

8.1 Random errors

Random errors are always present in any measurement and vary from one observation to another. This gives different results when repeating the same measurement. They originate from inherently unpredictable fluctuations in the measuring instruments and the measuring procedure.

This thesis is based on a counting experiment where the result is determined from the number of events in a particular bin. A good approximation for the random distribution of errors in such counting experiments is the Poisson distribution. In high energy physics, for such distributions it is common practice to take the variance of a bin in a histogram to be equal to the number of events in that bin and the standard deviation to be the square root of the variance. Therefore the error bars are plotted as $N_i \pm \sqrt{N_i}$ where N_i is the number of events in that bin. This leads to a relative error in each bin being $\frac{1}{\sqrt{N_i}}$.

In this thesis the errors are calculated in this way for only the 2 basic histograms: the signal and the background, from which the correlation function is calculated. All further errors are calculated by propagating these errors throughout the analysis, adding new errors as new possible sources appear (for example during the fitting procedure). The errors are propagated in the following ways: if the value of a variable is multiplied by a

constant, such as when normalizing a histogram, its relative error remains unchanged. If the values of multiple variables are added or subtracted, such as when projecting a 2D histogram onto 1D, the value of the square of the standard error of the new variable equals the sum of the squares of the standard errors in all of the variables added together. If the values of multiple variables are multiplied or divided, such as when dividing the signal by the background to obtain the correlation function, the value of the square of the relative error of the new variable equals the sum of the squares of the relative errors.

These errors are omitted from 2D plots for clarity but are shown on all 1D plots. In many cases these errors might seem to be absent, but they are simply smaller than the markers used on the plots.

8.2 Systematic errors

Systematic errors are errors that are not caused by random fluctuations but by an inaccuracy inherent to the measuring procedure. These errors do not get smaller by taking a larger number of measurements and averaging. They are usually constant or proportional to the actual value of the measurement.

8.2.1 Contributions to the systematic uncertainty

Certain systematic errors can be estimated by varying some aspect of the measuring or data taking procedure and observing how such a change influences the final result. In this section the variations taken into account in this thesis will be presented.

Dataset

The analysis was performed on one particular sample described in section 5.1. All the data in this sample was recorded under the same conditions with the same reconstruction procedure. To estimate the potential systematic error originating from choosing this particular dataset, the analysis was performed on a run from another dataset and compared. This new dataset was still taken with the same particle energies and the same detectors were used as for the original dataset used for this thesis. There were, however, some slightly different conditions and slight differences in the reconstruction procedure (a newer version of the reconstruction procedure). The differences in the correlation function projections

between the two data samples was less than 1% in most bins, increasing up to 1.7% in a few specific bins.

Track cuts

In the analysis, particles with a pseudorapidity of $|\eta| < 0.9$ and a transverse momentum of $p_T > 0.15$ GeV/c were included in the data sample. The effect of these track cuts on the systematic error are studied by varying them and observing the change in the correlation function.

The pseudorapidity range was varied by ± 0.1 i.e. the ranges of $|\eta| < 0.8$ and $|\eta| < 1.0$ were studied. The effect of these variations on the correlation function is less than 1% in all bins except for those on the very edges of the correlation function for the largest values of $\Delta\eta$. This is due to the fact that in order to obtain particle pairs contributing to the highest $\Delta\eta$ bins the particles have to come from the opposite edges of the η range. These particle combinations have the lowest statistics and thus the highest fluctuations. Increasing the $|\eta|$ acceptance increases the number of particle pairs available to create these high $\Delta\eta$ combinations. These edge errors do not play a significant role in this analysis since the bins of sufficiently high $\Delta\eta$ are already excluded due to too low statistics.

The minimum range of $p_T > 0.15$ GeV/c was also varied to $p_T > 0.25$ GeV/c. This did not influence the correlation function at all since only particles in the p_T range $1 < p_T < 3$ GeV/c were used to construct the correlation function and thus these cuts did not influence it at all. The variation could influence the apparent transverse sphericity of the events causing certain events to fall into different S_T classes. However, the variation of p_T turned out to cause a negligible change in the results.

Event level systematics

The effect of three event level factors was observed on the systematics of this analysis. These are the range of the z_{vtx} bins, the position of the edges of the S_T bins and the effect of the pile-up rejection procedure.

While calculating the background of the correlation function, the particles from one event have to be paired with particles of other events. The events are mixed with other events that occurred at similar z_{vtx} positions along the beam line (see chapter 6). In

this analysis, events were only mixed with other events if their z_{vtx} position was in the same 2 cm wide bin. To estimate the systematic error from this binning the results were compared to the case where no binning was used. The difference was less than 0.4% and was mainly present for small $\Delta\varphi$ values.

The error introduced by the choice of the S_T intervals was studied by narrowing the S_T intervals by 10% (5% on each side). The bins were centred around the same value. The difference was was less than 3% in all bins.

The effect of the pile-up rejection procedure was not studied in this work but was found to be negligible in similar analyses [79].

Fitting uncertainties

Systematic uncertainties can be introduced through the fitting procedure in two ways: the starting parameters for the fit and the fitting range. Changing the starting parameters of the fit by an order of magnitude causes no discernible differences in the final fit and therefore did not affect the results. Changing the range of the fit however does affect the result since it changes the shape of the Lorentzian slightly. In the analysis the fits were performed for $|\Delta\eta| \leq 1$ and $|\Delta\varphi| \leq 1$. These values were varied by ± 0.2. There was a varying difference depending on whether the fitting range was increased or decreased as well as whether the projection was onto the $\Delta\eta$ or the $\Delta\varphi$ axis. In the case of the projection onto the $\Delta\eta$ axis the variation was on the order of 3% for both cases of a larger and smaller fitting range and for both the height and the width of the fit.

In the case of the projection onto the $\Delta\varphi$ axis the variation in the height of the fit was of the order of 3% in the case of a smaller fitting range ($|\Delta\varphi| \leq 0.8$) and of the order of 4% in the case of a larger fitting range ($|\Delta\varphi| \leq 1.2$). The variation in the width of the fit was of the order of 5% in the case of a smaller fitting range ($|\Delta\varphi| \leq 0.8$) and of the order of 9% in the case of a larger fitting range ($|\Delta\varphi| \leq 1.2$). The Lorentzian fit on the $\Delta\eta$ projection is better and more resistant to fitting range changes since the Lorentzian shape extends far past the original fitting range. This differs from the case of the $\Delta\varphi$ projection where the Lorentzian shape ends suddenly, leaving way to a constant background (see figure 6.7 for an example of a Lorentzian fit).

8.2.2 Monte Carlo closure test

The Monte Carlo closure test is a procedure to estimate the errors introduced by our corrections procedure detailed in section 6.2. The data that we read out in our detector is not the truth of what happened in physics but a version that is folded through our detector characteristics. We attempt to unfold this measured data back to the physical truth using a certain correction procedure (see section 6.2.1). This procedure uses Monte Carlo generated data (PYTHIA) and a complex simulation of our detector (GEANT3) to determine a simple way of unfolding our data to obtain the truth. To determine the errors introduced into the analysis by this unfolding method the analysis is performed on the MC generated data, which represents the physical truth (MC truth). Then the analysis is performed on the same MC generated data after it has passed through our detector simulation and then subsequently unfolded by our correction procedure. This is a new version of the physical truth which should be as close as possible to the MC truth. In the case of the correlation function calculated using a $\sqrt{s} = 7$ TeV pp data sample generated using Pythia 6 with a Perugia0 tune and GEANT3, the difference was on the order of $0 - 0.5\%$ with the exception of the single bin located at $(0, 0)$ where the difference was 2%.

Chapter 9

Discussion

In this closing chapter an interpretation of the results will be given along with a discussion about their significance towards future research.

There are four aspects of the results which should be discussed. The first is the effect of transverse sphericity on the shape and size of the jet peak in the correlation function. As can be seen in section 7.2.1 of the results, the height and yield of the jet peak decreases in a quasi-exponential way with increasing S_T. The width, on the other hand, remains constant and independent of S_T. This indicates that choosing data samples containing events with higher transverse sphericities can reduce the fraction of events with jets in that sample by about a factor of three. However, the jets that remain have the same shape and distribution of particles within them, extending over the same solid angle. Therefore, S_T as a variable cannot be used to fully remove jets as a background nor can it reduce the angle at which the jets influence the sample. On the other hand, it can be used to reduce (or increase) the fraction of events containing jets in a data sample. This can be useful for certain analyses requiring the removal of jets or data samples with more jets if the S_T variable doesn't significantly influence the underlying variable that is being studied.

This brings us to the second point: as can be seen in figure 7.1, while studying the correlation function, the implementation of S_T does not only affect the jet peak but the entire underlying correlation structure. The transverse sphericity variable appears to "overpower" the structures of the correlation function causing the only structure present in all S_T cases to be the near-side jet peak. It is not the case, as was originally expected, that increasing the S_T of events would reduce only the jet peak leaving way for the underlying structures to be more visible. Quite the contrary, it appears that S_T has a larger effect on the underlying structures themselves. In retrospect this does make sense since the

correlation function depends exclusively on the angular distribution of particles within events i.e. the shape of the events and S_T is an event shape variable. Choosing events of certain transverse sphericities biases the possible shapes of the correlation function that can be made. It appears that S_T has a profound effect on the correlation function even though the definition of S_T appears natural and harmless (simply being defined as the ratio of the p_T projections on the two perpendicular axes with highest and lowest total projection of p_T) and has been used until now to determine the extent to which an event is "jet-like". Even though S_T is based on the momentum distribution in an event while the correlation function is based on the angular distribution of particles themselves, and S_T is calculated using all particles in an event while the correlation function is calculated using only particles with $1 < p_T < 3$ GeV/c, a bias is still introduced into the results. This is an important reminder that particularly in particle physics, but generally in all scientific research, care must be taken to ensure that our measurement procedure doesn't bias our results. In the case of the correlation function which looks at the shapes of events, other event shape variables should be avoided. This realisation has already had an effect in our collaboration where a study looking at the correlation function as a function of elliptic flow v_2 was halted in its infancy due to the fact that elliptic flow also depends heavily on the shape of the events. On the other hand, S_T has already been highly successful in studies that are not dependent on the event shape such as in femtoscopy [76].

While the introduction of a bias, such as observing the correlation function in S_T bins, should generally be avoided, it could also be the case that a physical significance is hidden in some of the structures of the correlation function. Further research would be needed to establish whether or not this is the case. One of these features is the presence of two long range ridge-like $\Delta\eta$ correlations present at $\Delta\varphi = \frac{\pi}{2}$ and $\Delta\varphi = \frac{3\pi}{2}$ in the case of high S_T seen in figure 7.1. These correlation structures are different from anything before seen in the correlation function. The question then arises: what physical mechanism, primarily present among events with high S_T, could cause such a long range $\Delta\eta$ correlation structure at $\Delta\varphi = \frac{\pi}{2}$ and $\Delta\varphi = \frac{3\pi}{2}$? The answer to this question is unfortunately: the cause is not a known or unknown physical mechanism but is mathematical in nature. To see why this is the case it is useful to think about these long range structures from the point of view of what the events actually look like. The structures are present if, while observing an event in the transverse plane, for a randomly chosen particle there is a higher probability that

other particles are produced at $\pi/2$. To find out which process favours particles being produced at $\pi/2$ relative to one another one must only look at the definition of transverse sphericity. More specifically, what does it mean for an event to have a high S_T? As can be seen in section 5.3.1, the S_T variable is constructed by finding the axis in the transverse plane which has the highest total p_T projection of all the particles in the event. This total p_T projection then divides the total p_T projection on the axis perpendicular to the main axis. If the projection on the main axis is much larger than the total projection onto the perpendicular axis we have a jet like event and if the perpendicular projections are similar we have a spherical event. The question then arises: what happens when we have events with very few particles? For an event with only 2 particles that happen to pass our cuts, the only way for it to have a high S_T is for those two particles to have similar p_T and to fly our at $\pi/2$ to one another. This can be generalized to events with a low number of particles higher than 2. The presence of an energetic pair of particles perpendicular to one another will increase the sphericity of the event as well as contribute to the perpendicular ridge. This is a mathematical phenomenon present even in simulations [82] and is a typical case of *"you get what you asked for"* meaning that constructing an experiment in a careless way to try and prove a certain phenomenon can lead to the "discovery" of said phenomenon even if it is not actually present. As expected, this perpendicular structure becomes less pronounced the higher the multiplicity of the events is.

The final aspect of this analysis which should be commented on is the fact that a structure appearing to be "The Ridge" from section 3.4 appears in an unexpected place. In the first three panels of figure 7.1 showing the correlation function in the three lowest transverse sphericities a structure resembling the ridge is clearly visible. This is seen more clearly in figure 7.3 which shows the highest η projections onto the $\Delta\varphi$ axis. This ridge is also present in purely simulated data, which is a problem since the physical mechanism behind the ridge is still not fully understood and therefore not present in PYTHIA 6 generated data. This means that the ridge can be obtained in a data sample that does not contain it by carefully selecting part of the data sample. The fact that the ridge can appear in places where it shouldn't doesn't pose a problem to this thesis where it is already established that a bias occurred. However, it could influence other research where the problem could creep in unexpectedly and remain undetected. Since the ridge was discovered in pp collisions and touted as a truly unexpected discovery from CERN, other

analyses have sprung up searching for and finding the ridge in various places. Hopefully none of these analyses made an inconspicuous cut using a variable similar to or correlated to transverse sphericity and unknowingly tainted their results. As always in science, great care must be taken in the future to prevent unknown biases and blemish otherwise factual results.

Chapter 10

Hrvatski produljeni sažetak

10.1 Uvod

Fizika elementarnih čestica eksperimentalno se provjerava sudaranjem čestica pri visokim energijama. Sve veće energije sudara omogućuju ispitivanje sve manjih i skrivenijih struktura svemira. Novi fenomeni koji nastaju u tim sudarima obično su izuzetno kratkotrajni, raspadajući se u druge čestice prije nego što imaju priliku doći u blizinu bilo kojeg detektora. Stoga se moraju proučavati čestice koje novi fenomen proizvede raspadom kako bi se nešto zaključilo o njemu. Dvočestične kutne korelacije koristan su alat za proučavanje mehanizama proizvodnje čestica promatranjem kutnih distribucija $(\Delta\eta, \Delta\varphi)$ između parova čestica u nekom događaju. Različite strukture u $\Delta\eta - \Delta\varphi$ prostoru nastanu različitim metodama produkcije čestica i interakcijama između njima kratko nakon proizvodnje. Ispitivanje ovih struktura može nam dati uvid u prirodu tih interakcija. Jedna od tih struktura grebenastog oblika naziva se "The Ridge", i zanimljiva je jer najbolje trenutno objašnjenje njenog nastanka je iz interakcija unutar kvark-gluonske plazme (QGP). Stoga, prisustvo te strukture može biti indikator stvaranja QGP-a u određenom sustavu. Problem u proučavanju te strukture je da je često zasjenjuju druge strukture u korelaciji.

U ovoj se disertaciji analiziraju dvočestične kutne korelacije proton-proton sudara pri $\sqrt{s} = 7$ TeV koristeći transverzalni sfericitet i multiplicitet događaja za izoliranje i proučavanje različitih struktura u korelacijskoj funkciji. Transverzalni sfericitet je varijabla oblika događaja u prostoru količine gibanja koja mjeri koliko se izotropno čestice distribuiraju unutar događaja. Ova varijabla omogućava razlikovanje događaja koji sadrže mlazove čestica proizvedene u tvrdim procesima od događaje koji sadrže više mekih, neperturbativnih kvantno-kromodinamičnih (QCD) procesa.

10.2 Kvarkovsko-Gluonska plazma i sudari teških iona

Kvarkovsko-Gluonska plazma je stanje materije u kojoj su elementarne čestice od kojih su sastavljeni hadroni i koje nose jaku nuklearnu silu (kvarkovi i gluoni) naizgled oslobođene međusobnog jakog privlačenja. To se stanje materije formira pri ekstremnim energijama i gustoćama. Smatra se da su takvi uvjeti prožimali rani Svemir do nekoliko milisekundi nakon Velikog praska, a trenutno postoje u centrima neutronskih zvijezda. Ovi se uvjeti također mogu stvoriti u laboratoriju koristeći ultra-relativističke sudare teških iona.

Standardni model (SM) je teorija koja klasificira sve poznate elementarne čestice i opisuje tri od četiri poznate temeljne interakcije između čestica. Opisane temeljne sile su elektromagnetska sila, slaba i jaka sila koje se, prema standardnom modelu, prenose drugim česticama.

Dio SM koji se odnosi na jaku silu naziva se kvantna kromodinamika (QCD). QCD je kvantna teorija polja koja opisuje jaku silu među kvarkovima i gluonima. Snaga jake sile je dana konstantom vezanja QCD, α_s, koja uopće nije konstanta, već je funkcija količine gibanja koja se prenosi interakcijom:

$$\alpha_s(Q^2) \propto \frac{1}{\ln(Q^2/\Lambda^2_{QCD})}, \tag{10.2.1}$$

pri čemu je Q^2 preneseni četveromoment u interakciji, a Λ_{QCD} neki konstantni parametar[11]. Udaljenost među kvarkovima je dana s $\lambda\!\!\!^{-} = \frac{\hbar}{\sqrt{Q^2}}$. Stoga se pri vrlo malim udaljenostima i visokoj vrijednosti Q^2 konstanta vezanja α_s smanjuje i nestaje asimptotski. Ova ovisnost konstante spajanja manifestira se preko dva poznata svojstva obojenih čestica (kvarkova i gluona):

- **Zatočenje bojom** - svojstvo je koje kaže da jedan naboj boje ne može sam postojati.
- **Asimptotska sloboda** - opisuje smanjenje snage jake sile s porastom energije interakcije. U slučajevima kad je prijenos momenta (Q^2) visok, poput kratkih udaljenosti ili visokih temperatura, partoni se ponašaju slobodno.

Koncept asimptotske slobode je doveo do hipoteze da stanje materije nazvano Kvarkovsko-gluonska plazma može postojati pod određenim uvjetima. Pod tim uvjetima, jaka sila koja djeluje na partone postaje dovoljno slaba da bi se partoni ponašali kao slabo vezani partonski plin, umjesto organizirani u diskretne hadrone. Vjeruje se da su uvjeti u ranom Svemiru bili takvi da je cijeli Svemir bio u stanju QGP. Stoga proučavanje QGP-a dalo bi vrijedan uvid u fiziku koja upravlja nekim od najranijih trenutaka svemira.

Potpisi QGP

QGP koji nastaje u sudarima teških iona vrlo brzo se širi i hladi, trajući samo $\approx 10^{-23}$ sekunde, što znači da se ne stigne pomaknuti iz točke sudara i ući u naše detektore. Stoga možemo promatrati samo čestice koje nastaju kao rezultat hadronizacije QGP-a. Različita svojstva tih čestica, kao što su vrste čestica, broj čestica, njihove energije i smjerovi u kojima lete mogu se koristiti kao pokazatelji prisutnosti QGP-a. Ta svojstva nam čak omogućavaju proučavanje nekih svojstava QGP-a. Neki izmjereni, a neki samo teorijski potpisi QGP-a su: direktni fotoni, potisnuće mlazova, J/Ψ potisnuće, povećanje stranosti itd. Jedan od tih potpisa koji je najbitniji za ovaj rad je grebenasta struktura u dvočestičnim korelacijama koja je detaljnije opisana u idućem poglavlju.

Sudari teških iona

Najkorisnije sredstvo za proučavanje jake nuklearne sile i QGP su ultra-relativistički sudari teških iona. Oni su ujedno i jedini poznati eksperimentalno ostvariv način proučavanja QGP.

Eksperimentalni postav

LHC (veliki hadronski sudarač) i ALICE (A Large Ion Collider Experiment) su akcelerator/sudarač čestica i detektor koji se koriste za stvaranje i mjerenje podataka korištenih u ovoj disertaciji.

10.3 Dvočestične kutne korelacije

Dvočestične kutne korelacije koristan su alat za proučavanje mehanizama proizvodnje čestica, dinamike procesa sudaranja i svojstava proizvedenog medija.

Korelacije u ovom radu definirane su preko azimutalnog kuta φ i pseudorapiditeta η.

Korelacijska funcija

Korelacijska funcija $C(\Delta\eta, \Delta\varphi)$ daje mjeru međusobne kutne raspodjele čestica. Računa se na temelju razlike u η i φ među parovima čestica u nekom događaju. Jednostavna raspodjela ovih razlika unutar jednog događaja može se definirati na sljedeći način:

$$S(\Delta\eta, \Delta\varphi) = \frac{\mathrm{d}^2 N_{\mathrm{pairs}}^{\mathrm{signal}}}{\mathrm{d}\Delta\eta \mathrm{d}\Delta\varphi}. \tag{10.3.1}$$

Svaka pojedina čestica uspoređuje se sa svakom drugom česticom, a razlika njihovih η i φ računa se i dodaje u distribuciju. To daje informaciju o distribuciji čestica u događaju ili točnije, za određenu česticu, kolika je vjerojatnost da ćemo u nekom dijelu $\Delta\eta - \Delta\varphi$ faznog prostora pronaći drugu česticu. Na primjer, vrh oko $\Delta\eta = 0$ i $\Delta\varphi = 0$ bi nam ukazao da čestice putuju zajedno u istom smjeru.

Ova raspodjela uključuje fizikalne korelacije dviju čestica koje su nam zanimljive, međutim uključuje i trivijalne dvočestične korelacije i korelacije zbog nesavršenosti detektora i raspodjele pojedinih čestica. Kako bi se izbjegla pozadina ovih trivijalnih korelacija koje maskiraju stvarne fizikalne korelacije, stvaramo drugu korelacijsku raspodjelu na sljedeći način:

$$B(\Delta\eta, \Delta\varphi) = \frac{\mathrm{d}^2 N_{\mathrm{pairs}}^{\mathrm{mixed}}}{\mathrm{d}\Delta\eta \mathrm{d}\Delta\varphi}. \tag{10.3.2}$$

Ova distribucija uzima parove čestica iz različitih događaja. Budući da obje ove skupine i dalje potječu iz istog fizikalnog sustava i mjere se istim detektorom, raspodjela $B(\Delta\eta, \Delta\varphi)$ i dalje će uključivati trivijalne korelacije zbog nesavršenosti detektora i bilo kakve raspodjele pojedinih čestica. Međutim, neće sadržavati informaciju o bilo kakvim fizikalnim korelacijama među dvije čestice, jer čestice potječu iz zasebnih događaja i ne postoji način da one međudjeluju.

Korelacijska funkcija $C(\Delta\eta, \Delta\varphi)$ konstruira se dijeljenjem distribucije $S(\Delta\eta, \Delta\varphi)$, koja se naziva distribucija signala, $B(\Delta\eta, \Delta\varphi)$ distribucijom, koja se naziva pozadinom. Prije podjele raspodjele se normiraju:

$$C(\Delta\eta, \Delta\varphi) = \frac{\frac{1}{N_{\text{pairs}}^{\text{signal}}} S(\Delta\eta, \Delta\varphi)}{\frac{1}{N_{\text{pairs}}^{\text{mixed}}} B(\Delta\eta, \Delta\varphi)}. \tag{10.3.3}$$

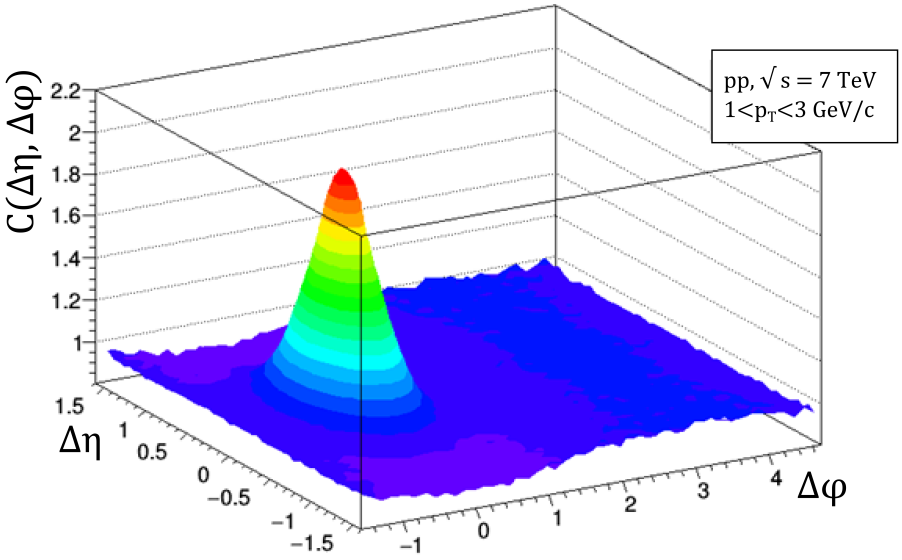

Slika 10.1: Tipični primjer korelacijske funkcije $C(\Delta\eta, \Delta\varphi)$.

Praktična implementacija korelacijske funkcije

Zbog nesavršenosti našeg detektora i grešaka pri sakupljanju podataka, podaci mjereni u eksperimentu nisu savršena reprezentacija čestica koje se stvarno stvaraju u sudaru. Stoga se izmjerena korelacijska funkcija definira malo drugačije od one opisane u predhodnom odjeljku. Postupak koji se koristi za ekstrapolaciju onoga što se vidi u detektoru na ono što se stvarno fizikalno događa impementira se računanjem i primjenom korekcijskog faktora f.

Korekcijski faktor f se primjenjuje za svaki par čestica, uzimajući u obzir vjerojatnost da vidimo te dvije čestice koje izlaze pod tim kutom ako pretpostavimo da su u stvarnosti te čestice proizvedene. Ispravljena korelacijska funkcija izračunata iz podataka može se

definirati pomoću ispravljenog signala $S_C(\Delta\eta, \Delta\varphi)$ i ispravljene pozadine $B_C(\Delta\eta, \Delta\varphi)$ na isti način kao u jednadžbi 10.3.3:

$$C(\Delta\eta, \Delta\varphi) = \frac{\frac{1}{N_{pairs}^{signal}} S_C(\Delta\eta, \Delta\varphi)}{\frac{1}{B_C(0,0)} B_C(\Delta\eta, \Delta\varphi)}. \tag{10.3.4}$$

Ispravljena distribucija signala i pozadine izračunava se na sljedeći način:

$$S_C(\Delta\eta, \Delta\varphi) = \sum_{p_{T,1}, p_{T,2}} f(p_{T,1}, p_{T,2}) S(\Delta\eta, \Delta\varphi, p_{T,1}, p_{T,2}), \tag{10.3.5}$$

$$B_C(\Delta\eta, \Delta\varphi) = \sum_{p_{T,1}, p_{T,2}} f(p_{T,1}, p_{T,2}) B(\Delta\eta, \Delta\varphi, p_{T,1}, p_{T,2}). \tag{10.3.6}$$

Kako bi se izračunao korekcijski faktor f potrebna su dva skupa Monte Carlo (MC) generiranih događaja. Prvi skup generira se izravno iz MC simulacije na temelju ulaznih parametara koji odgovaraju primarnim specifikacijama sudara LHC (tip čestica, energija sudara). Drugi skup podataka, koji se naziva rekonstruirani MC, sadržava podatke o tome koje čestice zapravo detektiraju naši detektori. Ovaj se set dobiva simuliranjem transporta čestica kroz različite materijale koji sačinjavaju detektor.

Ono što se dobije na ovaj način je skup podataka koji zrcali naš stvarni izmjereni skup podataka. Međutim, nasuprot izmjerenim podacima, za ovaj skup imamo podatke o stvarnim "fizikalnim" događajima od kojih su proizvedeni. Usporedba ova dva simulirana skupa podataka omogućava nam određivanje utjecaja detektora i procedure mjerenja na same podatke, te izračun korekcijskog faktora f. Taj faktor se zatim može primijeniti na stvarne izmjerene podatke da bi se dobilo ono što se stvarno fizikalno događa. Ovaj korekcijski faktor nije samo jedan broj, već je tenzor, jer efikasnost našeg detektora nije homogena, nego ovisi o različitim parametrima.

Strukture u korelacijskoj funkciji

Korelacijska funkcija nam daje cjelovitu sliku svih korelacija prisutnih u našem sustavu. Ova ukupna korelacija sastoji se od mnogo različitih preklapajućih izvora. Svaki od ovih izvora korelira čestice na različite načine, stvarajući različite strukture u korelacijskoj funkciji. Ti izvori uključuju zakone očuvanja, mlazove i mini-mlazove, Bose-Einsteinove

korelacije, rezonancije, pretvorbu fotona, gluonske strune, Coulomb-ove interakcije, flow, grebenastu strukturu itd.

Mlazovi

Najdominantnija struktura u korelacijskoj funkciji dolazi od mlazova. Zaslužni su za glavni vrh oko (0,0) i grebenastu strukturu oko $\Delta\varphi = \pi$. Mlazovi nastaju hadronizacijom partona koji je sudarom izbačen iz hadrona. Zbog početne brzine partona, sve čestice u mlazu izlete u istom smjeru. Ova dominantna struktura često zasjenjuje druge slabije strukture (kao npr. u ovom radu) i nekad bi ju bilo korisno ukloniti.

The Ridge

Grebenasta struktura koja je nazvana "The Ridge" je korelacijska struktura koja se nalazi oko $\Delta\varphi = 0$ i proteže se u širokom rasponu $\Delta\eta$. Još uvijek se teorijski raspravlja podrijetlo tog grebena. Obično se pripisuje interakcijama između QGP i mlazova, te kolektivnog gibanja u QGP [35].

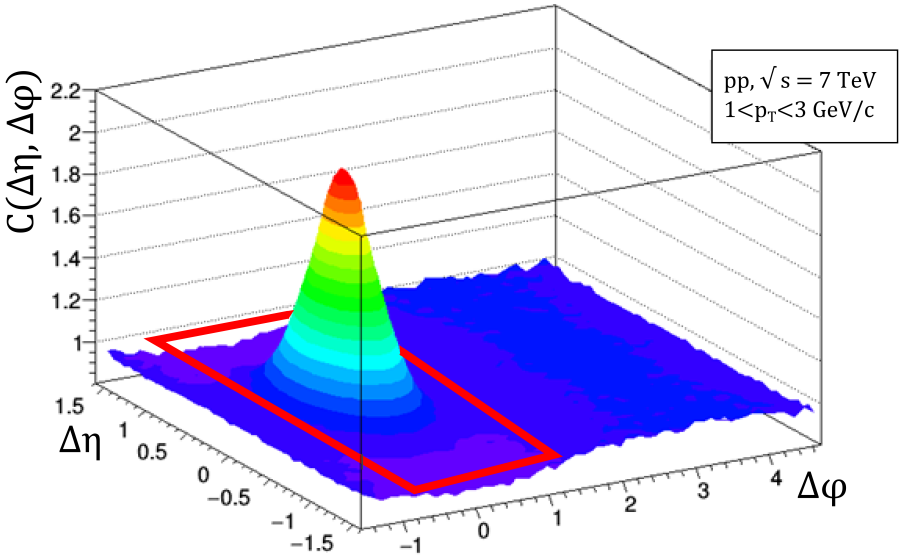

Slika 10.2: Doprinos Ridge-a korelacijskoj funkciji $C(\Delta\eta, \Delta\varphi)$ (označeno crvenom bojom).

Ridge se očituje u korelacijskoj funkciji kao grebenasta struktura otprilike konstantne visine, centrirana oko $\Delta\phi = 0$ koja se prostire u širokom rasponu $\Delta\eta$. Ridge u sudarima te-

ških iona najčešće se pripisuje korelacijama unutar QGP-a. Najčešća objašnjenja uključuju neku vrstu hidrodinamičkog toka, koji opisuje evoluciju QGP nakon formiranja [40, 41]. Stoga bi se prisustvo Ridge-a teoretski moglo upotrijebiti kao indikator za prisustvo QGP u nekom skupu podataka. Ovo se razlikuje od drugih metoda koje uspoređuju neku pojavu u sudarima teških iona s onima iz manjih sustava (uglavnom pp, ali i p-A). Ti se manji sustavi koriste za usporedbu jer se smatraju premalim za nastajanje QGP-a, tj. da nema dovoljno vremena da se dogodi termalizacija, tako da se u njima sve čestice proizvode u teškim procesima.

Stoga je bilo veliko iznenađenje kad je CMS kolaboracija najavila otkriće korelacije koja odgovara Ridgeu u pp sudarima. Kao što je već spomenuto, na temelju našeg trenutnog razumijevanja pp sudara, ne formira se QGP. Otkriće Ridge-a u tim sudarima bi moglo ukazivati na neku novu fiziku. To otkriće je motivacija ovog doktorskog istraživanja, naime cilj je proučiti strukture korelacijske funkcije i pokušati izolirati Ridge strukturu od pozadinskih mlazova.

10.4 Uzorak podataka

Podaci korišteni u ovom radu dobiveni su od sudara proton-proton (pp) zabilježenih 2010. godine. Događaji su izmjereni u sudarima s energijom centra mase od $\sqrt{s} = 7$ TeV. Ukupni broj dobrih događaja koji su prošli sve kriterije odabira događaja je $33 \cdot 10^6$. Odgovarajući podaci su generirani Monte Carlo (MC) generatorom. Te MC simulacije izvedene su s postavkama koje odgovaraju postavkama LHC sudarivača i ALICE detektora u vrijeme stvarnog uzimanja podataka. Pythia 6 korištena je za generiranje događaja, a GEANT3 za simulaciju odgovora detektora.

10.5 Analiza oblika događaja

Multiplicitet (broj proizvedenih čestica) je jedna od glavnih opservabli koja se koristi za razlikovanje sudara čestica visokih energija. Međutim, kao opservabla, nije osobito osjetljiva na osnovne fizikalne mehanizme koji su zaslužni za stvaranje čestica u nekom događaju. Hadronizacija jednog visoko-energetskog partona u mlaz može rezultirati događajem velikog multipliciteta. S druge strane, sudar koji sadrži mnogo "mekih" sudara niskih energija (npr. u QGP) također može stvoriti događaj velikog multipliciteta. Za

razlikovanje takvih događaja može biti korisna analiza oblika događaja. Događaji s tvrdim raspršenjem jednog partona su u perturbativnom režimu QCD-a i imaju tendenciju stvarati mlazove što rezultira vrlo anizotropnim događajima s kolimiranim snopovima čestica. Suprotno tome, više mekih interakcija koje karakteriziraju neperturbativnu QCD proizvodnju čestica, imaju tendenciju stvoriti više izotropno raspoređene događaje. U tim događajima su čestice i njihove količine gibanja ravnomjernije raspoređene po svim kutovima. Varijabla koja bi opisala oblik konačnog stanja trebala bi biti učinkovitija u razlikovanju događaja s tim različitim vrstama temeljnih procesa.

10.5.1 Transverzalni sfericitet

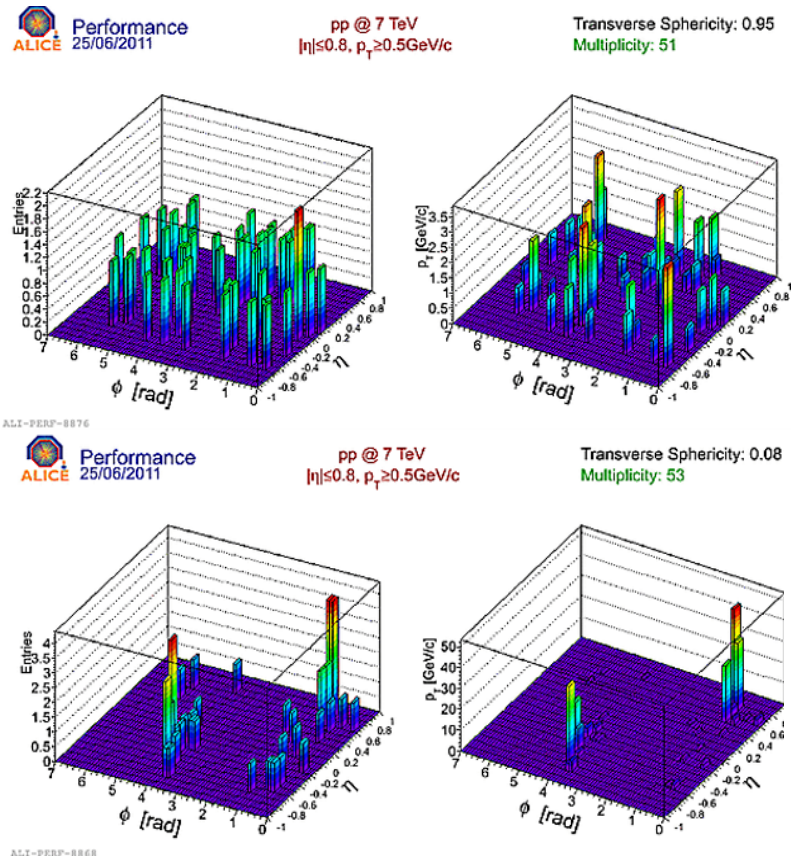

Slika 10.3: Usporedba raspodjele čestica i količina gibanja unutar dva događaja sa sličnim brojem čestica. Događaji imaju drastično različit oblik i S_T [76].

Transverzalni sfericitet (S_T) je varijabla oblika događaja u prostoru količine gibanja. Opisuje koliko su izotropno raspoređene putanje čestica i njihove količine gibanja u nekom događaju. Varijabla je skalar izračunat korištenjem svojstvenih vrijednosti matrice

transverzalne količine gibanja S_{XY}:

$$S_{XY} = \frac{1}{\sum_i p_{T\,i}} \sum_i \frac{1}{p_{T\,i}} \begin{pmatrix} p_{x\,i}^2 & p_{x\,i} p_{y\,i} \\ p_{x\,i} p_{y\,i} & p_{y\,i}^2 \end{pmatrix}. \tag{10.5.1}$$

Matrica transverzalne količine gibanja definirana je korištenjem transverzalne količine gibanja svih primarnih nabijenih čestica u događaju. Razmatraju se samo transverzalne količine gibanja kako bi se izbjegla pristranost od Lorentzovog boost-a duž osi snopa. Vlastite vrijednosti matrice transverzalne količine gibanja λ_1 i λ_2 ($\lambda_1 \leq \lambda_2$) osjetljive su na razlike u ukupnoj količini gibanja u transverzalnoj ravnini. To omogućava da se tranzverzalni sfericitet definira kao:

$$S_T = \frac{2\lambda_1}{\lambda_1 + \lambda_2}. \tag{10.5.2}$$

Definiran na ovaj način, S_T je skalar koji može imati vrijednosti u rasponu od 0 do 1. S_T je približno 0 za događaje u kojima je većina transverzalne količine gibanja usmjerena duž jedne osi. S_T je približno 1 za događaje u kojima je projekcija transverzalne količine gibanja na os s najvećom projekcijom jednaka projekciji na os koja joj je okomita.

10.6 Rezultati

U ovom su odjeljku prikazani rezultati promatranja dvočestične kutne korelacijske funkcije u ovisnosti o obliku događaja. Zavisnost korelacijske funkcije o S_T proučava se za sve događaje i za događaje s najvećim multiplicitetom. Rezultati se zatim uspoređuju korištenjem projekcija korelacijske funkcije na različite osi. Konačno se širina i visina vrha mlazova kvantificiraju ovisno o S_T-u.

Ovisnost korelacijske funkcije $\Delta\eta - \Delta\varphi$ o S_T prikazana je na slici 10.4. Događaji su podijeljeni u pet klasa S_T.

Na slikama se vidi drastična promjena oblika korelacijske funkcije u ovisnosti o S_T. Najočitija karakteristika korelacijske funkcije koja se jasno vidi u svim slučajevima S_T je jasan vrh na $(0, 0)$ koji potječe od mlazova. Ovaj vrh je posebno izražen za slučajeve malih S_T, što odgovara događajima u kojima očekujemo više mlazova. Čini se da se taj vrh postupno smanjuje u svim dimenzijama kako se S_T događaja povećava.

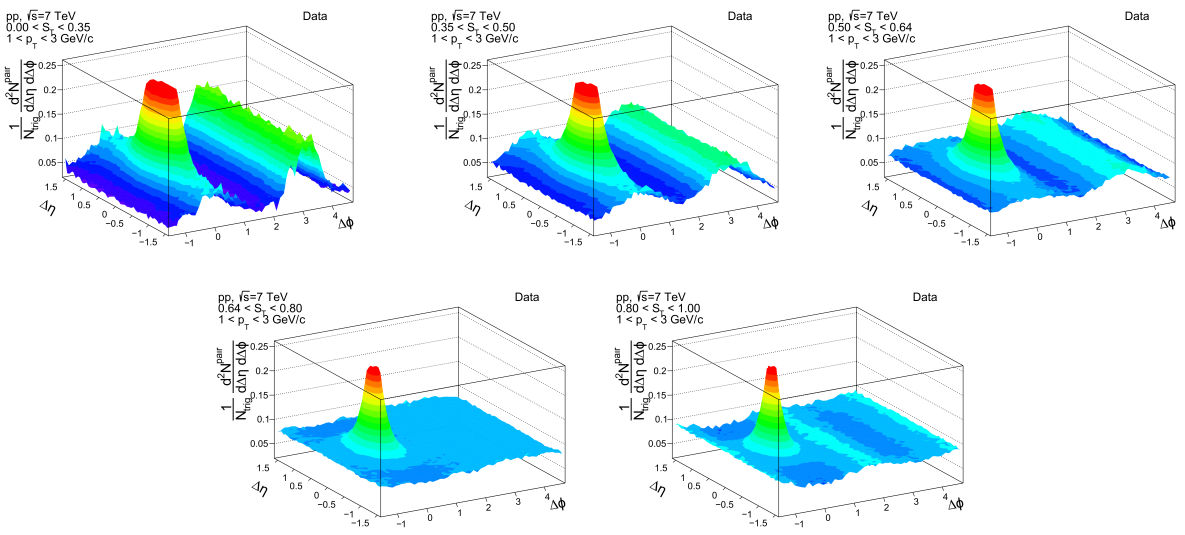

Slika 10.4: $\Delta\eta - \Delta\varphi$ korelacijska funkcija u ovisnosti o S_T za minimalno pristrane događaje.

Druga značajna karakteristika je greben na daljoj strani, koji se manifestira kroz korelaciju koja se proteže kroz čitav raspon $\Delta\eta$ i koji se nalazi na $\Delta\varphi = \pi$. Slično kao i kod vrha na $(0, 0)$, udaljeni greben je naročito izražen u slučajevima malih S_T i smanjuje se kako se povećava S_T. Za razliku od vrha na $(0, 0)$, udaljeni greben ne ostaje prisutan u svim S_T klasama, nego prividno nestaje, i pri najvišim vrijednostima S_T se čak invertira i postaje dolina.

Ove dvije značajke korelacijske funkcije ukazaju na smanjenje udjela mlazova u uzorku s povećanjem S_T, ali bi također mogle ukazivati na prisutnost drugih nepoznatih pojava o kojima će se raspravljati u odjeljku Rasprava i zaključak.

Još jedna iznenađujuća značajka ovih korelacijskih funkcija je to što se pojavljuje grebenasta struktura koja izgleda kao poznati "Ridge" u događajima s niskim S_T. To je korelacijska struktura koja se proteže u velikom rasponu $\Delta\eta$ i koja se nalazi na $\Delta\varphi = 0$. Ovaj se greben može vidjeti kako strši iz vrha pri $(0, 0)$ pri događajima s nižim S_T-om, opada prema srednjim S_T-ima prije nego što nestane i preokrene se pri najvišim vrijednostima S_T-a.

Konačno, uočljive strukture mogu se vidjeti u slučaju od $0,8 < S_T < 1,0$ što odgovara najsferičnijim događajima. Te se strukture protežu u cijelom rasponu $\Delta\eta$ i nalaze se na $\Delta\varphi = \frac{\pi}{2}$ i $\Delta\varphi = \frac{3\pi}{2}$.

Projekcije

Da bi se na smisleniji način usporedile razlike u strukturama između različitih vrijednosti S_T, mogu se napraviti projekcije na osi korelacija. Ove projekcije pojašnjavaju određene aspekte grafova, i također omogućuju bolju usporedbu među slučajevima jer se podaci s različitim vrijednostima S_T mogu prikazati na istim osima. To se može vidjeti na slici 10.5.

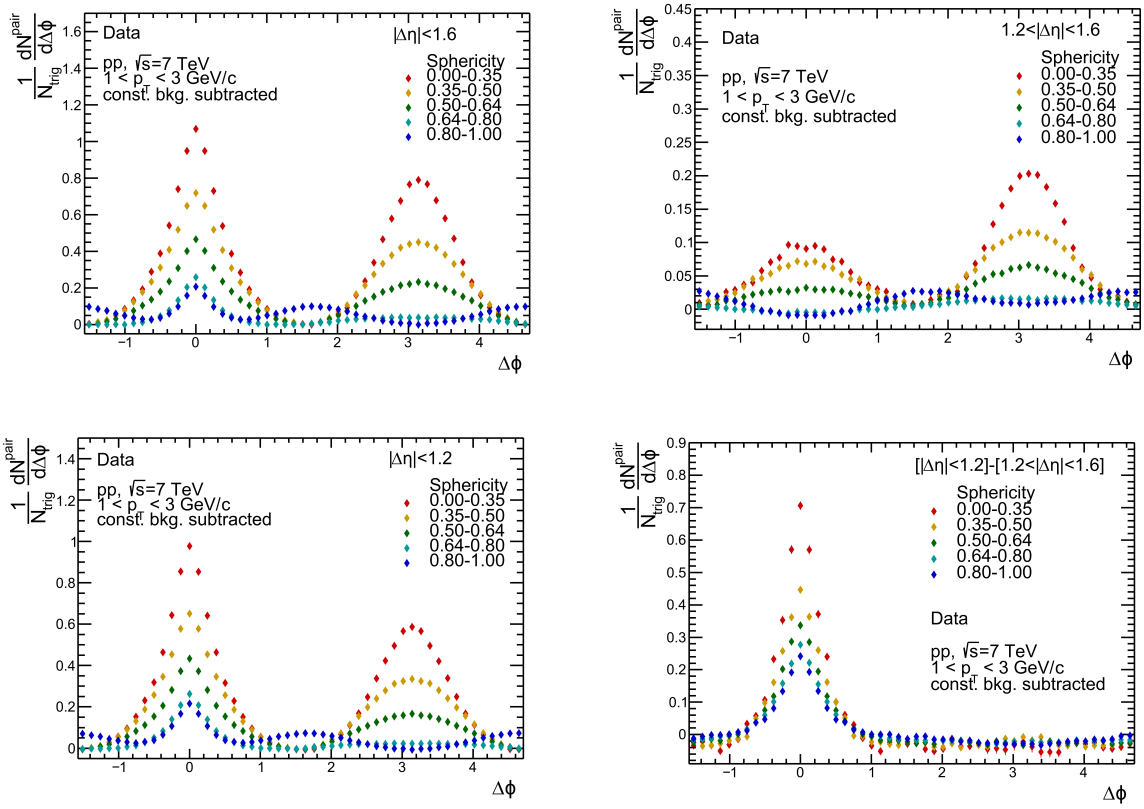

Slika 10.5: Projekcije različitih podskupova $\Delta\eta - \Delta\varphi$ korelacijske funkcije na $\Delta\varphi$ i na $\Delta\eta$ osi u pet klasa S_T.

Karakteristike vrha na $(0, 0)$

Utjecaj S_T-a na oblik i veličinu vrha na $(0, 0)$ može se kvantificirati pomoću prilagođavanja neke funkcije na projekciju vrha na $(0, 0)$. Tri mjerljive opservable koje opisuju vrh se mogu zatim izvući iz te funkcije; visina vrha, širina vrha i udio čestica koje pripadaju vrhu. Te tri varijable se promatraju i uspoređuju za projekcije na osi $\Delta\eta$ i $\Delta\varphi$, kao i za događaje sa svim multiplicitetima i one u $1,5\%$ najvećih multipliciteta.

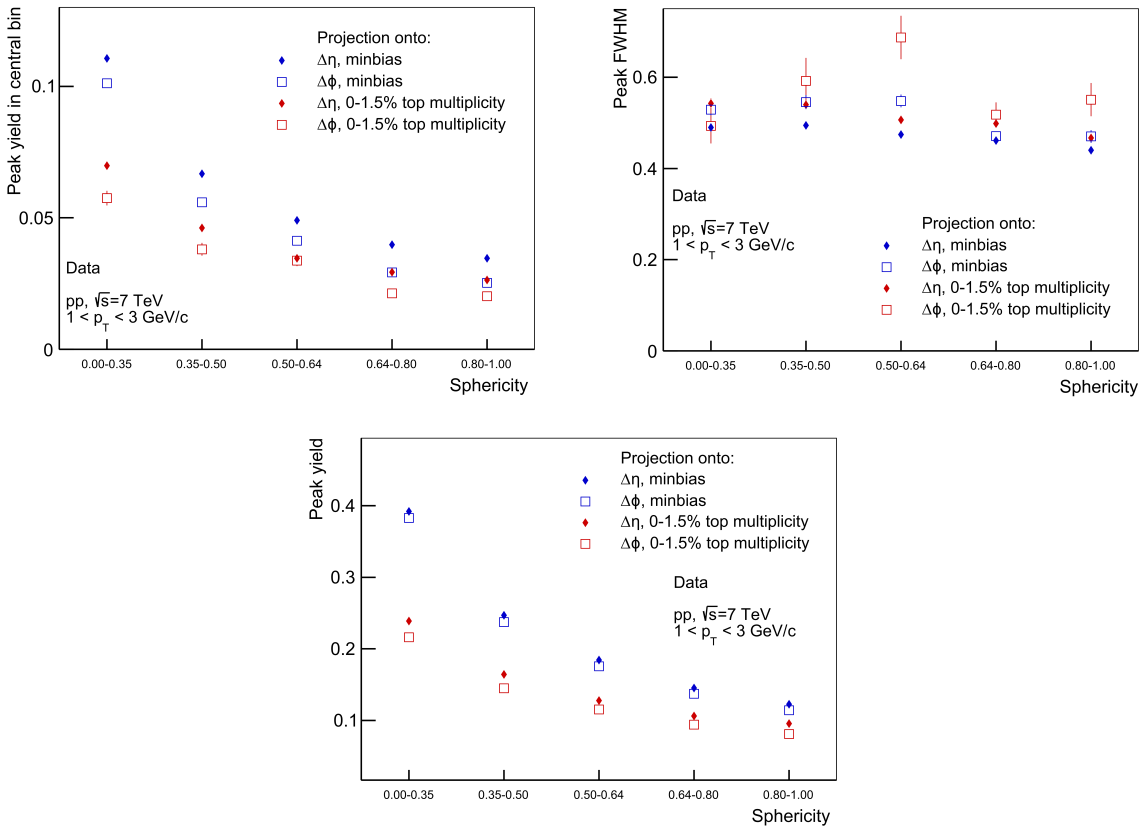

Slika 10.6: Visina i širina vrha od mlazova te udio čestica u vrhu.

Visina vrha i udio čestica u vrhu padaju eksponencijalno s porastom S_T što ukazuje na to da se povećanjem S_T-a smanjuje broj događaja u kojima postoje mlazovi. Širina vrha ostaje nepromijenjena što ukazuje na to da mlazovi koji preostaju imaju nepromijenjeni oblik.

10.7 Rasprava i zaključak

U ovom su radu istraženi oblik i veličina nekih struktura dvočestične korelacijske funkcije u ovisnosti o transverzalnom sfericitetu i multiplicitetu za pp sudare pri $\sqrt{s} = 7$ TeV.

Postoje četiri značajna aspekta rezultata koje treba spomenuti. Prvi je utjecaj S_T-a na oblik i veličinu vrha na $(0, 0)$ u korelacijskoj funkciji. Visina i udio čestica u vrhu smanjuju se gotovo eksponencijalno povećanjem S_T-a. S druge strane, širina ostaje konstantna i neovisna o S_T-u. To ukazuje na to da se odabirom uzorka podataka koji sadrže događaje s višim S_T-om može smanjiti udio događaja s mlazovima u tom uzorku i to za otprilike

faktor tri. Međutim, preostali mlazovi imaju isti oblik i raspodjelu čestica unutar njih, koji se protežu pod istim prostornim kutom. Stoga se S_T kao varijabla ne može upotrijebiti za potpuno uklanjanje mlazova iz uzorka niti može smanjiti kut pod kojim mlazovi utječu na uzorak. S druge strane, S_T se može koristiti za smanjenje (ili povećanje) udjela događaja koji sadrže mlazove u uzorku podataka.

Drugi bitni aspekt rezultata, koji se može vidjeti na slici 10.4, jest da implementacija S_T reza na podatke ne utječe samo na vrh na $(0, 0)$, već na cjelokupnu strukturu korelacije. Čini se da je varijabla S_T "nadjačala" ostale strukture korelacijske funkcije. Jedina struktura prisutna u svim klasama S_T je vrh na $(0, 0)$. Nije slučaj, kao što se prvobitno očekivalo, da bi povećavanje S_T-a smanjilo samo vrh na $(0, 0)$, ostavljajući ostale temeljne strukture da budu vidljivije. Sasvim suprotno, čini se da S_T ima veći učinak na same temeljne strukture. Ovo je važan podsjetnik da posebno u fizici čestica, ali općenito u svim znanstvenim istraživanjima, treba paziti da naš postupak mjerenja ne čini naše rezultate pristranim.

Dok u pravilu treba izbjegavati uvođenje pristranosti, kao što je promatranje korelacijske funkcije u S_T klasama, može se dogoditi i da je u nekim strukturama korelacijske funkcije skriven neki fizikalni značaj. Potrebna bi bila daljnja istraživanja kako bi se utvrdilo je li to slučaj.

Jedna od tih značajki je prisutnost dva dugodosežna grebena u $\Delta\eta$ prisutnih na $\Delta\varphi = \frac{\pi}{2}$ i $\Delta\varphi = \frac{3\pi}{2}$ u slučaju visokog S_T-a što se vidi na slici 10.4. Te korelacijske strukture razlikuju se od bilo čega što je do sad viđeno u korelacijskoj funkciji. Zatim se može postaviti pitanje: koji bi fizikalni mehanizam, prvenstveno prisutan u događajima s visokim S_T, mogao stvarati takvu korelacijsku strukturu? Na ovo je pitanje odgovor nažalost: uzrok nije fizikalni mehanizam, nego je matematičke prirode. Ispada, iz definicije S_T, da događaj može imati visoki S_T ako sadrži mali broj čestica koje lete u okomitim smjerovima. Takvi događaji također doprinose ovim novim grebenastim strukturama. To znači da smo odabirom varijable S_T uveli pristranost u korelacijsku funkciju dok promatramo događaje s visokim S_T. Ovaj je matematički fenomen prisutan čak i u simulacijama [82] i ilustrira da konstruiranje eksperimenta na neoprezan način s ciljom kako bi se dokazao određeni fenomen može dovesti do "otkrića" navedenog fenomena čak i ako on zapravo nije prisutan.

Završni aspekt ove analize koji bi se trebao komentirati je činjenica da se struktura koja izgleda kao "The Ridge" pojavljuje na neočekivanom mjestu. Na prva tri grafa na

slici 10.4 koje prikazuju korelacijsku funkciju u tri najniža S_T-a jasno je vidljiva struktura koja liči na taj greben. Ovaj greben je također prisutan u čisto simuliranim podacima, što predstavlja problem jer fizikalni mehanizam koji stvara taj greben u pp sudarima još uvijek nije u potpunosti dojašnjen i zbog toga nije prisutan u podacima proizvedenim u PYTHIA 6. To znači da se greben može dobiti u uzorku podataka koji ga ne sadrži pažljivim odabirom uzorka podataka. Budući da je Ridge otkriven u pp sudarima i oglašen kao zaista neočekivano otkriće CERN-a, pojavila su se razna druga istraživanja koja su tražila i pronalazila Ridge na raznim mjestima. Moguće je da je neka od ovih analiza napravila nepromišljeni rez na podatke korištenjem neke varijable slične S_T ili korelirane s S_T i nesvjesno učinila svoje rezultate pristranim. Trebala bi se izvršiti daljnja istraživanja koja bi proučavala i provjerila prijašnje rezultate.

Appendix A

Additional plots

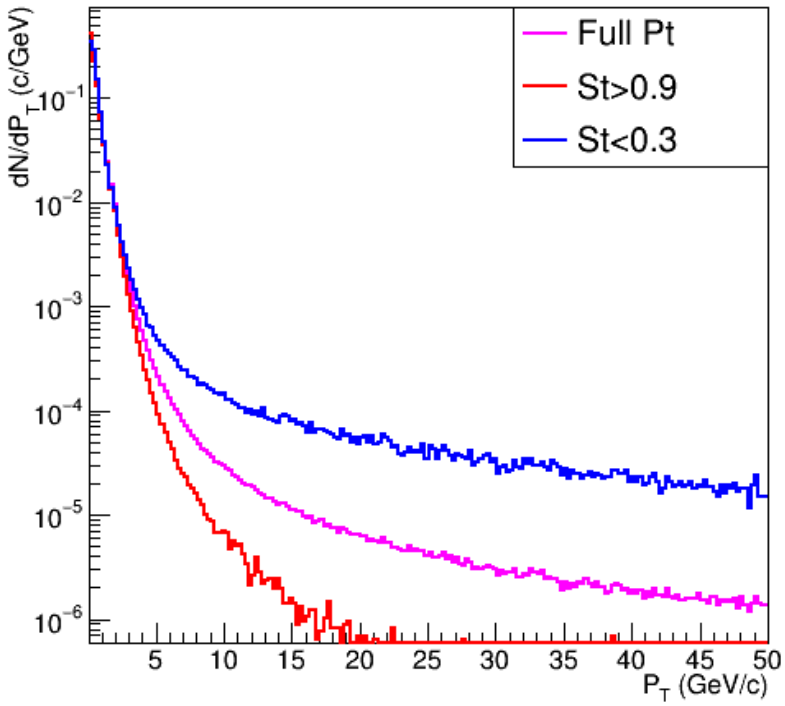

Figure A.1: Normalized p_T spectra in three different S_T classes. It is visible that events with a lower S_T contain a larger proportion of high p_T particles, indicating a higher proportion of hard jet-like events. The opposite is true for events with high S_T [83].

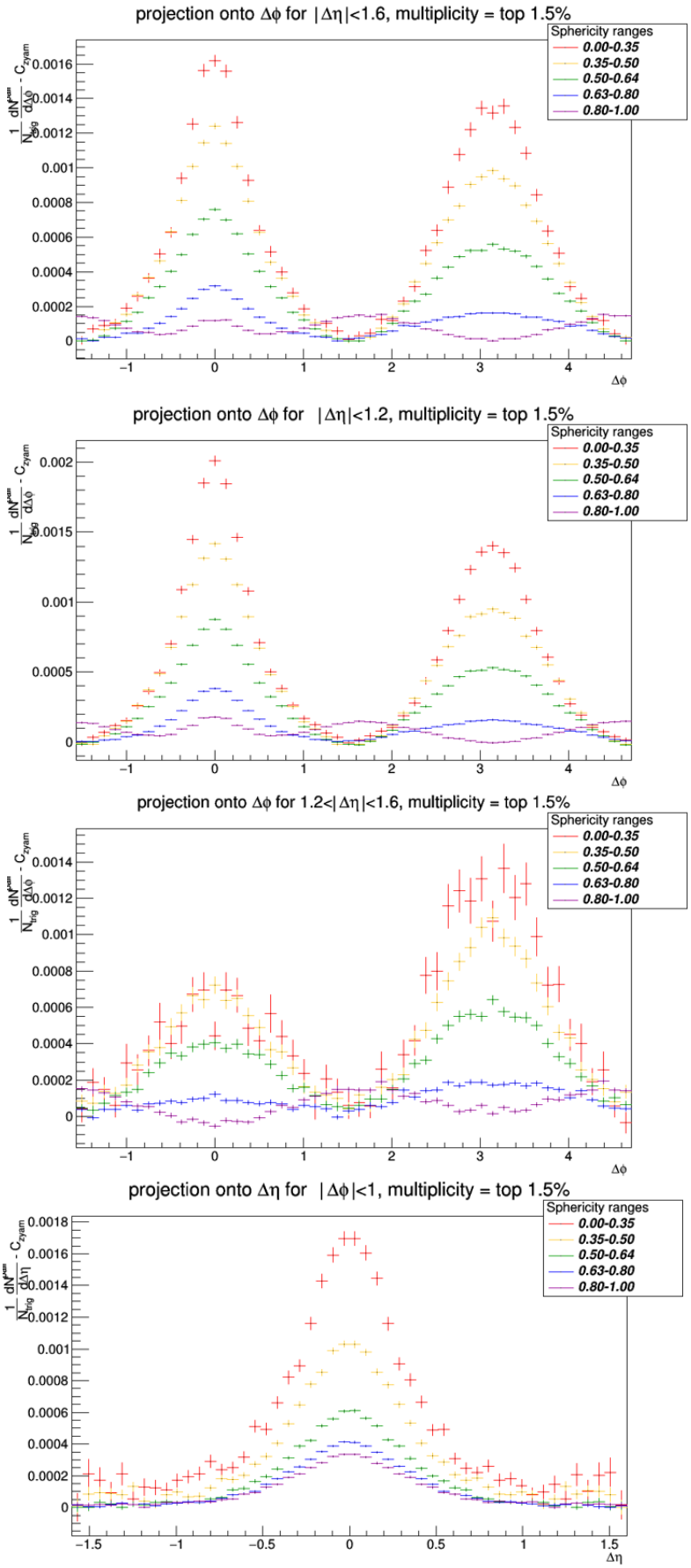

Figure A.2: Projections of the $\Delta\eta - \Delta\varphi$ correlation function onto the 4 axes described in section 7.2 in five different S_T classes. These plots show data, including only events in the top 1.5% of multiplicities and are not normalized.

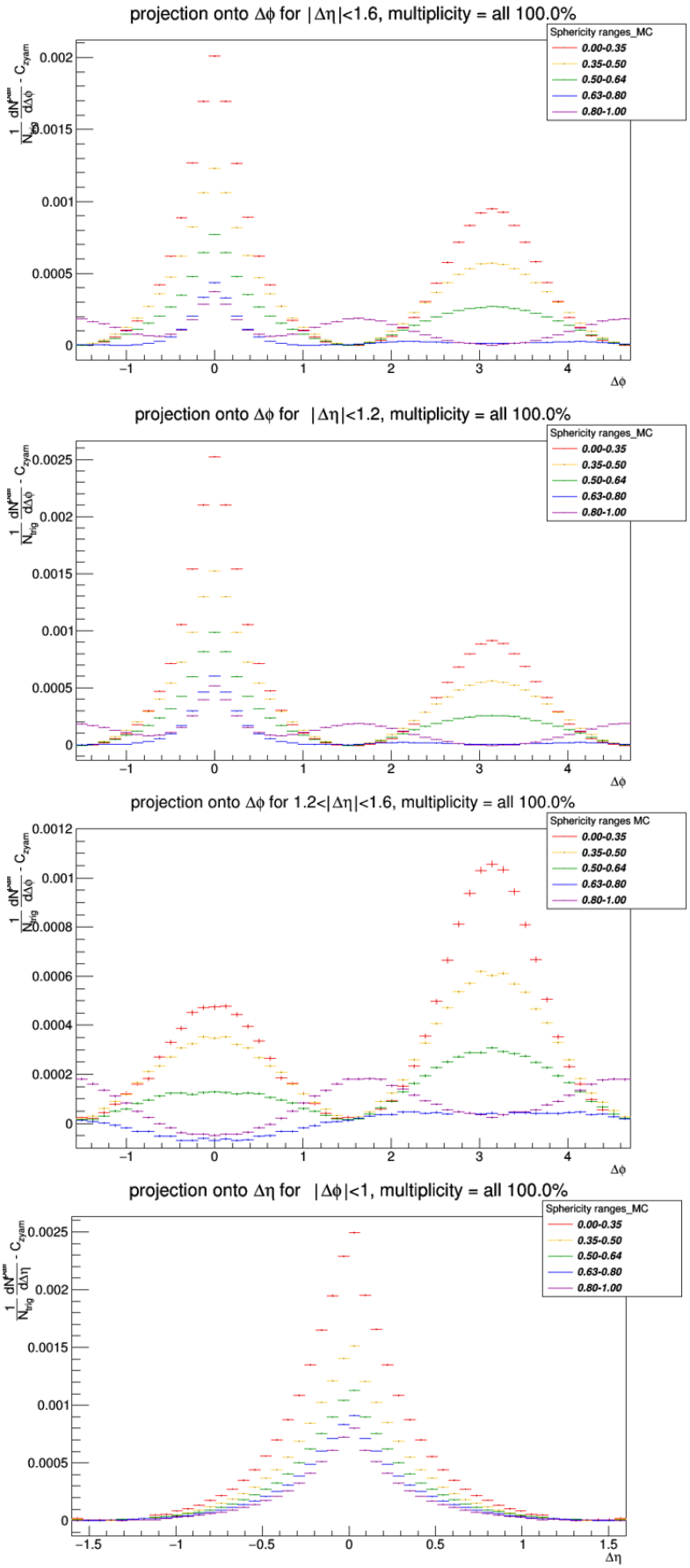

Figure A.3: Projections of the $\Delta\eta - \Delta\varphi$ correlation function onto the 4 axes described in section 7.2 in five different S_T classes. These plots show minimum bias simulations and are not normalized.

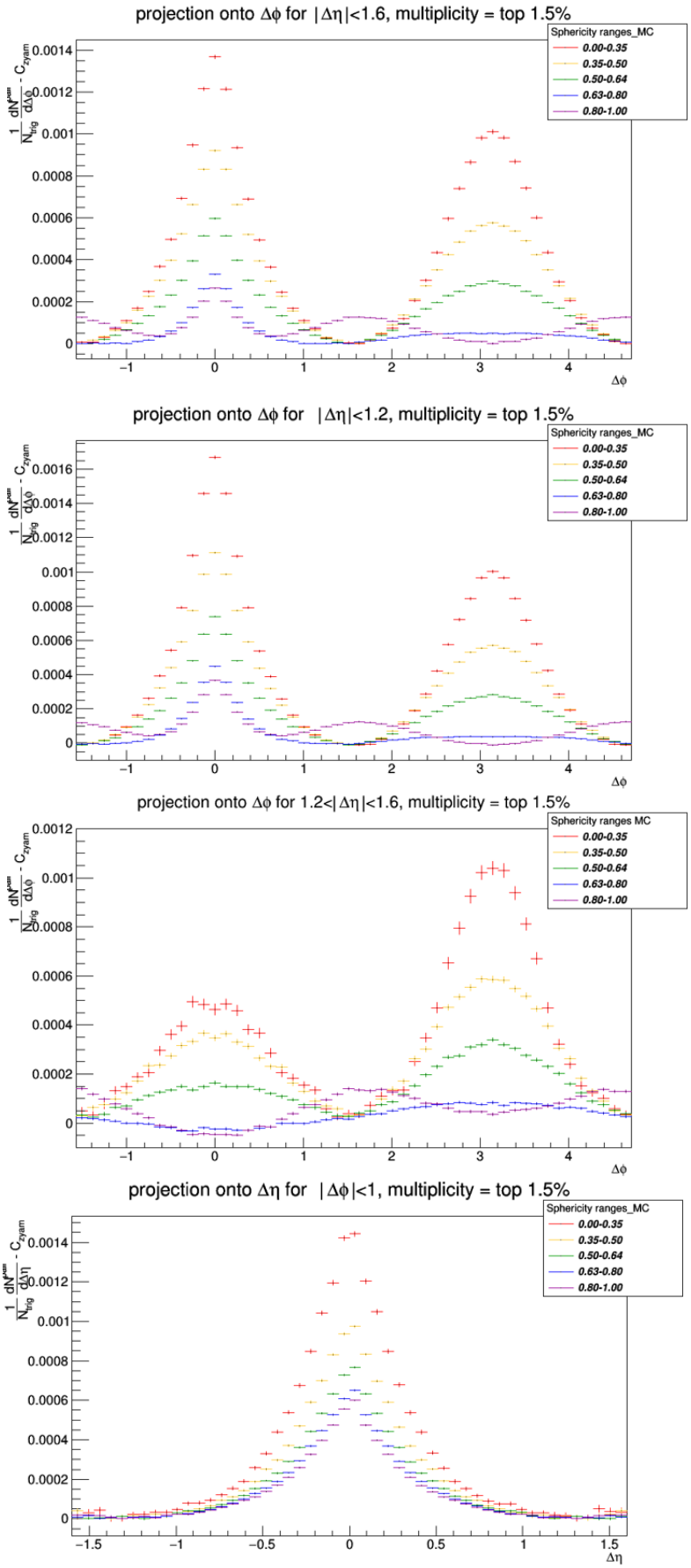

Figure A.4: Projections of the $\Delta\eta - \Delta\varphi$ correlation function onto the 4 axes described in section 7.2 in five different S_T classes. These plots show simulations, including only events in the top 1.5% of multiplicities and are not normalized.

Bibliography

[1] K. Nakamura *et al.*, "Review of particle physics," *J.Phys*, 2010.

[2] P. Higgs, "Broken Symmetries and the Masses of Gauge Bosons," *Phys.Rev.Lett*, 1964.

[3] F. Englert and R. Brout, "Broken Symmetry and the Mass of Gauge Vector Mesons," *Phys.Rev.Lett*, 1964.

[4] G. Guralnik, C. Hagen, and T. Kibble, "Global Conservation Laws and Massless Particles," *Phys.Rev.Lett*, 1964.

[5] S. Chatrchyan *et al.*, "Observation of a new boson at a mass of 125 GeV with the CMS experiment at the LHC," *Phys.Lett*, 2012.

[6] P. D. Group, "Review of Particle Physics," *Chinese Physics C*, vol. 40, no. 10, p. 100001.

[7] MissMJ. [Online]. Available: https://commons.wikimedia.org/wiki/File:Standard_Model_of_Elementary_Particles.svg

[8] W. J. Stirling, "QCD and Collider Physics." [Online]. Available: http://cds.cern.ch/record/317239/files/FERMILAB-Conf-90-164-T.pdf

[9] J. Bartke, *Introduction to Relativistic Heavy Ion Physics*. World Scientific, 2009.

[10] W. Florkowski, *Phenomenology of Ultra-Relativistic Heavy-Ion Collisions*. World Scientific, 2010.

[11] D. Green, "High Pt Physics at Hadron Colliders," p. Appendix D.

[12] K. Wilson, "Confinement of Quarks," *Phys.Rev*, 1974.

[13] G. 't Hooft, "On the Phase Transition Towards Permanent Quark Confinement," *Nucl.Phys*, 1978.

[14] G. 't Hooft, "Topology of the Gauge Condition and New Confinement Phases in Nonabelian Gauge Theories," *Nucl.Phys*, 1981.

[15] D. J. Gross and F. Wilczek, "Ultraviolet Behavior of Nonabelian Gauge Theories," *Phys.Rev.Lett*, 1973.

[16] D. J. Gross and F. Wilczek, "Asymptotically Free Gauge Theories," *Phys.Rev.*, vol. D8, pp. 3633–3652, 1973.

[17] H. Politzer, "Reliable Perturbative Results for Strong Interactions?" *Phys.Rev.Lett*, 1973.

[18] D. d'Enterria, P. Skands *et al.*, "High-precision α_s measurements from LHC to FCC-ee," 2015.

[19] J. M. for the BESIII Collaboration, "BESIII: "charming" physics at an e^+e^- collider machine," *Proceedings of Science*, 2015.

[20] "10 February 2000, CERN press release," 2000. [Online]. Available: https://home.cern/news/press-release/cern/new-state-matter-created-cern

[21] M. Gyulassy, "THE QGP DISCOVERED AT RHIC." [Online]. Available: https://arxiv.org/pdf/nucl-th/0403032v1.pdf

[22] D. Overbye, "In Brookhaven Collider, Scientists Briefly Break a Law of Nature," 2010. [Online]. Available: https://www.nytimes.com/2010/02/16/science/16quark.html

[23] E. Hand, "Hot stuff: CERN physicists create record-breaking subatomic soup," 2012. [Online]. Available: http://blogs.nature.com/news/2012/08/hot-stuff-cern-physicists-create-record-breaking-subatomic-soup.html

[24] J. Gonski, "A Quark Gluon Plasma Primer." [Online]. Available: https://www.particlebites.com/?p=3081

[25] H. Tydesjo, "Net-charge fluctuations in ultra-relativistic nucleus-nucleus collisions," Ph.D. dissertation, Lund U., 2004. [Online]. Available: https://www.hep.lu.se/staff/tydesjo/physics/theses/lichtml/lic.html

[26] R. Albrecht, V. Antonenko *et al.*, "Limits on the Production of Direct Photons in 200A GeV $^{32}S + Au$ Collisions," *Phys. Rev. Lett.*, vol. 76, pp. 3506–3509, May 1996. [Online]. Available: https://link.aps.org/doi/10.1103/PhysRevLett.76.3506

[27] M. Wilde, "Measurement of Direct Photons in pp and Pb–Pb Collisions with ALICE," *Nuclear Physics A*, vol. 904-905, pp. 573c – 576c, 2013. [Online]. Available: http://www.sciencedirect.com/science/article/pii/S0375947413001954

[28] The ALICE collaboration, B. Abelev, J. Adam *et al.*, "Measurement of charged jet suppression in Pb-Pb collisions at $\sqrt{s_{NN}} = 2.76$ TeV," *Journal of High Energy Physics*, 2014. [Online]. Available: https://doi.org/10.1007/JHEP03(2014)013

[29] The ALICE collaboration, K. Aamodt, A. A. Quintana *et al.*, "Suppression of charged particle production at large transverse momentum in central Pb-Pb collisions at $\sqrt{s_{NN}} = 2.76$ TeV," *Physics Letters B*, vol. 696, no. 1, pp. 30 – 39, 2011. [Online]. Available: http://www.sciencedirect.com/science/article/pii/S0370269310013973

[30] C. Suire, "Charmonia production in ALICE," *Nuclear Physics A*, vol. 910-911, pp. 106–113, 2013. [Online]. Available: http://www.sciencedirect.com/science/article/pii/S0375947412004150

[31] P. Foka and M. Janik, "ALICE Masterclass on strangeness," *EPJ Web of Conferences*, vol. 71, 2014.

[32] I. Selyuzhenkov, "Anisotropic Flow and Other Collective Phenomena Measured in Pb-Pb Collisions with ALICE at the LHC," *Progress of Theoretical Physics Supplement*, vol. 193, pp. 153–158, 2012.

[33] A. Toia, "Participants and spectators at the heavy-ion fireball." [Online]. Available: https://cerncourier.com/a/participants-and-spectators-at-the-heavy-ion-fireball/

[34] Deckard, "Evolution of collisions and QGP." [Online]. Available: https://particlesandfriends.wordpress.com/2016/10/14/evolution-of-collisions-and-qgp/

[35] The ALICE collaboration, J. Adam, D. Adamová *et al.*, "Multiplicity and transverse momentum evolution of charge-dependent correlations in pp, p-Pb, and Pb-Pb collisions at the LHC," *The European Physical Journal C*, vol. 76, Feb 2016.

[36] J. Adams *et al.*, "Distributions of charged hadrons associated with high transverse momentum particles in pp and Au+Au collisions at $\sqrt{s_{NN}} = 200$ GeV," *Phys.Rev.Lett*, 2005.

[37] B. Alver *et al.*, "High transverse momentum triggered correlations over a large pseudorapidity acceptance in Au+Au collisions at $\sqrt{s_{NN}} = 200$ GeV," *Phys.Rev.Lett*, 2010.

[38] H. Agakishiev *et al.*, "Measurements of Dihadron Correlations Relative to the Event Plane in Au+Au Collisions at $\sqrt{s_{NN}} = 200$ GeV," 2010.

[39] G. Agakishiev *et al.*, "Anomalous centrality evolution of twoparticle angular correlations from Au-Au collisions at $\sqrt{s_{NN}} = 62$ and 200 GeV," *Phys.Rev*, 2012.

[40] E. Shuryak, "On the origin of the 'Ridge' phenomenon induced by jets in heavy ion collisions," *Phys.Rev*, 2007.

[41] S. A. Voloshin, "Transverse radial expansion in nuclear collisions and two particle correlations," *Phys.Lett*, 2006.

[42] C.-Y. Wong, "Momentum kick model description of the near-side ridge and jet quenching," *Phys. Rev. C*, vol. 78, 2008.

[43] A. Dumitru, F. Gelis, L. McLerran *et al.*, "Glasma flux tubes and the near side ridge phenomenon at RHIC," *Nuclear Physics A*, vol. 810, 2008.

[44] V. Khachatryan *et al.*, "Observation of Long-Range Near-Side Angular Correlations in Proton-Proton Collisions at the LHC," *JHEP*, 2010.

[45] J. Schukraft, "Heavy ion physics at the Large Hadron Collider: what is new? What is next?" *Phys.Scripta*, 2013.

[46] The CMS collaboration, V. Khachatryan, A. Sirunyan *et al.*, "Measurement of Long-Range Near-Side Two-Particle Angular Correlations in pp Collisions at $\sqrt{s} = 13$ TeV," *Physical Review Letters*, vol. 116, 2016.

[47] M. Gyulassy and L. McLerran, "New forms of QCD matter discovered at RHIC," *Nucl.Phys*, 2005.

[48] K. Itakura, "Color Glass Condensate in QCD at High Energy," *High Energy Physics*, pp. 397–400, 2005.

[49] H. Schopper and L. D. Lella, *60 Years of CERN Experiments and Discoveries*. World Scientific Publishing Co. Pte. Ltd., 2015, vol. 23.

[50] P. Foka and M. A. Janik, "An overview of experimental results from ultra-relativistic heavy-ion collisions at the CERN LHC: Bulk properties and dynamical evolution," *Reviews in Physics*, vol. 1, pp. 154 – 171, 2016. [Online]. Available: http://www.sciencedirect.com/science/article/pii/S2405428316300156

[51] J. Engelen *et al.*, "Ten years on and the LHC accelerator is still not done colliding," 2020. [Online]. Available: https://www.nikhef.nl/en/news/ten-years-on-and-the-lhc-accelerator-is-still-not-done-colliding/

[52] L. Evans and P. Bryant, "LHC Machine," *Journal of Instrumentation*, vol. 3, no. 08, pp. S08 001–S08 001, 2008. [Online]. Available: https://iopscience.iop.org/article/10.1088/1748-0221/3/08/S08001/pdf

[53] "Cern LHC sees high-energy success," 2010. [Online]. Available: http://news.bbc.co.uk/2/hi/science/nature/8593780.stm

[54] [Online]. Available: http://lhc-closer.es/taking_a_closer_look_at_lhc/0.magnetic_multipoles

[55] G. Aad *et al.*, "The ATLAS Experiment at the CERN Large Hadron Collider," *JINST*, 2008.

[56] S. Chatrchyan *et al.*, "The CMS experiment at the CERN LHC," *JINST*, 2008.

[57] K. Aamodt *et al.*, "The ALICE experiment at the CERN LHC," *JINST*, 2008.

[58] The LHCb Collaboration, A. A. Alves, L. M. A. Filho *et al.*, "The LHCb Detector at the LHC," *Journal of Instrumentation*, 2008.

[59] J. Schukraft, "ALICE status and highlights," *PoS*, 2010.

[60] "ALICE figure repository." [Online]. Available: https://alice-figure.web.cern.ch/node/11218

[61] The ALICE Collaboration, "Alice Technical Design Report of the Inner Tracking System (ITS)," Tech. Rep., 1999.

[62] The ALICE Collaboration, "Alice Technical Design Report of the Time Projection Chamber (TPC)," Tech. Rep., 2000.

[63] The ALICE Collaboration, "ALICE Technical Design Report of the Transition-Radiation Detector (TRD)," Tech. Rep., 2009.

[64] M. Braß, "Estimating Hadron Contamination in Pb-Pb Collisions at $\sqrt{s_{NN}} = 2.76$ TeV for Low Transversal Momenta with TPC, TOF and TRD of the ALICE Experiment," Ph.D. dissertation, University of Heidelberg, 2014. [Online]. Available: https://www.physi.uni-heidelberg.de/Publications/Bachelorarbeit_Martin_Brass.pdf

[65] The ALICE Collaboration, G. Dellacasa *et al.*, "ALICE Technical Design Report of the Time-Of-Flight system (TOF)," CERN, Tech. Rep.

[66] S. Beole *et al.*, "ALICE Technical Design Report: Detector for High Momentum PID," Tech. Rep., 1998.

[67] M. Ivanov, "Identified charged hadron production measured with ALICE at the LHC," *Nuclear Physics A*, 2013.

[68] The ALICE Collaboration, "ALICE EMCal Physics Performance Report," CERN, Tech. Rep., 2009.

[69] G. Dellacasa *et al.*, "ALICE Technical Design Report of the Photon Spectrometer (PHOS)," 1999.

[70] The ALICE Collaboration, "ALICE Technical Design Report on Forward Detectors: FMD, V0, T0," Tech. Rep., 2004.

[71] C. Pagliarone and A. Fernandez-Tellez, "Cosmic Ray Physics with ACORDE at LHC," *J. Phys. Conf. Ser*, 2007.

[72] G. Dellacasa *et al.*, "ALICE technical design report of the zero degree calorimeter (ZDC)," Tech. Rep., 1999.

[73] The ALICE Collaboration, "ALICE Technical Design Report of the Dimuon Forward Spectrometer," Tech. Rep., 1999.

[74] P. Skowronski, "Space-time evolution of nuclear collisions," 2006.

[75] The ALICE Collaboration, J. Adam, D. Adamová *et al.*, "Particle identification in ALICE: a Bayesian approach," *The European Physical Journal Plus*, 2016. [Online]. Available: https://doi.org/10.1140/epjp/i2016-16168-5

[76] G. Simatović, "Event shape dependent pion femtoscopy of proton-proton collisions at 7 TeV center-of-mass energy," Ph.D. dissertation, University of Zagreb, 2015. [Online]. Available: https://bib.irb.hr/datoteka/816773.thesis.pdf

[77] The ALICE collaboration, B. Abelev, J. Adam *et al.*, "Transverse sphericity of primary charged particles in minimum bias proton-proton collisions at $\sqrt{s} = 0.9$, 2.76 and 7 TeV," *The European Physical Journal C*, 2012.

[78] R. Brun *et al.*, "GEANT3 User Guide," *CERN Data Handling Division*, 1985.

[79] M. A. Janik, "Two-particle correlations as a function of relative azimuthal angle and pseudorapidity in proton-proton collisions registered by the ALICE experiment," Ph.D. dissertation, Warsaw University of Technology, 2014. [Online]. Available: https://cds.cern.ch/record/2093543?ln=en

[80] The ALICE collaboration, K. Aamodt *et al.*, "Production of pions, kaons and protons in pp collisions at $\sqrt{s} = 900$ GeV with ALICE at the LHC," *The European Physical Journal C*, vol. 71, p. 1655, 2011.

[81] The CMS collaboration, V. Khachatryan, A. M. Sirunyan *et al.*, "Observation of long-range, near-side angular correlations in proton-proton collisions at the LHC," *Journal of High Energy Physics*, 2010.

[82] E. P. Lezama, G. Paić, E. C. Flores *et al.*, "Study of the PYTHIA $\Delta\eta\Delta\phi$ correlation as a function of multiplicity and transverse sphericity in proton-proton collisions at 7 TeV," *Journal of Physics: Conference Series*, vol. 578, p. 012005, 2015. [Online]. Available: https://doi.org/10.1088%2F1742-6596%2F578%2F1%2F012005

[83] M. Jerčić, "Reprodukcija i izučavanje fenomena grebena ("ridge") u korelacijama dviju čestica na ALICE detektoru," Master's thesis, University of Zagreb, 2016.

Curriculum vitae

Filip Erhardt was born on June 28, 1989 in Zagreb. In 2008 he enrolled into the physics programme at the Physics Department of the Faculty of Science at the University of Zagreb where he obtained his Master's Degree with his thesis titled "Characterization of silicon pixel detectors" in 2014. Later that year he began working at the Faculty of Science as a PhD student and teaching assistant in the subjects Fundamentals of physics and General physics. During his PhD research he became a member of the RD51 and the ALICE collaborations at CERN. He performed the relative calibration of the TRD (Transitional radiation detector) of the ALICE experiment using radioactive Kr gas in 2015. In the scope of his PhD work he performed an analysis on two-particle angular correlations as well as work on the development of GEM detectors for the ALICE TPC upgrade. His work was presented at Quark Matter 2018 and 2019 which are the largest conferences in his field as well as at several smaller conferences. He has also organized a conference as part of the local organizing committee of the ALICE Week 2014 conference and played a role in organizing the summer school for young physicists from 2016-2019. He has published (as a co-author) 209 papers cited 6850 times according to INSPIRE HEP.

List of publications:

[1] S. Acharya et al. Charged-particle multiplicity distributions over a wide pseudorapidity range in proton-proton collisions at $\sqrt{s} = 0.9$, 7, and 8 TeV. *Eur. Phys. J. C*, 77(12):852, 2017.

[2] S. Acharya et al. Energy dependence of forward-rapidity J/ψ and ψ(2S) production in pp collisions at the LHC. *Eur. Phys. J. C*, 77(6):392, 2017.

[3] S. Acharya et al. J/ψ elliptic flow in Pb-Pb collisions at $\sqrt{s_{\rm NN}} = 5.02$ TeV. *Phys. Rev. Lett.*, 119(24):242301, 2017.

[4] S. Acharya et al. Kaon femtoscopy in Pb-Pb collisions at $\sqrt{s_{\rm NN}} = 2.76$ TeV. *Phys. Rev. C*, 96(6):064613, 2017.

[5] S. Acharya et al. Linear and non-linear flow modes in Pb-Pb collisions at $\sqrt{s_{\rm NN}} = 2.76$ TeV. *Phys. Lett. B*, 773:68–80, 2017.

[6] S. Acharya et al. Measurement of D-meson production at mid-rapidity in pp collisions at $\sqrt{s} = 7$ TeV. *Eur. Phys. J. C*, 77(8):550, 2017.

[7] S. Acharya et al. Measurement of deuteron spectra and elliptic flow in Pb–Pb collisions at $\sqrt{s_{\rm NN}} =$ 2.76 TeV at the LHC. *Eur. Phys. J. C*, 77(10):658, 2017.

[8] S. Acharya et al. Measuring $\rm K^0_S K^{\pm}$ interactions using Pb-Pb collisions at $\sqrt{s_{\rm NN}} = 2.76$ TeV. *Phys. Lett. B*, 774:64–77, 2017.

[9] S. Acharya et al. Production of muons from heavy-flavour hadron decays in p-Pb collisions at $\sqrt{s_{\rm NN}} = 5.02$ TeV. *Phys. Lett. B*, 770:459–472, 2017.

[10] S. Acharya et al. Production of π^0 and η mesons up to high transverse momentum in pp collisions at 2.76 TeV. *Eur. Phys. J. C*, 77(5):339, 2017.

[11] S. Acharya et al. Searches for transverse momentum dependent flow vector fluctuations in Pb-Pb and p-Pb collisions at the LHC. *JHEP*, 09:032, 2017.

[12] S. Acharya et al. Anisotropic flow in Xe-Xe collisions at $\sqrt{s_{\rm NN}} = 5.44$ TeV. *Phys. Lett. B*, 784:82–95, 2018.

[13] S. Acharya et al. Anisotropic flow of identified particles in Pb-Pb collisions at $\sqrt{s}_{\rm NN} = 5.02$ TeV. *JHEP*, 09:006, 2018.

[14] S. Acharya et al. Azimuthally-differential pion femtoscopy relative to the third harmonic event plane in Pb-Pb collisions at $\sqrt{s_{_{NN}}} = 2.76$ TeV. *Phys. Lett. B*, 785:320–331, 2018.

[15] S. Acharya et al. Constraining the magnitude of the Chiral Magnetic Effect with Event Shape Engineering in Pb-Pb collisions at $\sqrt{s_{\rm NN}} = 2.76$ TeV. *Phys. Lett. B*, 777:151–162, 2018.

[16] S. Acharya et al. Constraints on jet quenching in p-Pb collisions at $\sqrt{s_{\rm NN}} = 5.02$ TeV measured by the event-activity dependence of semi-inclusive hadron-jet distributions. *Phys. Lett. B*, 783:95–113, 2018.

[17] S. Acharya et al. *D*-meson azimuthal anisotropy in midcentral Pb-Pb collisions at $\sqrt{s_{\rm NN}} = 5.02$ TeV. *Phys. Rev. Lett.*, 120(10):102301, 2018.

[18] S. Acharya et al. Dielectron production in proton-proton collisions at $\sqrt{s} = 7$ TeV. *JHEP*, 09:064, 2018.

[19] S. Acharya et al. Energy dependence and fluctuations of anisotropic flow in Pb-Pb collisions at $\sqrt{s_{\rm NN}} =$ 5.02 and 2.76 TeV. *JHEP*, 07:103, 2018.

[20] S. Acharya et al. First measurement of jet mass in Pb–Pb and p–Pb collisions at the LHC. *Phys. Lett. B*, 776:249–264, 2018.

[21] S. Acharya et al. First measurement of Ξ_c^0 production in pp collisions at $\sqrt{s}$ = 7 TeV. *Phys. Lett. B*, 781:8–19, 2018.

[22] S. Acharya et al. Inclusive J/ψ production at forward and backward rapidity in p-Pb collisions at $\sqrt{s_{\rm NN}}$ = 8.16 TeV. *JHEP*, 07:160, 2018.

[23] S. Acharya et al. Inclusive J/ψ production in Xe–Xe collisions at $\sqrt{s_{\rm NN}}$ = 5.44 TeV. *Phys. Lett. B*, 785:419–428, 2018.

[24] S. Acharya et al. Λ_c^+ production in pp collisions at $\sqrt{s}$ = 7 TeV and in p-Pb collisions at $\sqrt{s_{\rm NN}}$ = 5.02 TeV. *JHEP*, 04:108, 2018.

[25] S. Acharya et al. Longitudinal asymmetry and its effect on pseudorapidity distributions in Pb-Pb collisions at $\sqrt{s_{\rm NN}}$ = 2.76 TeV. *Phys. Lett. B*, 781:20–32, 2018.

[26] S. Acharya et al. Measurement of $\rm D^0$, $\rm D^+$, $\rm D^{*+}$ and $\rm D_s^+$ production in Pb-Pb collisions at $\sqrt{s_{\rm NN}}$ = 5.02 TeV. *JHEP*, 10:174, 2018.

[27] S. Acharya et al. Measurement of the inclusive J/ ψ polarization at forward rapidity in pp collisions at $\sqrt{s}$ = 8 TeV. *Eur. Phys. J. C*, 78(7):562, 2018.

[28] S. Acharya et al. Measurement of $\rm Z^0$-boson production at large rapidities in Pb-Pb collisions at $\sqrt{s_{\rm NN}}$ = 5.02 TeV. *Phys. Lett. B*, 780:372–383, 2018.

[29] S. Acharya et al. Measurements of low-$\rm p_T$ electrons from semileptonic heavy-flavour hadron decays at mid-rapidity in pp and Pb-Pb collisions at $\sqrt{s_{\rm NN}}$ = 2.76 TeV. *JHEP*, 10:061, 2018.

[30] S. Acharya et al. Medium modification of the shape of small-radius jets in central Pb-Pb collisions at $\sqrt{s_{\rm NN}} = 2.76\,TeV$. *JHEP*, 10:139, 2018.

[31] S. Acharya et al. Neutral pion and η meson production at mid-rapidity in Pb-Pb collisions at $\sqrt{s_{\rm NN}}$ = 2.76 TeV. *Phys. Rev. C*, 98(4):044901, 2018.

[32] S. Acharya et al. Neutral pion and η meson production in p-Pb collisions at $\sqrt{s_{\rm NN}}$ = 5.02 TeV. *Eur. Phys. J. C*, 78(8):624, 2018.

[33] S. Acharya et al. ϕ meson production at forward rapidity in Pb-Pb collisions at $\sqrt{s_{\rm NN}}$ = 2.76 TeV. *Eur. Phys. J. C*, 78(7):559, 2018.

[34] S. Acharya et al. π^0 and η meson production in proton-proton collisions at $\sqrt{s}$ = 8 TeV. *Eur. Phys. J. C*, 78(3):263, 2018.

[35] S. Acharya et al. Production of ^{4}He and $^4\overline{\rm He}$ in Pb-Pb collisions at $\sqrt{s_{\rm NN}}$ = 2.76 TeV at the LHC. *Nucl. Phys. A*, 971:1–20, 2018.

[36] S. Acharya et al. Production of deuterons, tritons, ^{3}He nuclei and their antinuclei in pp collisions at $\sqrt{s}$ = 0.9, 2.76 and 7 TeV. *Phys. Rev. C*, 97(2):024615, 2018.

[37] S. Acharya et al. Prompt and non-prompt J/ψ production and nuclear modification at mid-rapidity in p–Pb collisions at $\sqrt{s_N N}$ = 5.02 TeV. *Eur. Phys. J. C*, 78(6):466, 2018.

[38] S. Acharya et al. Search for collectivity with azimuthal J/ψ-hadron correlations in high multiplicity p-Pb collisions at $\sqrt{s_{\rm NN}}$ = 5.02 and 8.16 TeV. *Phys. Lett. B*, 780:7–20, 2018.

[39] S. Acharya et al. Systematic studies of correlations between different order flow harmonics in Pb-Pb collisions at $\sqrt{s_{\rm NN}}$ = 2.76 TeV. *Phys. Rev. C*, 97(2):024906, 2018.

[40] S. Acharya et al. The ALICE Transition Radiation Detector: construction, operation, and performance. *Nucl. Instrum. Meth. A*, 881:88–127, 2018.

[41] S. Acharya et al. Transverse momentum spectra and nuclear modification factors of charged particles in pp, p-Pb and Pb-Pb collisions at the LHC. *JHEP*, 11:013, 2018.

[42] S. Acharya et al. ${}^{3}_{\Lambda}\mathrm{H}$ and ${}^{3}_{\bar{\Lambda}}\bar{\mathrm{H}}$ lifetime measurement in Pb-Pb collisions at $\sqrt{s_{\mathrm{NN}}}$ = 5.02 TeV via two-body decay. *Phys. Lett. B*, 797:134905, 2019.

[43] S. Acharya et al. Analysis of the apparent nuclear modification in peripheral Pb–Pb collisions at 5.02 TeV. *Phys. Lett. B*, 793:420–432, 2019.

[44] S. Acharya et al. Azimuthal Anisotropy of Heavy-Flavor Decay Electrons in p-Pb Collisions at $\sqrt{s_{\mathrm{NN}}}$ = 5.02 TeV. *Phys. Rev. Lett.*, 122(7):072301, 2019.

[45] S. Acharya et al. Azimuthal correlations of prompt D mesons with charged particles in pp and p-Pb collisions at $\sqrt{s_{\mathrm{NN}}}$ = 5.02 TeV. 10 2019.

[46] S. Acharya et al. Calibration of the photon spectrometer PHOS of the ALICE experiment. *JINST*, 14(05):P05025, 2019.

[47] S. Acharya et al. Centrality and pseudorapidity dependence of the charged-particle multiplicity density in Xe–Xe collisions at $\sqrt{s_{\mathrm{NN}}}$ =5.44TeV. *Phys. Lett. B*, 790:35–48, 2019.

[48] S. Acharya et al. Charged jet cross section and fragmentation in proton-proton collisions at $\sqrt{s}$ = 7 TeV. *Phys. Rev. D*, 99(1):012016, 2019.

[49] S. Acharya et al. Charged-particle production as a function of multiplicity and transverse spherocity in pp collisions at $\sqrt{s}$ = 5.02 and 13 TeV. *Eur. Phys. J. C*, 79(10):857, 2019.

[50] S. Acharya et al. Charged-particle pseudorapidity density at mid-rapidity in p-Pb collisions at $\sqrt{s_{\mathrm{NN}}}$ = 8.16 TeV. *Eur. Phys. J. C*, 79(4):307, 2019.

[51] S. Acharya et al. Coherent J/ψ photoproduction at forward rapidity in ultra-peripheral Pb-Pb collisions at $\sqrt{s_{\mathrm{NN}}}$ = 5.02 TeV. *Phys. Lett. B*, 798:134926, 2019.

[52] S. Acharya et al. Dielectron and heavy-quark production in inelastic and high-multiplicity proton–proton collisions at $\sqrt{s_{\mathrm{NN}}}$ = 13TeV. *Phys. Lett. B*, 788:505–518, 2019.

[53] S. Acharya et al. Direct photon elliptic flow in Pb-Pb collisions at $\sqrt{s_{\mathrm{NN}}}$ = 2.76 TeV. *Phys. Lett. B*, 789:308–322, 2019.

[54] S. Acharya et al. Direct photon production at low transverse momentum in proton-proton collisions at $\sqrt{s}$ = 2.76 and 8 TeV. *Phys. Rev. C*, 99(2):024912, 2019.

[55] S. Acharya et al. Energy dependence of exclusive J/ψ photoproduction off protons in ultra-peripheral p–Pb collisions at $\sqrt{s_{\mathrm{NN}}}$ = 5.02 TeV. *Eur. Phys. J. C*, 79(5):402, 2019.

[56] S. Acharya et al. Event-shape and multiplicity dependence of freeze-out radii in pp collisions at $\sqrt{s}$ = 7 TeV. *JHEP*, 09:108, 2019.

[57] S. Acharya et al. Event-shape engineering for the D-meson elliptic flow in mid-central Pb-Pb collisions at $\sqrt{s_{\mathrm{NN}}}$ = 5.02 TeV. *JHEP*, 02:150, 2019.

[58] S. Acharya et al. First Observation of an Attractive Interaction between a Proton and a Cascade Baryon. *Phys. Rev. Lett.*, 123(11):112002, 2019.

[59] S. Acharya et al. Inclusive J/ψ production at mid-rapidity in pp collisions at $\sqrt{s}$ = 5.02 TeV. *JHEP*, 10:084, 2019.

[60] S. Acharya et al. Investigations of Anisotropic Flow Using Multiparticle Azimuthal Correlations in pp, p-Pb, Xe-Xe, and Pb-Pb Collisions at the LHC. *Phys. Rev. Lett.*, 123(14):142301, 2019.

[61] S. Acharya et al. Jet fragmentation transverse momentum measurements from di-hadron correlations in $\sqrt{s}$ = 7 TeV pp and $\sqrt{s_{\mathrm{NN}}}$ = 5.02 TeV p-Pb collisions. *JHEP*, 03:169, 2019.

[62] S. Acharya et al. $K^{*}(892)^{0}$ and $\phi(1020)$ production at midrapidity in pp collisions at $\sqrt{s}$ = 8 TeV. 10 2019.

[63] S. Acharya et al. Λ_c^+ production in Pb-Pb collisions at $\sqrt{s_{\rm NN}} = 5.02$ TeV. *Phys. Lett. B*, 793:212–223, 2019.

[64] S. Acharya et al. Measurement of charged jet cross section in *pp* collisions at $\sqrt{s} = 5.02$ TeV. *Phys. Rev. D*, 100(9):092004, 2019.

[65] S. Acharya et al. Measurement of $\rm D^0$, $\rm D^+$, $\rm D^{*+}$ and $\rm D_s^+$ production in pp collisions at $\sqrt{s} = 5.02$ TeV with ALICE. *Eur. Phys. J. C*, 79(5):388, 2019.

[66] S. Acharya et al. Measurement of dielectron production in central Pb-Pb collisions at $\sqrt{s_{\rm NN}} = 2.76$ TeV. *Phys. Rev. C*, 99(2):024002, 2019.

[67] S. Acharya et al. Measurement of jet radial profiles in Pb–Pb collisions at $\sqrt{s_{\rm NN}} = 2.76$ TeV. *Phys. Lett. B*, 796:204–219, 2019.

[68] S. Acharya et al. Measurement of prompt $\rm D^0$, $\rm D^+$, $\rm D^{*+}$, and $\rm D_S^+$ production in p–Pb collisions at $\sqrt{s_{\rm NN}} = 5.02$ TeV. *JHEP*, 12:092, 2019.

[69] S. Acharya et al. Measurement of the inclusive isolated photon production cross section in pp collisions at $\sqrt{s} = 7$ TeV. *Eur. Phys. J. C*, 79(11):896, 2019.

[70] S. Acharya et al. Measurement of the production of charm jets tagged with $\rm D^0$ mesons in pp collisions at $\sqrt{\rm s} = 7$ TeV. *JHEP*, 08:133, 2019.

[71] S. Acharya et al. Measurement of $\Upsilon(1S)$ elliptic flow at forward rapidity in Pb-Pb collisions at $\sqrt{s_{\rm NN}} = 5.02$ TeV. *Phys. Rev. Lett.*, 123(19):192301, 2019.

[72] S. Acharya et al. Measuring $\rm K_S^0K^\pm$ interactions using pp collisions at $\sqrt{s} = 7$ TeV. *Phys. Lett. B*, 790:22–34, 2019.

[73] S. Acharya et al. Multiplicity dependence of (anti-)deuteron production in pp collisions at $\sqrt{s} = 7$ TeV. *Phys. Lett. B*, 794:50–63, 2019.

[74] S. Acharya et al. Multiplicity dependence of light-flavor hadron production in pp collisions at $\sqrt{s} = 7$ TeV. *Phys. Rev. C*, 99(2):024906, 2019.

[75] S. Acharya et al. One-dimensional charged kaon femtoscopy in p-Pb collisions at $\sqrt{s_{\rm NN}} = 5.02$ TeV. *Phys. Rev. C*, 100(2):024002, 2019.

[76] S. Acharya et al. p-p, p-Λ and Λ-Λ correlations studied via femtoscopy in pp reactions at $\sqrt{s} = 7$ TeV. *Phys. Rev. C*, 99(2):024001, 2019.

[77] S. Acharya et al. Production of muons from heavy-flavour hadron decays in pp collisions at $\sqrt{s} = 5.02$ TeV. *JHEP*, 09:008, 2019.

[78] S. Acharya et al. Production of the $\rho(770)^0$ meson in pp and Pb-Pb collisions at $\sqrt{s_{\rm NN}} = 2.76$ TeV. *Phys. Rev. C*, 99(6):064901, 2019.

[79] S. Acharya et al. Real-time data processing in the ALICE High Level Trigger at the LHC. *Comput. Phys. Commun.*, 242:25–48, 2019.

[80] S. Acharya et al. Relative particle yield fluctuations in Pb-Pb collisions at $\sqrt{s_{\rm NN}} = 2.76$ TeV. *Eur. Phys. J. C*, 79(3):236, 2019.

[81] S. Acharya et al. Study of J/ψ azimuthal anisotropy at forward rapidity in Pb-Pb collisions at $\sqrt{s_{\rm NN}} = 5.02$ TeV. *JHEP*, 02:012, 2019.

[82] S. Acharya et al. Study of the Λ-Λ interaction with femtoscopy correlations in pp and p-Pb collisions at the LHC. *Phys. Lett. B*, 797:134822, 2019.

[83] S. Acharya et al. Suppression of $\Lambda(1520)$ resonance production in central Pb-Pb collisions at $\sqrt{s_{\rm NN}} = 2.76$ TeV. *Phys. Rev. C*, 99:024905, 2019.

[84] S. Acharya et al. Transverse momentum spectra and nuclear modification factors of charged particles in Xe-Xe collisions at $\sqrt{s_{\rm NN}} = 5.44$ TeV. *Phys. Lett. B*, 788:166–179, 2019.

[85] S. Acharya et al. Two particle differential transverse momentum and number density correlations in p-Pb and Pb-Pb at the LHC. *Phys. Rev. C*, 100(4):044903, 2019.

[86] S. Acharya et al. Υ suppression at forward rapidity in Pb-Pb collisions at $\sqrt{s_{\rm NN}} = 5.02$ TeV. *Phys. Lett. B*, 790:89–101, 2019.

[87] S. Acharya et al. A new laboratory to study hadron-hadron interactions. 5 2020.

[88] S. Acharya et al. (Anti-)Deuteron production in pp collisions at $\sqrt{s} = 13$ TeV. 3 2020.

[89] S. Acharya et al. Centrality and transverse momentum dependence of inclusive J/ψ production at midrapidity in Pb-Pb collisions at $\sqrt{s_{\rm NN}} = 5.02$ TeV. *Phys. Lett. B*, 805:135434, 2020.

[90] S. Acharya et al. Coherent photoproduction of ρ^0 vector mesons in ultra-peripheral Pb-Pb collisions at $\sqrt{s_{\rm NN}} = 5.02$ TeV. *JHEP*, 06:035, 2020.

[91] S. Acharya et al. Constraining the Chiral Magnetic Effect with charge-dependent azimuthal correlations in Pb-Pb collisions at $\sqrt{s_{\rm NN}} = 2.76$ and 5.02 TeV. 5 2020.

[92] S. Acharya et al. Dielectron production in proton-proton and proton-lead collisions at $\sqrt{s_{\rm NN}} = 5.02$ TeV. 5 2020.

[93] S. Acharya et al. Elliptic and triangular flow of (anti)deuterons in Pb-Pb collisions at $\sqrt{s_{\rm NN}} = 5.02$ TeV. 5 2020.

[94] S. Acharya et al. Elliptic flow of electrons from beauty-hadron decays in Pb-Pb collisions at $\sqrt{s_{\rm NN}} =$ 5.02 TeV. 5 2020.

[95] S. Acharya et al. Evidence of rescattering effect in Pb-Pb collisions at the LHC through production of $K^*(892)^0$ and $\phi(1020)$ mesons. *Phys. Lett. B*, 802:135225, 2020.

[96] S. Acharya et al. Exploration of jet substructure using iterative declustering in pp and Pb–Pb collisions at LHC energies. *Phys. Lett. B*, 802:135227, 2020.

[97] S. Acharya et al. First measurement of quarkonium polarization in nuclear collisions at the LHC. 5 2020.

[98] S. Acharya et al. Global baryon number conservation encoded in net-proton fluctuations measured in Pb-Pb collisions at $\sqrt{s_{\rm NN}} = 2.76$ TeV. *Phys. Lett. B*, 807:135564, 2020.

[99] S. Acharya et al. Global polarization of Λ and $\overline{\Lambda}$ hyperons in Pb-Pb collisions at the LHC. *Phys. Rev. C*, 101(4):044611, 2020.

[100] S. Acharya et al. Investigation of the p-Σ^0 interaction via femtoscopy in pp collisions. *Phys. Lett. B*, 805:135419, 2020.

[101] S. Acharya et al. Jet-hadron correlations measured relative to the second order event plane in Pb-Pb collisions at $\sqrt{s_{\rm NN}} = 2.76$ TeV. *Phys. Rev. C*, 101(6):064901, 2020.

[102] S. Acharya et al. J/ψ elliptic and triangular flow in Pb-Pb collisions at $\sqrt{s_{\rm NN}} = 5.02$ TeV. 5 2020.

[103] S. Acharya et al. J/ψ production as a function of charged-particle multiplicity in p-Pb collisions at $\sqrt{s_{NN}} = 8.16$ TeV. 4 2020.

[104] S. Acharya et al. ΛK femtoscopy in Pb-Pb collisions at $\sqrt{s_{\rm NN}} = 2.76$ TeV. 5 2020.

[105] S. Acharya et al. Linear and non-linear flow modes of charged hadrons in Pb-Pb collisions at $\sqrt{s_{\rm NN}} =$ 5.02 TeV. *JHEP*, 05:085, 2020.

[106] S. Acharya et al. Longitudinal and azimuthal evolution of two-particle transverse momentum correlations in Pb-Pb collisions at $\sqrt{s_{\rm NN}}$ = 2.76 TeV. *Phys. Lett. B*, 804:135375, 2020.

[107] S. Acharya et al. Measurement of electrons from heavy-flavour hadron decays as a function of multiplicity in p-Pb collisions at $\sqrt{s_{\rm NN}}$ = 5.02 TeV. *JHEP*, 02:077, 2020.

[108] S. Acharya et al. Measurement of electrons from semileptonic heavy-flavour hadron decays at midrapidity in pp and Pb-Pb collisions at $\sqrt{s_{\rm NN}}$ = 5.02 TeV. *Phys. Lett. B*, 804:135377, 2020.

[109] S. Acharya et al. Measurement of isolated photon-hadron correlations in $\sqrt{s_{\rm NN}}$ = 5.02 TeV pp and p-Pb collisions. 5 2020.

[110] S. Acharya et al. Measurement of $\Lambda(1520)$ production in pp collisions at $\sqrt{s}$ = 7 TeV and p-Pb collisions at $\sqrt{s_{\rm NN}}$ = 5.02 TeV. *Eur. Phys. J. C*, 80(2):160, 2020.

[111] S. Acharya et al. Measurement of nuclear effects on $\psi(2S)$ production in p-Pb collisions at $\sqrt{s_{NN}}$ = 8.16 TeV. 3 2020.

[112] S. Acharya et al. Measurement of spin-orbital angular momentum interactions in relativistic heavy-ion collisions. *Phys. Rev. Lett.*, 125(1):012301, 2020.

[113] S. Acharya et al. Measurement of strange baryon–antibaryon interactions with femtoscopic correlations. *Phys. Lett. B*, 802:135223, 2020.

[114] S. Acharya et al. Measurement of the (anti-)^{3}He elliptic flow in Pb-Pb collisions at $\sqrt{s_{\rm NN}}$ = 5.02 TeV. *Phys. Lett. B*, 805:135414, 2020.

[115] S. Acharya et al. Measurement of the low-energy antideuteron inelastic cross section. 5 2020.

[116] S. Acharya et al. Measurements of inclusive jet spectra in pp and central Pb-Pb collisions at $\sqrt{s_{\rm NN}}$ = 5.02 TeV. *Phys. Rev. C*, 101(3):034911, 2020.

[117] S. Acharya et al. Multiplicity dependence of J/ψ production at midrapidity in pp collisions at $\sqrt{s}$ = 13 TeV. 5 2020.

[118] S. Acharya et al. Multiplicity dependence of K$^*(892)^0$ and $\phi(1020)$ production in pp collisions at $\sqrt{s}$ =13 TeV. *Phys. Lett. B*, 807:135501, 2020.

[119] S. Acharya et al. Multiplicity dependence of light (anti-)nuclei production in p-Pb collisions at $\sqrt{s_{\rm NN}}$ = 5.02 TeV. *Phys. Lett. B*, 800:135043, 2020.

[120] S. Acharya et al. Multiplicity dependence of (multi-)strange hadron production in proton-proton collisions at $\sqrt{s}$ = 13 TeV. *Eur. Phys. J. C*, 80(2):167, 2020.

[121] S. Acharya et al. Multiplicity dependence of π, K, and p production in pp collisions at $\sqrt{s}$ = 13 TeV. 3 2020.

[122] S. Acharya et al. Non-linear flow modes of identified particles in Pb-Pb collisions at $\sqrt{s_{\rm NN}}$ = 5.02 TeV. *JHEP*, 06:147, 2020.

[123] S. Acharya et al. Pion-kaon femtoscopy and the lifetime of the hadronic phase in Pb−Pb collisions at $\sqrt{s_{\rm NN}}$ = 2.76 TeV. 7 2020.

[124] S. Acharya et al. Probing the effects of strong electromagnetic fields with charge-dependent directed flow in Pb-Pb collisions at the LHC. *Phys. Rev. Lett.*, 125(2):022301, 2020.

[125] S. Acharya et al. Production of (anti-)^{3}He and (anti-)^{3}H in p-Pb collisions at $\sqrt{s_{\rm NN}}$ = 5.02 TeV. *Phys. Rev. C*, 101(4):044906, 2020.

[126] S. Acharya et al. Production of charged pions, kaons and (anti-)protons in Pb-Pb and inelastic pp collisions at $\sqrt{s_{\rm NN}}$ = 5.02 TeV. *Phys. Rev. C*, 101(4):044907, 2020.

[127] S. Acharya et al. Production of light-flavor hadrons in pp collisions at $\sqrt{s} = 7$ and $\sqrt{s} = 13$ TeV. 5 2020.

[128] S. Acharya et al. Production of ω mesons in pp collisions at $\sqrt{s} = 7$ TeV. 7 2020.

[129] S. Acharya et al. Scattering studies with low-energy kaon-proton femtoscopy in proton-proton collisions at the LHC. *Phys. Rev. Lett.*, 124(9):092301, 2020.

[130] S. Acharya et al. Search for a common baryon source in high-multiplicity pp collisions at the LHC. 4 2020.

[131] S. Acharya et al. Soft-dielectron excess in proton-proton collisions at $\sqrt{s} = 13$ TeV. 5 2020.

[132] S. Acharya et al. Studies of J/ψ production at forward rapidity in Pb-Pb collisions at $\sqrt{s_{\rm NN}} = 5.02$ TeV. *JHEP*, 02:041, 2020.

[133] S. Acharya et al. Transverse-momentum and event-shape dependence of D-meson flow harmonics in Pb-Pb collisions at $\sqrt{s_{\rm NN}} = 5.02$ TeV. 5 2020.

[134] S. Acharya et al. Underlying Event properties in pp collisions at $\sqrt{s} = 13$ TeV. *JHEP*, 04:192, 2020.

[135] S. Acharya et al. Υ production in p–Pb collisions at $\sqrt{s_{\rm NN}}$=8.16 TeV. *Phys. Lett. B*, 806:135486, 2020.

[136] S. Acharya et al. Z-boson production in p-Pb collisions at $\sqrt{s_{\rm NN}} = 8.16$ TeV and Pb-Pb collisions at $\sqrt{s_{\rm NN}} = 5.02$ TeV. 5 2020.

[137] J. Adam et al. Centrality dependence of high-p$_T$ D meson suppression in Pb-Pb collisions at $\sqrt{s_{mathrmNN}} = 2.76$ TeV. *JHEP*, 11:205, 2015. [Addendum: JHEP 06, 032 (2017)].

[138] J. Adam et al. Centrality dependence of inclusive J/ψ production in p-Pb collisions at $\sqrt{s_{\rm NN}} = 5.02$ TeV. *JHEP*, 11:127, 2015.

[139] J. Adam et al. Coherent ψ(2S) photo-production in ultra-peripheral Pb Pb collisions at $\sqrt{s_{\rm NN}} = 2.76$ TeV. *Phys. Lett. B*, 751:358–370, 2015.

[140] J. Adam et al. Coherent ρ^0 photoproduction in ultra-peripheral Pb-Pb collisions at $\sqrt{s_{\rm NN}} = 2.76$ TeV. *JHEP*, 09:095, 2015.

[141] J. Adam et al. Inclusive, prompt and non-prompt J/ψ production at mid-rapidity in Pb-Pb collisions at $\sqrt{s_{\rm NN}} = 2.76$ TeV. *JHEP*, 07:051, 2015.

[142] J. Adam et al. Measurement of charged jet production cross sections and nuclear modification in p-Pb collisions at $\sqrt{s_{\rm NN}} = 5.02$ TeV. *Phys. Lett. B*, 749:68–81, 2015.

[143] J. Adam et al. Measurement of dijet k_T in p–Pb collisions at $\sqrt{s_{\rm NN}}$=5.02 TeV. *Phys. Lett. B*, 746:385–395, 2015.

[144] J. Adam et al. Measurement of jet quenching with semi-inclusive hadron-jet distributions in central Pb-Pb collisions at $\sqrt{s_{\rm NN}} = 2.76$ TeV. *JHEP*, 09:170, 2015.

[145] J. Adam et al. Measurement of jet suppression in central Pb-Pb collisions at $\sqrt{s_{\rm NN}} = 2.76$ TeV. *Phys. Lett. B*, 746:1–14, 2015.

[146] J. Adam et al. Measurement of pion, kaon and proton production in proton–proton collisions at $\sqrt{s} = 7$ TeV. *Eur. Phys. J. C*, 75(5):226, 2015.

[147] J. Adam et al. One-dimensional pion, kaon, and proton femtoscopy in Pb-Pb collisions at $\sqrt{s_{\rm NN}}$ =2.76 TeV. *Phys. Rev. C*, 92(5):054908, 2015.

[148] J. Adam et al. Precision measurement of the mass difference between light nuclei and anti-nuclei. *Nature Phys.*, 11(10):811–814, 2015.

[149] J. Adam et al. Rapidity and transverse-momentum dependence of the inclusive J/ψ nuclear modification factor in p-Pb collisions at $\sqrt{s_{\rm NN}} = 5.02$ TeV. *JHEP*, 06:055, 2015.

[150] J. Adam et al. Two-pion femtoscopy in p-Pb collisions at $\sqrt{s_{\rm NN}} = 5.02$ TeV. *Phys. Rev. C*, 91:034906, 2015.

[151] J. Adam et al. ${}^{3}_{\Lambda}$H and ${}^{3}_{\Lambda}\overline{\rm H}$ production in Pb-Pb collisions at $\sqrt{s_{\rm NN}} = 2.76$ TeV. *Phys. Lett. B*, 754:360–372, 2016.

[152] J. Adam et al. Anisotropic flow of charged particles in Pb-Pb collisions at $\sqrt{s_{\rm NN}} = 5.02$ TeV. *Phys. Rev. Lett.*, 116(13):132302, 2016.

[153] J. Adam et al. Azimuthal anisotropy of charged jet production in $\sqrt{s_{\rm NN}} = 2.76$ TeV Pb-Pb collisions. *Phys. Lett. B*, 753:511–525, 2016.

[154] J. Adam et al. Centrality dependence of charged jet production in p–Pb collisions at $\sqrt{s_{\rm NN}} = 5.02$ TeV. *Eur. Phys. J. C*, 76(5):271, 2016.

[155] J. Adam et al. Centrality dependence of pion freeze-out radii in Pb-Pb collisions at $\sqrt{s_{\rm NN}} = 2.76$ TeV. *Phys. Rev. C*, 93(2):024905, 2016.

[156] J. Adam et al. Centrality dependence of ψ(2S) suppression in p-Pb collisions at $\sqrt{s_{\rm NN}} = 5.02$ TeV. *JHEP*, 06:050, 2016.

[157] J. Adam et al. Centrality dependence of the charged-particle multiplicity density at midrapidity in Pb-Pb collisions at $\sqrt{s_{\rm NN}} = 5.02$ TeV. *Phys. Rev. Lett.*, 116(22):222302, 2016.

[158] J. Adam et al. Centrality dependence of the nuclear modification factor of charged pions, kaons, and protons in Pb-Pb collisions at $\sqrt{s_{\rm NN}} = 2.76$ TeV. *Phys. Rev. C*, 93(3):034913, 2016.

[159] J. Adam et al. Centrality evolution of the charged-particle pseudorapidity density over a broad pseudorapidity range in Pb-Pb collisions at $\sqrt{s_{\rm NN}} = 2.76$ TeV. *Phys. Lett. B*, 754:373–385, 2016.

[160] J. Adam et al. Charge-dependent flow and the search for the chiral magnetic wave in Pb-Pb collisions at $\sqrt{s_{\rm NN}} = 2.76$ TeV. *Phys. Rev. C*, 93(4):044903, 2016.

[161] J. Adam et al. Correlated event-by-event fluctuations of flow harmonics in Pb-Pb collisions at $\sqrt{s_{\rm NN}} =$ 2.76 TeV. *Phys. Rev. Lett.*, 117:182301, 2016.

[162] J. Adam et al. D-meson production in p-Pb collisions at $\sqrt{s_{\rm NN}}$ =5.02 TeV and in pp collisions at $\sqrt{s}$ =7 TeV. *Phys. Rev. C*, 94(5):054908, 2016.

[163] J. Adam et al. Differential studies of inclusive J/ψ and ψ(2S) production at forward rapidity in Pb-Pb collisions at $\sqrt{s_{\rm NN}} = 2.76$ TeV. *JHEP*, 05:179, 2016.

[164] J. Adam et al. Direct photon production in Pb-Pb collisions at $\sqrt{s_{\rm NN}} = 2.76$ TeV. *Phys. Lett. B*, 754:235–248, 2016.

[165] J. Adam et al. Elliptic flow of electrons from heavy-flavour hadron decays at mid-rapidity in Pb-Pb collisions at $\sqrt{\rm s_{NN}} = 2.76$ TeV. *JHEP*, 09:028, 2016.

[166] J. Adam et al. Elliptic flow of muons from heavy-flavour hadron decays at forward rapidity in Pb–Pb collisions at $\sqrt{s_{\rm NN}} = 2.76$ TeV. *Phys. Lett. B*, 753:41–56, 2016.

[167] J. Adam et al. Event shape engineering for inclusive spectra and elliptic flow in Pb-Pb collisions at $\sqrt{s_{\rm NN}} = 2.76$ TeV. *Phys. Rev. C*, 93(3):034916, 2016.

[168] J. Adam et al. Forward-central two-particle correlations in p-Pb collisions at $\sqrt{s_{\rm NN}} = 5.02$ TeV. *Phys. Lett. B*, 753:126–139, 2016.

[169] J. Adam et al. Higher harmonic flow coefficients of identified hadrons in Pb-Pb collisions at $\sqrt{s_{\rm NN}} =$ 2.76 TeV. *JHEP*, 09:164, 2016.

[170] J. Adam et al. Inclusive quarkonium production at forward rapidity in pp collisions at $\sqrt{s} = 8$ TeV. *Eur. Phys. J. C*, 76(4):184, 2016.

[171] J. Adam et al. Jet-like correlations with neutral pion triggers in pp and central Pb–Pb collisions at 2.76 TeV. *Phys. Lett. B*, 763:238–250, 2016.

[172] J. Adam et al. Measurement of an excess in the yield of J/ψ at very low p_T in Pb-Pb collisions at $\sqrt{s_{\rm NN}} = 2.76$ TeV. *Phys. Rev. Lett.*, 116(22):222301, 2016.

[173] J. Adam et al. Measurement of D-meson production versus multiplicity in p-Pb collisions at $\sqrt{s_{\rm NN}} = 5.02$ TeV. *JHEP*, 08:078, 2016.

[174] J. Adam et al. Measurement of $\rm D_s^+$ production and nuclear modification factor in Pb-Pb collisions at $\sqrt{s_{\rm NN}} = 2.76$ TeV. *JHEP*, 03:082, 2016.

[175] J. Adam et al. Measurement of electrons from heavy-flavour hadron decays in p-Pb collisions at $\sqrt{s_{\rm NN}} = 5.02$ TeV. *Phys. Lett. B*, 754:81–93, 2016.

[176] J. Adam et al. Measurement of transverse energy at midrapidity in Pb-Pb collisions at $\sqrt{s_{\rm NN}} = 2.76$ TeV. *Phys. Rev. C*, 94(3):034903, 2016.

[177] J. Adam et al. Multi-strange baryon production in p-Pb collisions at $\sqrt{s_{\rm NN}} = 5.02$ TeV. *Phys. Lett. B*, 758:389–401, 2016.

[178] J. Adam et al. Multipion Bose-Einstein correlations in pp,p -Pb, and Pb-Pb collisions at energies available at the CERN Large Hadron Collider. *Phys. Rev. C*, 93(5):054908, 2016.

[179] J. Adam et al. Multiplicity and transverse momentum evolution of charge-dependent correlations in pp, p–Pb, and Pb–Pb collisions at the LHC. *Eur. Phys. J. C*, 76(2):86, 2016.

[180] J. Adam et al. Multiplicity dependence of charged pion, kaon, and (anti)proton production at large transverse momentum in p-Pb collisions at $\sqrt{s_{\rm NN}} = 5.02$ TeV. *Phys. Lett. B*, 760:720–735, 2016.

[181] J. Adam et al. Particle identification in ALICE: a Bayesian approach. *Eur. Phys. J. Plus*, 131(5):168, 2016.

[182] J. Adam et al. Production of $\rm K^*(892)^0$ and $\phi(1020)$ in p–Pb collisions at $\sqrt{s_{\rm NN}} = 5.02$ TeV. *Eur. Phys. J. C*, 76(5):245, 2016.

[183] J. Adam et al. Production of light nuclei and anti-nuclei in pp and Pb-Pb collisions at energies available at the CERN Large Hadron Collider. *Phys. Rev. C*, 93(2):024917, 2016.

[184] J. Adam et al. Pseudorapidity and transverse-momentum distributions of charged particles in proton–proton collisions at $\sqrt{s} = 13$ TeV. *Phys. Lett. B*, 753:319–329, 2016.

[185] J. Adam et al. Pseudorapidity dependence of the anisotropic flow of charged particles in Pb-Pb collisions at $\sqrt{s_{\rm NN}} = 2.76$ TeV. *Phys. Lett. B*, 762:376–388, 2016.

[186] J. Adam et al. Search for weakly decaying $\overline{\Lambda}\overline{\rm n}$ and $\Lambda\Lambda$ exotic bound states in central Pb-Pb collisions at $\sqrt{s_{\rm NN}} = 2.76$ TeV. *Phys. Lett. B*, 752:267–277, 2016.

[187] J. Adam et al. Study of cosmic ray events with high muon multiplicity using the ALICE detector at the CERN Large Hadron Collider. *JCAP*, 01:032, 2016.

[188] J. Adam et al. Transverse momentum dependence of D-meson production in Pb-Pb collisions at $\sqrt{s_{\rm NN}} = 2.76$ TeV. *JHEP*, 03:081, 2016.

[189] J. Adam et al. Anomalous evolution of the near-side jet peak shape in Pb-Pb collisions at $\sqrt{s_{\rm NN}} = 2.76$ TeV. *Phys. Rev. Lett.*, 119(10):102301, 2017.

[190] J. Adam et al. Centrality dependence of the pseudorapidity density distribution for charged particles in Pb-Pb collisions at $\sqrt{s_{\rm NN}} = 5.02$ TeV. *Phys. Lett. B*, 772:567–577, 2017.

[191] J. Adam et al. Charged-particle multiplicities in proton–proton collisions at $\sqrt{s} = 0.9$ to 8 TeV. *Eur. Phys. J. C*, 77(1):33, 2017.

[192] J. Adam et al. Determination of the event collision time with the ALICE detector at the LHC. *Eur. Phys. J. Plus*, 132(2):99, 2017.

[193] J. Adam et al. Enhanced production of multi-strange hadrons in high-multiplicity proton-proton collisions. *Nature Phys.*, 13:535–539, 2017.

[194] J. Adam et al. Evolution of the longitudinal and azimuthal structure of the near-side jet peak in Pb-Pb collisions at $\sqrt{s_{\rm NN}} = 2.76$ TeV. *Phys. Rev. C*, 96(3):034904, 2017.

[195] J. Adam et al. Flow dominance and factorization of transverse momentum correlations in Pb-Pb collisions at the LHC. *Phys. Rev. Lett.*, 118(16):162302, 2017.

[196] J. Adam et al. Insight into particle production mechanisms via angular correlations of identified particles in pp collisions at $\sqrt{\rm s} = 7$ TeV. *Eur. Phys. J. C*, 77(8):569, 2017. [Erratum: Eur.Phys.J.C 79, 998 (2019)].

[197] J. Adam et al. J/ψ suppression at forward rapidity in Pb-Pb collisions at $\sqrt{s_{NN}} = 5.02$ TeV. *Phys. Lett. B*, 766:212–224, 2017.

[198] J. Adam et al. $\rm K^*(892)^0$ and $\phi(1020)$ meson production at high transverse momentum in pp and Pb-Pb collisions at $\sqrt{s_{\rm NN}} = 2.76$ TeV. *Phys. Rev. C*, 95(6):064606, 2017.

[199] J. Adam et al. Measurement of azimuthal correlations of D mesons and charged particles in pp collisions at $\sqrt{s} = 7$ TeV and p-Pb collisions at $\sqrt{s_{\rm NN}} = 5.02$ TeV. *Eur. Phys. J. C*, 77(4):245, 2017.

[200] J. Adam et al. Measurement of electrons from beauty-hadron decays in p-Pb collisions at $\sqrt{s_{\rm NN}} = 5.02$ TeV and Pb-Pb collisions at $\sqrt{s_{\rm NN}} = 2.76$ TeV. *JHEP*, 07:052, 2017.

[201] J. Adam et al. Measurement of the production of high-p_T electrons from heavy-flavour hadron decays in Pb-Pb collisions at $\sqrt{s_{\rm NN}} = 2.76$ TeV. *Phys. Lett. B*, 771:467–481, 2017.

[202] J. Adam et al. ϕ-meson production at forward rapidity in p-Pb collisions at $\sqrt{s_{\rm NN}} = 5.02$ TeV and in pp collisions at $\sqrt{s} = 2.76$ TeV. *Phys. Lett. B*, 768:203–217, 2017.

[203] J. Adam et al. W and Z boson production in p-Pb collisions at $\sqrt{s_{\rm NN}} = 5.02$ TeV. *JHEP*, 02:077, 2017.

[204] D. Adamová et al. J/ψ production as a function of charged-particle pseudorapidity density in p-Pb collisions at $\sqrt{s_{\rm NN}} = 5.02$ TeV. *Phys. Lett. B*, 776:91–104, 2018.

[205] D. Adamova et al. Azimuthally differential pion femtoscopy in Pb-Pb collisions at $\sqrt{s_{\rm NN}} = 2.76$ TeV. *Phys. Rev. Lett.*, 118(22):222301, 2017.

[206] D. Adamova et al. Production of $\Sigma(1385)^{\pm}$ and $\Xi(1530)^0$ in p-Pb collisions at $\sqrt{s_{\rm NN}} = 5.02$ TeV. *Eur. Phys. J. C*, 77(6):389, 2017.

[207] M. Aggarwal et al. Particle identification studies with a full-size 4-GEM prototype for the ALICE TPC upgrade. *Nucl. Instrum. Meth. A*, 903:215–223, 2018.

[208] N. Poljak, A. Bosilj, S. Brzaj, J. Dragović, T. Dubček, F. Erhardt, and M. Jerčić. Physionary - a scientific version of Pictionary. *Physics Education*, 063004:53, 2018.

[209] A. Utrobicic, M. Kovacic, F. Erhardt, M. Jercic, N. Poljak, and M. Planinic. Studies of the delayed discharge propagation in the Gas Electron Multiplier (GEM). *Nucl. Instrum. Meth. A*, 940:262–273, 2019.

[210] A. Utrobicic, M. Kovacic, F. Erhardt, N. Poljak, and M. Planinic. A floating multi-channel picoammeter for micropattern gaseous detector current monitoring. *Nucl. Instrum. Meth. A*, 801:21–26, 2015.

Nikola Poljak was born on 27.6.1982 in Čakovec, where he attended both elementary and high school. In 2000 he enrolled the study of physics at the Faculty of Science at the University of Zagreb. In 2005 he graduated with the diploma thesis topic "Non-conservation of the lepton number" under the guidance of prof. Amon Ilakovac. From 2005-2010 he was a PhD student at the University of Zagreb, working on the STAR experiment located at the Brookhaven National Laboratory (New York, USA). In 2010 he became a PhD in physics (experimental high energy particle physics) by defending his thesis topic "Transverse single spin asymmetries for the production of neutral pions in proton collisions at $\sqrt{s} = 200$ GeV".

After obtaining his PhD, he was employed as a postdoc in the Netherlands (Utrecht/Amsterdam, 1.1.-1.7.2012), at the Ruđer Bošković Institute (1.9.2012-1.8.2013) and at the Faculty of Science at the University of Zagreb (1.8.2013-1.5.2014). During these, he worked on future upgrades of the ALICE detector at forward angles, testing the CMS tracking system and finally on the upgrade of the ALICE TPC chamber.

Since 2014 he is employed at the Faculty of Science, University of Zagreb as an assistant professor. He began work on the ridge phenomenon on ALICE data, continued work on GEM detectors for the ALICE TPC chamber and started working on educational methods in physics. he was put in charge of the General physics courses (1-4) for physics researcher undergraduates, and has started working as an outside collaborator at the Faculty of nutrition and biotechnology (physics courses lab exercises) and at the Faculty of electrotechnics (co-introducing a new course named "Creative laboratory"). Since 2019 he has been in charge of a new course on the graduate study of particle physics.

During his work he put a lot of effort into the popularization of science. He was the main organizer of the first Open day of the Faculty of science, the main organizer or the co-organizer of the summer school for young physicists (2014-2019), the leader of the section for physics popularization at the Croatian physical society (4 years) as well as the team leader for the Croatian team at the International physicists' tournament (3 years). In addition, he gave a number of popular science talks at various schools, science festivals and public forums and has been a guest at the national TV over 30 times.

As an assistant professor, he began work in educational physics and has published several articles in that field of research. He is currently a member of the physics working group at the National center for external evaluation of education (writing original problems

for state exams and creating a new concept for a state exam in physics). He organized the first “Physics at the University” meeting and has been a member of the state commission for physics competitions for the last 10 years. Finally, he authored 3 University manuals with a focus on general physics problems.

He participated in the organizing of the 14th conference of Croatian physics teachers, the ICPRSE conference (Subotica, Serbia 2018 and 2019), and the Alice week outside CERN 2014 conference. He is an active member of the ALICE, STAR and RD51 collaborations and a member observer of the JUNO collaboration. He has been awarded the University research support grant 4 time and one NVIDIA Academic grant. He has mentored 15 diploma theses and is currently mentoring two PhD students. Alongside scientific publications, he has authored or co-authored 18 conference proceedings. He is currently the leader of the section for industrial physics at the Croatian physical society and a member of a Croatian science foundation project.